Technische Universität München
TUM School of Natural Sciences

Broadband Two-Photon Excitation Spectroscopy: A Method to Guide the Optimization of Multiphoton Absorption in Coordination Polymers

Yang Cui

Vollständiger Abdruck der von der TUM School of Natural Sciences der Technischen Universität München zur Erlangung eines

Doktors der Naturwissenschaften (Dr. rer. nat.)

genehmigten Dissertation.

Vorsitz:	Prof. Dr. Sebastian Günther
Prüfende der Dissertation:	1. Prof. Dr. Jürgen Hauer
	2. Prof. Dr. Jan Torgersen

Die Dissertation wurde am 14.06.2024 bei der Technischen Universität München eingereicht und durch die TUM School of Natural Sciences am 01.07.2024 angenommen.

Acknowledgments

The completion of this thesis would not have been possible without the help of many people, and I would like to express my sincere gratitude and appreciation to everyone involved before presenting any results.

I had the pleasure to be supervised by an excellent researcher, Prof. Jürgen Hauer. I am indebted to thank you for the exceptional scientific and very personal supervision, which I do not take for granted. Thank you for the overall support throughout my thesis, always encouraging me to get the best out of my research.

Additionally, I must express my gratitude to Pavel Malevich and Lars Mewes for their lab assistance and general cheerful attitude. I am particularly grateful for all the valuable and helpful academic discussions with Erling Thyrhaug, Václav Šebelík, Pushpendra Kumar, and Kiran Maiti.

Furthermore, I want to thank Sebastian Weishäupl, Simon Deger, Alexander Pöthig, and Prof. Roland Fischer for all the helpful academic discussions and for sharing their knowledge on coordination polymers. I thank Prof. Eberhard Riedle and Ferdinand Bergmeier for their generous help and enthusiasm for nonlinear optics. I thank Prof. Aleksandr Ovsianikov and Hamad Syed for letting me access their novel setup in Vienna. I also want to thank Prof. Jan Torgersen for sharing his knowledge of two-photon absorption with me and agreeing to be my second examiner.

Special thanks also to my fellow PhD students and co-workers, Ajeet Kumar, Constantin Heshmatpour, Erika Keil, Yi Xu, Maximilian Binzer, Hongxing Hao, Miriam Jänchen, Alina Bach, Annett Bachmann, Matthias Stecher, Peter Kämmerer, Sabine Kullick and Sabine Fölsner, for providing a comfortable and positive work environment where everyone helps everyone.

I am deeply grateful to my wife, Hongmei Jiao, for her encouraging and loving nature, which was a great support, especially in the last phases of this work.

I would like to end with a big thank you to my parents, Huanzhen Cui and Tongxiang Yang, and my sister Feng Cui. Without your loving and active support, I would never have gotten to where I am now. Thank you!

Abstract

Two-photon absorption (2PA) is a desirable nonlinear optical (NLO) process because of its myriad applications in, e.g., bioimaging, optoelectronics, and microfabrication. Metal–organic frameworks (MOFs) and coordination polymers (CPs) exhibiting NLO properties, e.g., 2PA, are of high interest for photophysically relevant applications. Their tunability leads to various designs, and the investigation of structure–property relations of MOFs and CPs is vital for synthesizing materials with enhanced NLO properties. In particular, we design, synthesize, and characterize MOFs and CPs with improved 2PA cross-sections. Our approach is to incorporate 2PA-active organic linker molecules in crystalline CPs. By comparing the 2PA spectrum of the linkers in solution and the CPs, we suggest excitonic coupling between the linkers as the primary mechanism behind the increased 2PA compared to solvated linkers.

We first characterize three highly 2PA-active CPs based on two carbazole-containing chromophore linkers. Z-scan analysis of three CPs shows large 2PA cross sections with up to three orders of magnitude enhancement compared to the solvated linkers. Based on this achievement, we further investigated different spatial chromophore arrangements using additional pillar linkers for CP formation. Two novel pillar-layered CPs are reported and examined in their two-photon-induced fluorescence and compared to a previously synthesized CP with the same chromophore but no pillars.

Instead of using the Z-scan technique, we design, implement, and employ an experiment to measure two-photon excitation spectra of pillar-layered CPs with nonlinear Fourier-transform spectroscopy. It is based on 10 fs pulses generated in a noncollinear optical parametric amplifier and a phase-stable common-path birefringent interferometer. The comparison shows a significant difference for the 2PA cross sections of the materials, improving it by incorporating the pillar. Our findings point toward the significance of controlling the chromophore orientation, e.g., structure rigidification and coplanarity of chromophores in CPs, to tailor the NLO properties of the materials. These insights demonstrate the feasibility of our approach to the aim-directed development of MOFs and CPs for advanced photonic applications.

Zusammenfassung

Zwei-Photonen-Absorption (2PA) ist ein erstrebenswerter nichtlinearer optischer (NLO) Prozess aufgrund einer Vielzahl an Anwendungen in Bereichen wie biologische Bildgebung, Optoelektronik und Mikrofabrikation. Metalorganische Gerüstverbindungen (MOFs) und Koordinationspolymere (CPs), die nichtlineare optische Eigenschaften wie 2PA aufweisen sind von hohem Interesse für photophysikalisch relevante Anwendungen. Ihre Verstellbarkeit führt zu verschiedenen Ausführungen. Die Untersuchung von Zusammenhägen zwischen der Struktur und der Eigenschaften von MOFs und CPs ist unerlässlich für die Synthese von Materialen mit verstärkten NLO-Eigenschaften. Insbesondere entwerfen, synthetisieren und charakterisieren wir MOFS und CPS mit verbesserten 2PA Wirkungsquerschnitten. Unser Ansatz ist es 2PA-aktive, organische Linker-Moleküle in kristalline CP zu integrieren. Aufgrund des Vergleiches von 2PA-Spektren der Linker in Lösung und der CPs, schlagen wir vor, dass exzitonische Kopplung zwischen den Linkern als hauptsächlicher Mechanismus hinter der gesteigerten 2PA dient, die im Vergleich zu Linkern in Lösung festgestellt wird.

Zuerst wurden drei stark 2PA-aktive CP basierend auf zwei Carbazol beinhaltenden chromophoren Linker charakterisiert. Z-scan Analyse von drei CPn zeigt 2PA Wirkungsquerschnitte, die bis zu drei Größenordnungen über denen von Linkern in Lösung liegen. Aufgrund dieses Ergebnisses wurden verschiedene räumliche chromophoren Anordnungen untersucht, die auf der Nutzung zusätzlicher Pillar Linkers zur Bildung der CP basieren. Zwei neue Pillar-geschichtete CPs wurden anhand ihrer Zwei-Photonen-Fluoreszenz untersucht und verglichen mit den zuvor synthetisierten CPs, die das gleiche Chromophor aber keine Pillar besaßen.

Anstelle der Z-scan Technik, wurde ein Experiment zur Messung von Zwei-Photonen Anregungsspektren der Pillar-geschichteten CPs mithilfe nichtlinearer Fourier-Transformations-Spektroskopie entworfen, umgesetzt und angewendet. Dieses basiert auf 10 fs Pulsen, die in einem nichtlinearen optischen parametrischen Verstärker erzeugt wurden, und einem phasenstabilen doppelbrechenden Common-Path-Interferometer. Im Vergleich zeigt sich ein nennenswerter Unterschied für die 2PA Wechselwirkungsquerschnitte der Materialen durch die Verbesserung aufgrund der Pillar. Die Ergebnisse weisen auf die Relevanz der Kontrolle der chromophoren Orientierung, so zum Beispiel strukturelle Versteifung und Koplanarität der chromophoren in CPS, zur Anpassung der NLO-Eigenschaften des Materials hin. Diese Einblicke demonstrieren die Durchführbarkeit des Ansatzes zur gezielten Entwicklung von MOFs und CPs für fortgeschrittene optische Anwendungen.

Scientific contributions

Publications with first or shared first authorship

1. Weishäupl, S.J.[†]; Cui, Y.[†]; Deger, S.N.; Syed, H.; Ovsianikov, A.; Hauer, J.; Pöthig, A.; Fischer, R.A. Coordination polymers based on carbazole-derived chromophore linkers for optimized multiphoton absorption: a structural and photophysical study. *Chemistry of Materials*, **34**(16):7402–7411, **2022**.

2. Deger, S.N.[†]; Cui, Y.[†]; Warnan, J.; Fischer, R.A.; Šanda, F.; Hauer, J.; Pöthig, A. Influence of chromophore packing on multiphoton absorption in carbazole-based pillar-layered coordination polymers. *ACS Applied Optical Materials*, **2024**. Accepted.

3. Cui, Y.; Bergmeier, F.; Hao, H.; Kumar, A.; Deger, S.N.; Mewes, L.; Thyrhaug, E.; Riedle, E.; Pöthig, A.; Fischer, R.A.; Hauer, J. Broadband two-photon excitation spectroscopy based on a common-path birefringent interferometer and 10 fs pulses. Under preparation.

Publications with co-authorship

1. Weishäupl, S.J.[†]; Mayer, D.C.[†]; Cui, Y.; Kumar, P.; Oberhofer, H.; Fischer, R.A.; Hauer, J.; Pöthig, A. Recent advances of multiphoton absorption in metal–organic frameworks. *Journal of Materials Chemistry C*, **10**:6912–6934, **2022**.

Presentations

1. Poster (first author): Two-photon absorption in metal–organic frameworks, *International Conference on Metal–Organic Frameworks and Open Frameworks Compounds*, September **2022**, Dresden, Germany.

2. Talk: Two-photon excitation spectroscopy — with an outlook on time-resolved fluorescence, *Seminar on Spectroscopy and Theory of Open Quantum Systems*, December **2023**, Prague, the Czech Republic.

[†] These authors contributed equally to this work.

Contents

Chapter 1

Introduction: two-photon excitation spectroscopy on coordination polymers

In this Chapter, we first discuss the concept of multiphoton absorption (MPA) and define the two-photon absorption (2PA) cross-section. A comparison of one-photon absorption (1PA) and 2PA is given in the framework of perturbation theory. Section 1.2 outlines the design principles of MPA-active coordination polymers (CPs). Section 1.3 summarizes the principal experimental techniques and challenges for measuring the 2PA cross-section, emphasizing two-photon Fourier transform spectroscopy used to characterize CPs in this work.

1.1 Concepts and descriptions of multiphoton absorption

Multiphoton absorption (MPA), i.e., the simultaneous absorption of two or more photons in a single event (as shown in the energy diagram in Fig. 1.1), was first predicted by Göppert-Mayer in 1931 [1] and was reported experimentally by Kaiser and Garrett in 1961 [2], one year after the invention of the first working laser by Maiman [3]. Since then, MPA has found extensive applications in the field of, e.g., spectroscopy of gas phase molecules [4], Doppler-free rotationally resolved electronic spectroscopy of polyatomic molecules [5], microscopic imaging [6], optical limiting [7], two-photon lithography [8] and polymerization [9].

Propagation of a light beam with intensity I incidents on a material is governed by the equation

$$\frac{\mathrm{d}I}{\mathrm{d}z} = -\alpha I - \beta I^2 - \gamma I^3 + \cdots , \tag{1.1}$$

where z is the depth in the sample, α, β, and γ are one-photon, two-photon, and three-photon absorption coefficients, respectively. Considering that only a linear absorption process takes place, i.e., $\mathrm{d}I/\mathrm{d}z = -\alpha I$, the solution of Eq. 1.1, which represents the light intensity at the exit

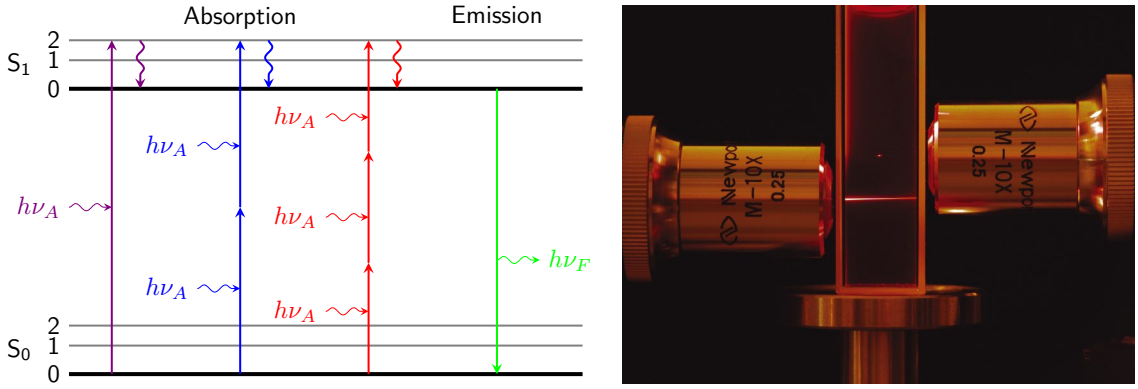

Figure 1.1: Energy level diagram of 1PA and MPAs for a molecule to reach from the ground state S_0 to the excited state S_1 followed with fluorescence emission (left). Fluorescence in a solution caused by 1PA and 2PA using microscope objectives to focus light beams (right; figure adapted from Newport).

of the sample, is given by

$$I = I_0 e^{-\alpha L}\,, \tag{1.2}$$

indicating the incoming light with intensity I_0 follows the exponential attenuation in the sample with a thickness of L, i.e., the so-called Beer–Lambert law. By selecting proper excitation conditions and assuming that linear and n-photon absorptions ($n \geq 3$) are negligible, Eq. 1.1 reduces to $\mathrm{d}I/\mathrm{d}z + \beta I^2 = 0$. This gives the intensity after the sample, attenuated solely by 2PA:

$$I = \frac{I_0}{1 + \beta I_0 L}\,, \tag{1.3}$$

which will reach a limiting case of $I = 1/\beta L$ when applying a large initial intensity I_0. This phenomenon is widely used for optical limiting and switching [7, 10].

As a macroscopic parameter, the 2PA coefficient β is concentration dependent [11, 12]. Therefore, 2PA cross-section $\sigma^{(2)}$ to describe molecular 2PA probability at respective wavelength λ is introduced, and its relation to β is expressed by:

$$\sigma^{(2)}(\lambda) = \frac{hc\beta(\lambda)}{\lambda N_\mathrm{A} \rho \times 10^{-3}}\,, \tag{1.4}$$

with its unit GM (Göppert-Mayer) defined as $1\,\mathrm{GM} = 10^{-50}\,\mathrm{cm}^4\,\mathrm{s}\,\mathrm{photon}^{-1}\,\mathrm{molecule}^{-1}$. Here, h is the Planck constant, c is the speed of light, N_A is the Avogadro constant, and ρ is the concentration of a given sample.

The treatment so far is purely phenomenological, meaning that we have not developed a way to predict one- or two-photon absorption spectrum in its shape or intensity. This is commonly achieved by applying perturbation theory, leading to expressions for the transition moments

$M_{fg}^{(1)}$ and $M_{f'g}^{(2)}$ for one- and two-photon absorption, respectively. The fundamental difference between 1PA and 2PA can be distinguished from the expression for $M_{fg}^{(1),(2)}$ between the ground (g) and excited (f) states of a molecule. The respective absorption cross sections $\sigma^{(1)}$ and $\sigma^{(2)}$ scale with the expectation value $|M_{fg}^{(1),(2)}|^2$. For 1PA, the matrix elements are

$$M_{fg}^{(1)} = \langle f|\vec{E}\cdot\vec{\mu}|g\rangle\,, \tag{1.5}$$

where $\vec{E}$ represents the excitation light field along a defined polarization direction and $\vec{\mu}$ is the dipole moment operator [13]. 1PA is most efficient when the frequency of the driving laser ω_{L} meets a resonance condition $\omega_{fg} = \omega_{\mathrm{L}}$. 2PA is most efficient when the resonance condition $\omega_{f'g} = 2\omega_{\mathrm{L}}$ is met, where state f' is the final state reached by the 2PA process, as depicted in Fig. 1.2. The 2PA probability is defined by the 2PA cross-section $\sigma^{(2)} \propto |M_{f'g}^{(2)}|^2$ derived from the two-photon transition matrix elements

$$M_{f'g}^{(2)} = \frac{1}{\hbar}\sum_{e}\frac{\langle f'|\vec{E}\cdot\vec{\mu}|e\rangle\langle e|\vec{E}\cdot\vec{\mu}|g\rangle}{\omega_{eg}-\omega_{\mathrm{L}}}\,, \tag{1.6}$$

where ω_{eg} stands for the transition frequency between the ground state g and nonresonant intermediate transient levels e [14, 15]. The final excited state f' after 2PA is usually different from f after 1PA as the analysis of Eqs. 1.5 and 1.6 suggests different selection rules for them. Consequently, the transition between the ground and final state f' does not have to be one-photon allowed. The dependence of $M_{f'g}^{(2)}$ on detuning $\omega_{eg} - \omega_{\mathrm{L}}$ is an important feature of Eq. 1.6, as only those transient e levels close to resonance with ω_{L} will contribute significantly.

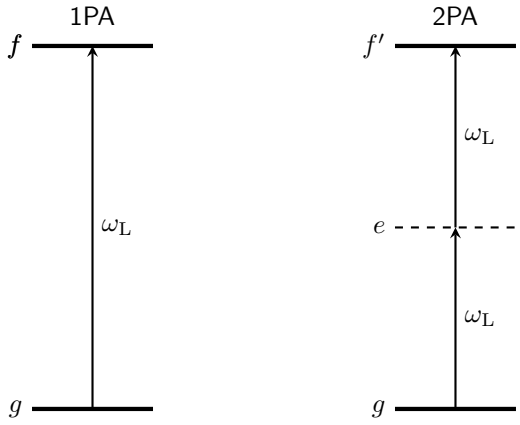

Figure 1.2: Schematic energy level diagram of a 1PA process reaching the final state f from the ground stare g by absorbing one photon with frequency ω_{L} (left), and a 2PA process reaching the final state f' by absorbing two photons via a nonresonant intermediate state e (right).

The overall probability of simultaneous absorption of two photons is low, which explains why 2PA is not a commonly observed phenomenon but requires either tight focusing of high-power CW lasers [5] or the high peak intensity of nanosecond, picosecond, or femtosecond

excitation pulses [16]. The number n_{abs} of photons absorbed per molecule per pulse depends on pulse duration τ_{p}, laser repetition rate R_{p}, laser intensity I_0, beam spot size A at the sample position, and numerical aperture NA of the focusing lens, as

$$n_{\mathrm{abs}} \approx \frac{I_0^2 A^2 \sigma^{(2)}}{\tau_{\mathrm{p}} R_{\mathrm{p}}^2} \left(\frac{\mathrm{NA}^2}{2\hbar c \lambda} \right)^2 , \tag{1.7}$$

where c is the speed of light, and $\hbar$ is the reduced Planck constant; saturation is neglected, and the paraxial approximation is assumed [6]. The efficiency of 2PA depends on molecular properties and the temporal and spatial distribution of the excitation laser [17]. Eq. 1.7 indicates that, without saturation or other nonlinear effects, g to f' population transfer is governed by the square law, i.e., $n_{\mathrm{abs}} \propto I_0^2$. This relation has to be ensured experimentally when aiming for pure 2PA signals.

1.2 Multiphoton-active coordination polymers

In the search for materials with optimized $\sigma^{(2)}$ values, different materials such as perovskites [18–21], polymers [22, 23], and molecular organic chromophores have been investigated [24]. Prominent material classes that are mostly studied in the context of such MPA activity are organic chromophores and inorganic nanoparticles. Although these substance classes show promising MPA properties, they show disadvantages such as low thermal stability and uncontrolled aggregation, which already limits their applicability [25]. Inorganic–organic hybrid materials such as coordination polymers (CPs) are of high interest in chemistry and materials science due to their modular design and the potential for tuning 2PA properties by incorporating different functional groups [26, 27]. More specific subgroups of CPs are (i) coordination networks, which are one-dimensional coordination chains with cross-links to two or more individual chains, forming two- or even three-dimensional networks, and (ii) metal–organic frameworks (MOFs), which are coordination networks with potential voids [28, 29].

CPs offer unique opportunities to modulate and optimize chromophore arrangements by reticular synthesis and, in turn, for the targeted design of highly MPA-active solid-state materials. Besides this so-called "inter-molecular approach" of tuning MPA in CPs via specific linker assemblies, there are other levels impacting MPA in CPs (and MOFs), such as the local conformational confinement (rigidification) of chromophore linkers (strain energy and planarization of π-systems) as well as enhanced polarization of the involved photo-excited states via metal-to-ligand or ligand-to-metal charge transfer bands (MLCT and LMCT) or the simple polarization of ligand electron density due to electron-pushing/pulling effects of the metal ions [26]. MPA-CP materials perspectives include increasing data storage densities in optical devices (e.g., CD, DVD) by two-photon excitation [30, 31]. Multiphoton processes provide the capability of triggering photochemical reactions and physical changes with a micrometer- and potentially even nanometer-sized resolution, allowing for high-density recording and mapping [11]. This necessitates materials with high MPA performances, long-term photostability, and easy and

cost-effective device processing [32]. For applications of MPA with high technological impact, such as bio-imaging, photodynamic therapy, or telecommunication, MPA-active materials with a broad range of properties are needed. Biological applications, e.g., need MPA materials with high cross-section values, large fluorescence quantum yields, and stability *in vivo* [33]. CPs offer highly active MPA materials that can be tuned to very low crystallite (particle) sizes (nm range) and can be modified for solubility and agglomeration inhibition and targeted transport or anchoring (via capping agents) [34]. MPA-CP nanoparticles can be used as porous materials with cavities of tunable size to transport medically active compounds while in parallel imaging the cell inclusion pathways. These are examples of many, clearly illustrating how CP materials chemistry and physics can contribute to the field of MPA on different levels. The processing of CPs and MOFs, controlled by particle size, thin film deposition, selective crystallite positioning, and post-synthetic modification, makes them an interesting materials platform for testing nonlinear optical effects.

However, several factors have to be taken into account influencing the properties of the CPs: choice of metal node and linker, coordination geometries of the linker and sub-building block (SBU), secondary interactions such as hydrogen bonding, π–π interactions or metal-to-ligand interactions determining the materials properties [35]. All of these interactions depend on the CP's linker arrangement, which in turn leads to reticular chemistry, describing the chemistry of linking molecular building blocks to extended frameworks [36, 37].

This topology can now be retained with different linkers as long as the connectivity of the building blocks stays the same and the elongation does not lead to framework interpenetration. With this crystal engineering tool, by choosing SBU and linker connectivity, different arrangements of chromophores inside the network can be achieved to obtain an improved structure–property relationship. Therefore, different design principles for MPA-active CPs have to be established.

In contrast to simple CP synthesis, which is only dependent on the linker–SBU interaction, MPA-active CPs can be designed in many ways, e.g., by using open shell metal precursors for the SBU, by introducing MPA-active guests inside the pores or by using MPA active linkers as chromophores [38–40]. Within this thesis, only CPs with "optical-innocent" metals, where the MPA character originates from the linker molecule, were investigated to deepen the understanding of an MPA-property–structure relationship.

As stated above, the chromophores themselves suffer from diverse limitations concerning MPA activity through uncontrolled aggregation in highly concentrated solutions and low thermal stability [25, 41]. Therefore, incorporating these chromophores into CPs is a perfect candidate to overcome those limitations, as the chromophore density in CPs can be much higher than in solution for concentrations below aggregate formation. Additionally, the incorporation of linker molecules already increases the emissive properties due to the limitation of the radiationless energy channels caused by the restricted conformation of the linker between the metal centers [42]. This is one of the most significant advantages of MOFs and CPs compared to other

materials. Additionally, in the case of transition metals, MLCT or LMCT bands introduce new charge transfer bands, facilitating higher MPA-activity than for the linker itself. Nonetheless, the ligand primarily defines the nonlinear optical properties of CPs if photophysically silent metals with closed electron shells are used [26].

1.3 Nonlinear optical spectroscopic techniques

Experimental methods in two-photon excitation spectroscopy can be categorized as frequency-domain and time-domain techniques. In frequency-domain technique, direct and indirect methods can be distinguished by the type of measured signals, where direct method is based on the measurement of beam attenuation after material transmission [43–46] and indirect method is based on action detection, e.g., two-photon induced fluorescence or phosphorescence emission [47–49] and thermal lensing [50, 51].

1.3.1 Frequency domain techniques

Among the direct methods for measuring nonlinear optical properties of substances, particularly 2PA cross sections, the Z-scan method is the most popular. Z-scan was initially introduced by Sheik-Bahae et al. in 1989 [45]. It is the most straightforward and widespread method for determining third-order nonlinear optical properties, e.g., nonlinear absorption coefficient and refractive index. The method is based on the far-field measurement of a change in the exciting laser radiation transmitted through a sample depending on the sample position z with respect to the focal point, as illustrated in Fig. 1.3. The sample moves through the focus of the laser beam, and a change in the transmittance is recorded at each sample position during the entire sample scanning without placing an aperture in front of the detector. This method has a lower sensitivity than the reference method but allows the measurement of the 2PA cross-sections for non-fluorescing substances [52].

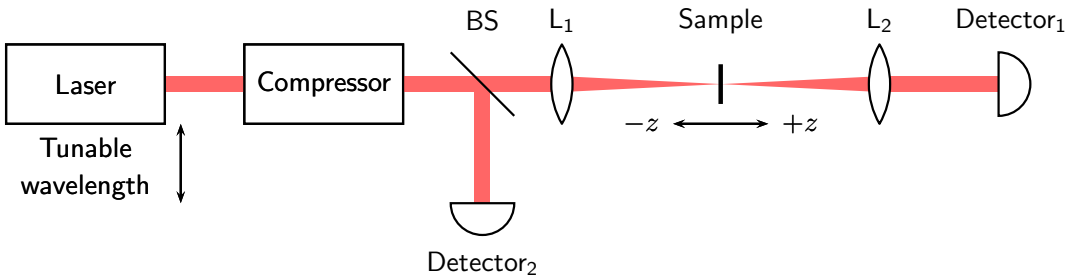

Figure 1.3: Schematic of an open-aperture Z-scan setup based on wavelength-tunable lasers and pulse compression unit. BS: beam splitter; L: lens.

To obtain 2PA spectra using Z-scan, an adequate option would be to introduce a tunable laser source producing ultrashort pulses, for example, an optical parametric amplifier (OPA) or optical parametric oscillator (OPO) and replace the single wavelength source in the conventional Z-scan setup. The central wavelength of an OPA or OPO can be tuned automatically in a wide

spectral range. Therefore, most Z-scan experiments employ such light sources [53–55]. The Z-scan measurements are repeated for different central wavelengths to attain 2PA spectra point-by-point. Ajami et al. have reported spectral-resolved 2PA spectra in the range of 600–950 nm with a resolution of 10 nm repeated 35 times [56].

In principle, Z-scan measures non-linear transmittance as a function of distance z of the sample from the focal point and yields Z-scan traces at different excitation wavelengths. In order to obtain 2PA spectra, the 2PA coefficient $\beta(\lambda)$ at each wavelength λ can be determined by fitting of the normalized transmittance traces $T_{\mathrm{norm}}(z)$ in terms of the sample position z for the respective wavelengths using the following relation:

$$T_{\mathrm{norm}}(z) = 1 - \frac{1}{2\sqrt{2}} \frac{\beta(\lambda) I_0 L_{\mathrm{eff}}}{1 + (\frac{z}{z_{\mathrm{R}}})^2}\,, \tag{1.8}$$

where the effective optical path L_{eff} is expressed as

$$L_{\mathrm{eff}} = \frac{1 - \mathrm{e}^{-\alpha d}}{\alpha}\,, \tag{1.9}$$

and the on-axis intensity of the laser I_0 is given by

$$I_0 = 4\sqrt{\frac{\mathrm{In2}}{\pi}} \frac{P_{\mathrm{avg}}}{\mathrm{M}^2 \lambda z_{\mathrm{R}} R \tau}\,. \tag{1.10}$$

z_{R} is the Rayleigh length of the focused laser beam, α is linear absorption coefficient, d is sample thickness, P_{avg} is average power of the laser, M^2 is beam quality factor, R is repetition rate, and τ is pulse duration. 2PA cross-section values $\sigma^{(2)}$ can thus be calculated from Eq. 1.4 provided that the sample concentration is known.

The magnitude of the I_0 must be known to the respective Z-scan trace to extract the 2PA cross-section. Experimental uncertainties in, e.g., pulse duration, beam waist, and spectral energy significantly affect the 2PA cross-section. Using the proposed approach, 2PA spectra of several recently developed two-photon initiators have been examined [57]. Steiger et al. introduced a fully automated tunable femtosecond oscillator-based Z-scan setup that significantly reduces measurement time to 30 minutes for spectral scanning with 10 nm step from 700 nm to 1000 nm [58]; this setup was used to characterize our coordination polymer samples [59].

Moreover, there is also an alternative choice for obtaining 2PA spectra by scanning central wavelengths, namely using a high-intensity white light continuum (WLC). In WLC Z-scan, a narrow range of the WLC spectrum is selected either by using bandpass filters or by selecting the desired excitation range after a dispersive element using a narrow slit. By changing the filter or displacing the slit, the wavelength of the transmitted light can be easily tuned and utilized to perform the Z-scan at different excitation wavelengths in a point-by-point manner. Again, the 2PA spectra are obtained by fitting Z-scan traces using Eq. 1.4. This method is also feasible for obtaining 2PA spectra but has not been utilized abundantly.

As discussed above, the Z-scan is a simple and powerful single-beam technique used for nonlinear transmission experiments that directly allows us to determine the nonlinear optical coefficients. However, this technique requires movement of the sample along the laser beam across the focal plane of a focusing lens, which in materials with absorption can result in irreversible damage [60]. Taheri et al. introduced a simple and reliable single beam technique to determine the magnitude and the nature of the third-order susceptibility χ^3 with a low damage threshold [61]. In the given method, the sample is placed in a Rayleigh length behind the focal plane of the lens, and the transmission signal is monitored as a function of the input pulse intensity $T(I)$, which yields an intensity-dependent 2PA coefficient. Later, the intensity-scan combined with the microscope objective lens known as μ-I-scan technique allows the imaging of the sample to observe whether the laser spot is tightly focused and exactly irradiates the sample. This is crucial when the sample size is comparable to the focused laser spot. This μ-I-scan technique was described somewhere to investigate nonlinear absorption properties of monolayer single crystal and multilayer triangular islands of transition metal dichalcogenides [62].

Two-photon excited fluorescence (2PEF) is the second most frequently used method for determining 2PA cross sections in nonlinear materials and solvated molecules. Xu and Webb introduced this method for determining 2PA cross sections of fluorescent materials with known fluorescence quantum yields [63]. To obtain 2PA spectra using 2PEF, a tunable femtosecond laser source is required for detecting two-photon induced fluorescence at different excitation wavelengths. The emission signal is recorded by an array detector after spectral dispersion or at a given detection wavelength after filtering. Results are compared to a standard reference with known 2PA cross-section and quantum yields. Several standard references, e.g., dye molecules, are available with reported 2PA cross-section and quantum yield values in the visible–near-infrared range [64]. In 2PEF, the intense incident light at central frequency ω is often spectrally well separated from the emitted light after 2PA (2ω). This means weak emissive features can be recorded after appropriate filtering of the excitation light, making the detection more sensitive. Therefore, the 2PEF method is more sensitive than the Z-scan, with the possibility of faster data collection for materials exhibiting high fluorescence quantum yield with a favorable signal-to-noise ratio.

The rate of 2PA absorption strongly depends on the spatial and temporal coherence of the excitation light. Therefore, it is important to know the relationship between the fluorescence and excitation intensity. Therefore, a 2PEF signal can be measured either with a reference or with the calibration of the setup [63, 64]. 2PEF strength of a sample and standard reference at different excitation wavelengths can be computed using the following equation:

$$F_{\mathrm{2PEF}}(\lambda) = gI^2\eta\phi\sigma^{(2)}(\lambda)N\mathrm{d}s\mathrm{d}z\,, \tag{1.11}$$

where g is the degree of the second-order temporal coherence, I is the laser intensity, η is the fluorescence quantum yield, ϕ is fluorescence collection efficiency of the experimental setup examines all the setup-related parameters, e.g., optical path, sensitivity of the detector, apertures,

collection angle for fluorescence scattering. $\sigma^{(2)}$ is the 2PA cross section, N is the particle density or concentration and $\mathrm{d}s\mathrm{d}z$ is the excitation volume of the focused laser beam. Generally, the results obtained from 2PEF measurements are often presented as a two-photon action cross-section or two-photon brightness ($\eta\sigma^{(2)}$), which evaluates the relative efficiency of the 2PEF. Eq. 1.11 allows us to quantify the ratio of fluorescence intensities of sample and reference at different wavelengths, which is necessary to compute the 2PA spectra. The ratio of fluorescence intensities cancels out the few common terms presented in Eq. 1.11 for sample (s) and reference (r) and provides a simplified following Eq. 1.12, which can be used to compute the 2PA cross-section values at different wavelengths with η (known for both sample and reference).

$$\sigma_{\mathrm{s}}^{(2)}\eta_{\mathrm{s}} = \sigma_{\mathrm{r}}^{(2)}\eta_{\mathrm{r}}\frac{A_{\mathrm{s,\,2PEF}}(\lambda)N_{\mathrm{r}}}{A_{\mathrm{r,\,2PEF}}(\lambda)N_{\mathrm{s}}}\,. \tag{1.12}$$

Here, A_{2PEF} is the integrated area of 2PEF curves for sample and reference. This approach is potentially helpful for quantifying two-photon excitation spectra for liquid and solid samples [26]. Nevertheless, both Z-scan and 2PEF methods are limited to samples with known concentrations that cannot be applied to samples with unknown concentrations or non-uniform distribution of chromophores over the excitation area. Therefore, it is challenging to determine the 2PA cross-section of, e.g., fluorescent semiconductor nanocrystals (quantum dots and nanoplatelets) in diluted solutions and thin films. To overcome this issue, two methods have been proposed for measuring the 2PA cross-section of individual quantum dots. One is based on the fluorescence blinking statistics in semiconductor quantum dots following two-photon excitations, while the other one is based on the photoluminescence saturation effect, which is produced by multiexciton Auger recombination [65, 66]. However, both these methods are limited to individual semiconductor nanocrystals, meaning that ensemble-average values can be estimated only if extensive statistics are achieved. Recently, Krivenkov et al. have studied the saturation of 2PEF in the quantum dots and nanoplatelets by considering a low ratio between fluorescence lifetime and laser pulse period [67]. The authors derived a rate equation based on a well-defined four-level system as an idealized model for the quantum dot. By fitting 2PEF behavior as a function of excitation intensity, the 2PA cross-section was derived without prior knowledge of fluorophore concentration.

1.3.2 Nonlinear Fourier transform spectroscopy

Two-photon Fourier-transform spectroscopy (2P-FTS) is a third alternative with distinct advantages [68]. On the one hand, this technique allows for faster data acquisition as compared to Z-scan measurements at varying central wavelengths. On the other hand — as a time-domain spectrometer — 2P-FTS readily gives a comparatively high spectral resolution as it depends on the maximum scanning range of the interferometer, e.g., Michelson or Mach–Zehnder. 2P-FTS was first used by Bellini et al. to examine the hyperfine structure of atomic energy levels [68]. Ogilvie et al. applied this method to measure two-photon excitation spectra of dye molecules

using an acousto-optic modulator for pulse shaping and a Michelson interferometer to scan the delay [69]. Midorikawa and co-workers combined this method with a 5-fs broadband pulse to measure two-photon excitation spectra of fluorescent proteins [70–72]. In our work, we demonstrate a spectroscopic experiment to measure two-photon excitation spectra based on the common-path birefringent interferometer TWINS (Translating-Wedge-based Identical pulses eNcoding System) [73]. Due to its common-path design, TWINS delivers double pulses with high phase stability and with delay accuracy of $\sim \lambda/300$ at 500 nm [74], which is one order of magnitude higher than in the Michelson geometry [73]. This is advantageous, especially when employing excitation pulses in visible [73, 75] or the UV spectral range [76].

Nonlinear Fourier-transform spectroscopy is based on the measurement of the second-order interferometric autocorrelation (IAC). For a given material showing second-order nonlinear polarization, e.g., 2PEF or second harmonic generation (SHG), the quadratic IAC as a function of time delay can be expressed as

$$S^{(2)}(\tau) = \int_{-\infty}^{+\infty} \left| [E(t) + E(t+\tau)]^2 \right|^2 \mathrm{d}t \,. \tag{1.13}$$

Here, we describe the electric field as

$$E(t) = A(t) \exp(i\omega_0 t) \,, \tag{1.14}$$

where $A(t)$ is the slowly varying amplitude and ω_0 is the central frequency of the electric field. $S^{(2)}(\tau)$ can be decomposed via Fourier transformation into three frequency components, at $\omega \approx 0$, $\omega \approx \pm\omega_0$ and $\omega \approx \pm 2\omega_0$. The power spectrum at frequency $2\omega_0$ is proportional to the product of the response function $R^{(2)}(\omega)$ representing the desired 2PA spectrum and the second harmonic (SH) spectrum [77], provided that the nonlinear optical response of the material scales uniformly with the square of the incident pulse intensity over a spectral range greater than the pulse bandwidth:

$$S^{(2)}_{2\omega_0}(\omega) \propto R^{(2)}(\omega) \left| E^{(2)}(\omega) \right|^2 . \tag{1.15}$$

The SH power spectrum $\left|E^{(2)}(\omega)\right|^2$ can be measured either using a nonlinear SHG crystal, e.g., β-barium borate (BBO) or in the reflection mode from the surface of a quartz substrate [78]. Alternatively, the two-photon-induced photocurrent in a photodiode can also be used to determine the SH spectrum [79]. When the frequency response of the crystal is assumed to be flat over the excitation range [69, 80], the $R^{(2)}(\omega)$ can be obtained by dividing the measured quantity $S^{(2)}_{2\omega_0}(\omega)$ by the SH spectrum $\left|E^{(2)}(\omega)\right|^2$.

A schematic of the experimental design for two-photon fluorescence excitation spectroscopy is shown in Fig. 1.4. The broadband spectrum is generated by a noncollinear optical parametric amplifier (NOPA rainbow) [81, 82] pumped by 60 µJ femtosecond pulses from a mode-locked Yb:KGW laser (Light Conversion, PHAROS PH2) operating at 1024 nm with a variable rep-

etition rate of up to 200 kHz. The input pulses are frequency doubled with 35% efficiency. The resulting 512 nm pulses amplify the seed continuum generated in a 4 mm YAG [83] using a type I phase-matched 3 mm thick BBO crystal cut at 23°. Typical output pulse energies are of the order of 3 µJ corresponding to a quantum efficiency of 35%. The NOPA rainbow was aligned once to the desired spectrum and did not need any readjustment over the course of the measurements.

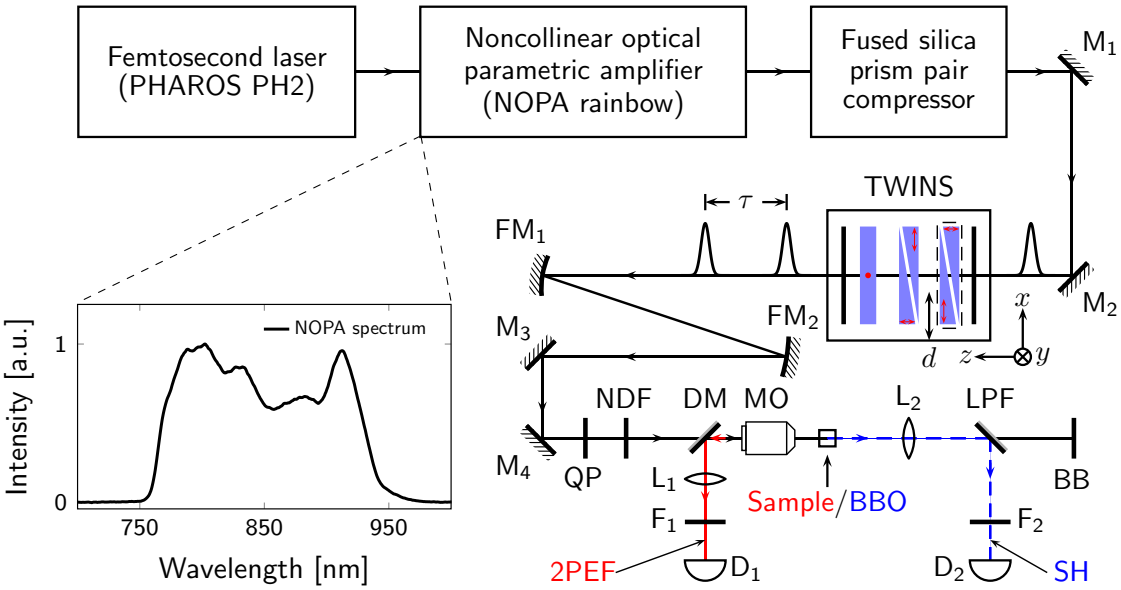

Figure 1.4: Experimental setup for interferometric two-photon excitation spectroscopy. M: mirror; FM: focusing mirror; QP: quartz plate; NDF: neutral density filter; DM: dichroic mirror; MO: microscope objective; L: lens; LPF: long-pass filter; F: filter; BB: beam block; D: detector; TWINS: Translating-Wedge-based Identical pulsed eNcoding System (an interferometer); 2PEF: two-photon excited fluorescence (solid red); SH: second harmonic spectrum (dashed blue). A representative NOPA spectrum is given in the lower left. The red arrows depict the path of the back-reflected 2PEF signal $S^{(2)}_{2\omega_0}(\omega)$.

The NOPA output spectrum is shown in the inset of Fig. 1.4 and covers a spectral range from 750 to 950 nm. The pulses are compressed by a fused silica prism pair to compensate for the dispersion introduced by transmissive optical components in the NOPA and before the sample position. The compressed pulses are directed to the TWINS interferometer (NIREOS, GEMINI-2D), which has been explained in detail elsewhere [74, 84–86]. The transmitted beam is then expanded twice using a reflective telescope and focused on the sample position using a microscope objective (MO; Nikon, CFI S Plan Fluor ELWD 20XC, NA 0.45). Even the large amount of glasses (about 35 mm) in the MO can be compensated by the prism compressor. Second harmonic spectra are recorded for reference purposes before every 2PA measurement. A BBO crystal with a nominal thickness of 10 µm on a fused silica substrate with $\theta = 36.7°$

is used as a nonlinear medium. A long-pass filter (LPF; Edmund Optics, #15-456) allows the fundamental light to pass through but reflects the SH to the detector D_2.

When replacing the BBO crystal with a test sample, 2PEF is detected in the backward direction and imaged onto the detector D_1. This is realized by placing a dichroic mirror (Thorlabs, DMLP650) before the objective. A short-pass filter (F_1) is then used to reject scattered fundamental light. A 1.25 mm quartz plate (QP) compensates for the front cuvette window. The laser intensity is adjusted by a neutral density filter (NDF) to avoid photosaturation of the investigated samples. The current experiment uses a fiber-coupled spectrometer (StellarNet Inc, BLUE-Wave) as the detector. While only the spectrally integrated signal is used for evaluating the 2PA spectra, broadband detection is convenient for measuring both SH and 2PEF signals. Furthermore, broadband detection is necessary for pulse characterization, as discussed below.

The TWINS interferometer follows a similar design as in [84]. It is a common-path interferometer utilizing birefringent materials to generate pulse replicas with variable time delay. Three birefringent blocks fabricated as wedges or plates are arranged with their optical axis along the x-, y- and z-axis, as marked with red arrows in Fig. 1.4. A linear polarizer is used to set the polarization direction of the incoming beam at 45° to the x direction. In this way, two polarization components at x and y direction will see different refractive indices when propagating collinearly along the z direction through the blocks. A second polarizer projects these two components to the same polarization state. The time delay τ between the pulse replicas is determined by translating a birefringent wedge in and out of the beam and can be expressed as

$$\tau = \frac{d \cdot \tan(\alpha) \cdot (n_{\mathrm{go}}(\lambda) - n_{\mathrm{ge}}(\lambda))}{c}\,, \tag{1.16}$$

where d is the displacement of the moving wedge, α is the apex angle of the wedge, $n_{\mathrm{go}}(\lambda)$ and $n_{\mathrm{ge}}(\lambda)$ are the group refractive indices of the ordinary and extraordinary polarization, and c is the speed of light in the free space. The spectral resolution, therefore, is determined by the maximum delay d of the wedge.

2PA cross-sections and, therefore, two-photon excitation spectra do not depend on the pulse duration [87]. This theoretical finding has been verified experimentally using excitation sources in the femtosecond, picosecond, and nanosecond regime [63, 88, 89]. However, shorter pulse durations lead to higher peak intensities at the focal spot and, therefore, to stronger 2PEF signals [90]. This explains the general aim of the shortest pulse duration possible reaching its Fourier limit in 2P-FTS experiments. Hashimoto et al. showed that two-photon excitation spectra do not depend on group delay dispersion (GDD) because any phase distortions can be referenced out by the corresponding SH spectrum, which carries both spectral and phase information of the excitation source [71]. This means that the 2P-FTS approach is robust against variations in pulse compression, even though a structure-free SH spectrum is preferred for normalization purposes.

The above arguments call for a thorough pulse characterization, which we realize *in-situ* via collinear frequency-resolved optical gating (cFROG) [91, 92]. We measure the SH spectrum

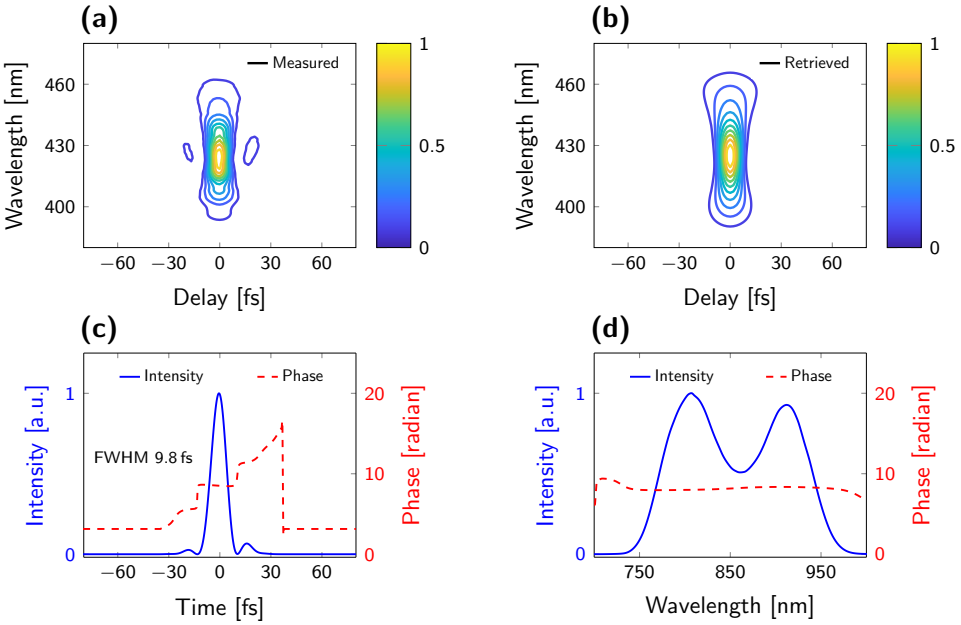

Figure 1.5: Characterization of the laser pulse using cFROG. (a) Measured FROG trace via Fourier filtering of the frequency-resolved IAC traces. (b) Retrieved FROG trace. (c) The retrieved pulse shape and temporal phase. (d) The retrieved power spectrum and spectral phase.

of the laser pulse at the objective's focal point with a 10 µm thick BBO crystal (see above). The frequency-resolved IAC trace is measured using a fiber-coupled spectrometer in the forward direction (dashed blue line in Fig. 1.4). Fourier transformation allows us to extract the standard noncollinear FROG trace, i.e., the intensity autocorrelation trace from the frequency-resolved IAC map, which can be retrieved using the standard FROG algorithm [93]. Pulse compression is necessary due to the GDD introduced by transparent materials, e.g., from the TWINS interferometer, neutral density filter, and microscope objective. These effects elongate the pulses but are pre-compensated using the fused silica prism compressor. Comparison between the measured (Fig. 1.5(a)) and retrieved (Fig. 1.5(b)) FROG traces shows a minimum FROG error of 0.4% and a pulse duration of 9.8 fs (Fig. 1.5(c)). When assuming a Gaussian pulse shape, we note that the given NOPA spectrum (750–950 nm) supports Fourier-transform-limited (FTL) pulses of 6.6 fs. Fourier transformation of the pulse spectrum, as shown in the inset of Fig. 1.4, matches the measured pulse length very well. In general, it is challenging to generate sub-10 fs pulse at the focal point for a tightly focused laser spot [94–96]. In addition, higher-order dispersion cannot be compensated solely by using a prism compressor for such a large bandwidth [97].

To evaluate the performance of our experiment, we have measured the IAC signals of three standard dyes, i.e., fluorescein, rhodamine B, and perylene, for their well-structured spectrum. Fluorescein was dissolved in deionized water to a concentration of 100 µM at pH 11; rhodamine B was prepared in ethanol with a concentration of 120 µM, and perylene was prepared in DCM

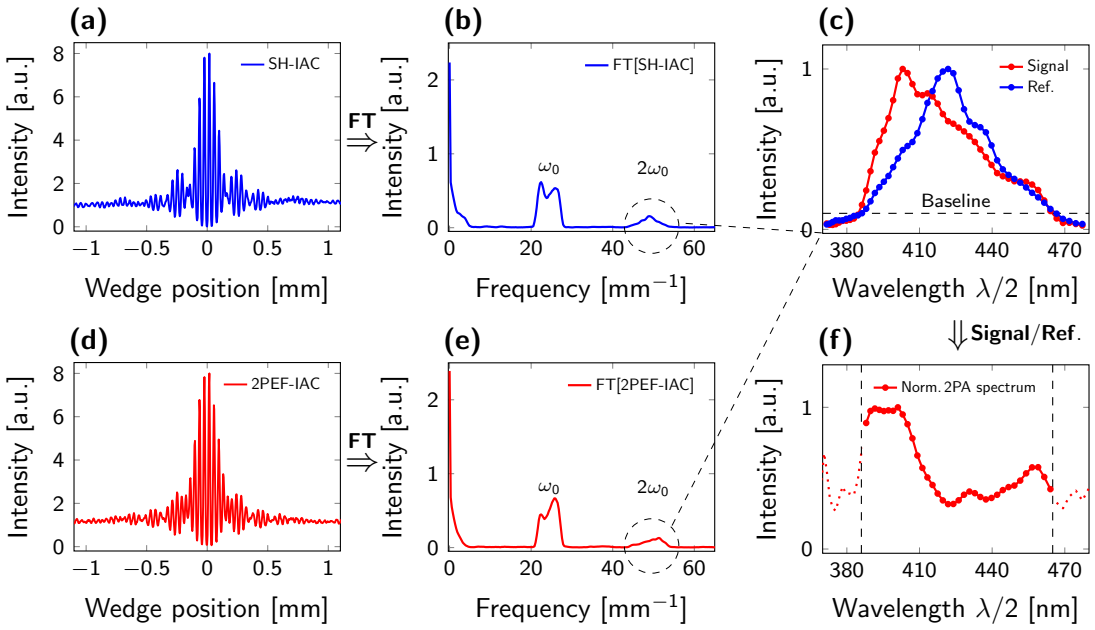

Figure 1.6: Interferometric autocorrelation traces of (a) SH from the BBO crystal and (d) 2PEF from fluorescein as a function of the wedge position d and Fourier spectra of (b) SH and (e) 2PEF. $2\omega_0$ terms of Fourier spectra (highlighted with dashed circles) are plotted together in (c) after axis calibration (please see the text for details); the baseline of the reference spectrum is set at 10% of its maximum intensity (black dashed line). Division by the SH spectrum leads to the normalized two-photon absorption spectrum of the sample (f); the vertical dashed lines limit the spectral range defined by the baseline in (c).

(dichloromethane) with a concentration of 1 mM. We use the case of fluorescein to illustrate the data processing method. Fig. 1.6(a) shows the second harmonic interferometric autocorrelation (SH-IAC) signal of the pump pulse as a function of the wedge position in the TWINS interferometer. Fourier transformation of the SH-IAC gives three well-separated components in the spatial frequency domain as depicted in Fig. 1.6(b). The $2\omega_0$ component representing the SH power spectrum is shown in blue in Fig. 1.6(c). After pulse duration optimization, the BBO crystal is replaced by the test samples to measure the 2PEF signal in the backward direction (see solid red arrows in Fig. 1.4). Fig. 1.6(d) shows the 2PEF-IAC of fluorescein, where the contrast of $I(d=0)/I(d=\infty)=8$ indicates that the setup is well-aligned and at the same time, no effects are leading to photosaturation, photodamage or higher-order absorption. Fourier transformation of the 2PEF-IAC signal yields the spectrum shown in Fig. 1.6(e), which is plotted together with the reference SH spectrum in Fig. 1.6(c). The desired two-photon absorption spectrum is then obtained by dividing the normalized signal spectrum by the normalized SH spectrum shown in Fig. 1.6(f).

Axis calibration from the spatial frequency to the optical frequency and finally to the wavelength domain is needed, i.e., mm^{-1} $\rightarrow$ THz $\rightarrow$ nm, from Fig. 1.6(b) and 1.6(e) to 1.6(c).

Recalling Eq. 1.16, the delay τ induced by one step of the delay stage in the TWINS interferometer is wavelength-dependent due to the difference between the ordinary and extraordinary indices of refraction. The calibration curve correlating spatial frequency and optical frequency is obtained by measuring the frequency-resolved linear autocorrelation of a broadband laser source as a function of the wedge displacement d and the detection wavelength λ, as described in detail in the literature [85, 86]. However, such a calibration procedure has so far only been carried out for the ω_0 component. Following the same protocol, the calibration curve for the $2\omega_0$ term can be determined using a BBO crystal as a nonlinear medium to measure its second-order autocorrelation map.

Two-photon excitation spectra of fluorescein, rhodamine B, and perylene are depicted in Fig. 1.7 compared to those measured with other techniques. To aid comparison, we normalize all spectra in Fig. 1.7 to their respective values at $\lambda/2 = 420\,\text{nm}$, as taken from literature [64]. For the fluorescein sample, we show 2PA spectrum from the fundamental wavelength of 680 nm to 930 nm employing the tunablity of our NOPA spectral range, we find an optimized pulse duration of 20 fs (FTL 18 fs) for spectrum #1, 19 fs (FTL 16 fs) for spectrum #2, 17 fs (FTL 15 fs) for spectrum #3, and 10 fs (FTL 7 fs) for spectrum #4. The resulting 2PA spectra of fluorescein are depicted in Fig. 1.7(b), where we find a nearly quantitative agreement between our results and those of Makarov et al. [64] and Xu et al. [63]. The latter two experiments employed swept-source lasers, namely fluorescence detection, which used either a tunable OPA or a tunable oscillator. Fig. 1.7(b) also shows two-photon excitation spectra obtained with the four different excitation pulses shown in Fig. 1.7(a). Even though excitation spectra may show strong overlap, the respective two-photon excitation spectra may differ. See, e.g., olive and orange dots in Fig. 1.7(b) between 375 nm and 385 nm. In case of such a discrepancy, we prefer the data points obtained with a higher SH-signal intensity. For the measurement of rhodamine B, Steiger et al. employed a tunable femtosecond oscillator [58]. We find good agreement between our results and the literature data.

In Fig. 1.7(c), we show the 2PA spectrum of perylene. The $\sigma^{(2)}$ values are in the single-digit regime, highlighting the sensitivity of our method. Our results for perylene agree with those of Makarov et al. [64]. Comparison to the 1PA spectrum shows a shift of oscillator strength to higher-lying transitions for the 2PA spectrum, which is in agreement with expectation [98]. Our measurement reproduces the structured nature of the vibronic spectrum well and highlights the high spectral resolution of our experiment.

The spectral resolution of a time-domain Fourier transform spectrometer is solely determined by the maximum time delay (maximum wedge displacement d in our case) between the pulse pair. As in our current measurement, we set the maximum wedge displacement at 1.85 mm, which gives us a spectral resolution of 4 nm at 800 nm. With the current interferometer supporting a maximum wedge delay of 28 mm, sub-nm resolution could be easily achieved. However, this comes at the cost of longer data acquisition times and is only useful if the resolution of narrow spectral features is aimed for. Under the experimental conditions described

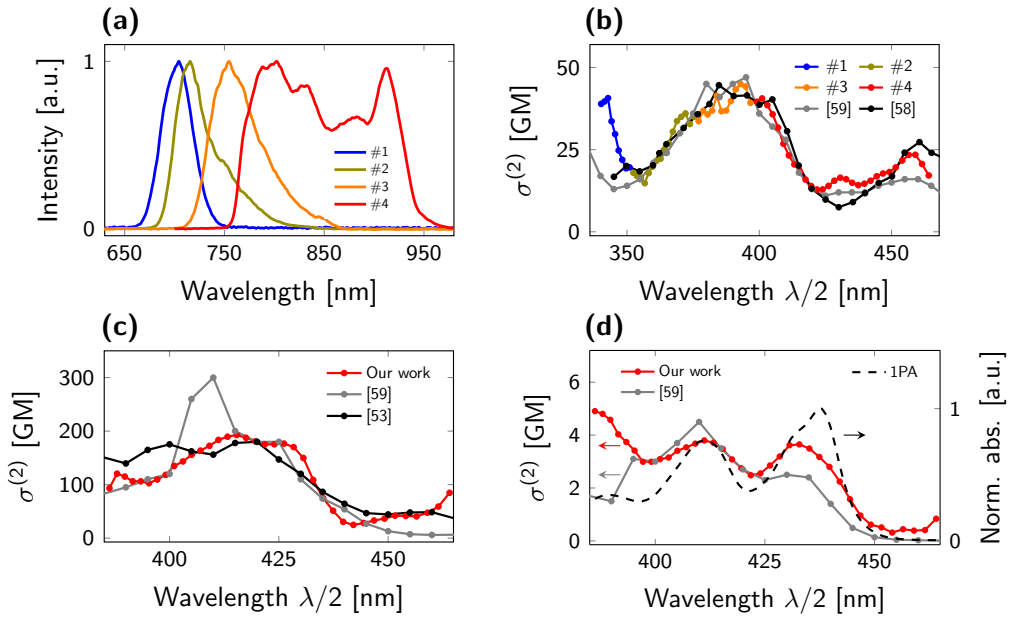

Figure 1.7: (a) Tunable NOPA spectra to cover a broad wavelength range from 650 nm to 950 nm. Two-photon excitation spectra compared with other techniques from the literature (normalization at $\lambda/2 = 420$ nm using Makarov's data in [64] as a reference) are depicted for (b) fluorescein, (c) rhodamine B, and (d) perylene.

here, i.e., at 4 nm resolution, a single 2PA spectrum is recorded in just 5 minutes. Replacement of the fiber-coupled spectrometer with an optimized photodiode detector and implementation of a continuous scan of the TWINS interferometer will further reduce the data acquisition time significantly.

After setup evaluation using standard dyes, we employ our method to characterize a carbazole- and fluorene-based chromophore linker sample H_4fbcd (2,7-fluorene-9,9-dimethyl-bis-carbazole-3,6-dicarboxylic acid) and the corresponding CP $Sr(H_2fbcd)(DMAc)_{0.25}(H_2O)_{3.5}$, featuring the twofold deprotonated and Sr-coordinated linker H_2fbcd [59]. H_4fbcd linker molecules are MPA-active building blocks that hold promise for the synthesis of two-photon enhanced MOFs and CPs. This measurement aims to establish whether incorporating a linker molecule into a CP framework affects its 2PA spectrum [27]. CPs are a versatile material class for the purpose of shaping the 2PA-spectrum of a linker, as the CP-nodes can serve as electron donating or accepting groups. Furthermore, an increase in the linker's 2PA response can be attributed to a CP-specific relative alignment of the linkers, which would not be found for randomly orientated linkers in solution [26]. Here, we investigate the 2PA spectrum of H_4fbcd dissolved in DMF (dimethylformamide) at a concentration of 500 µM and compare it to the respective CP. Due to their low solubility in liquid solvents, crystalline CP powders were prepared in PMMA films. Fig. 1.8(a) shows the absorption spectrum of the solvated linker (solid blue line) in comparison to the CP's diffuse reflectance spectrum (red line). The overlap between the linker's absorption spectrum and the frequency-doubled excitation spectrum (dashed blue line) is negligible, which

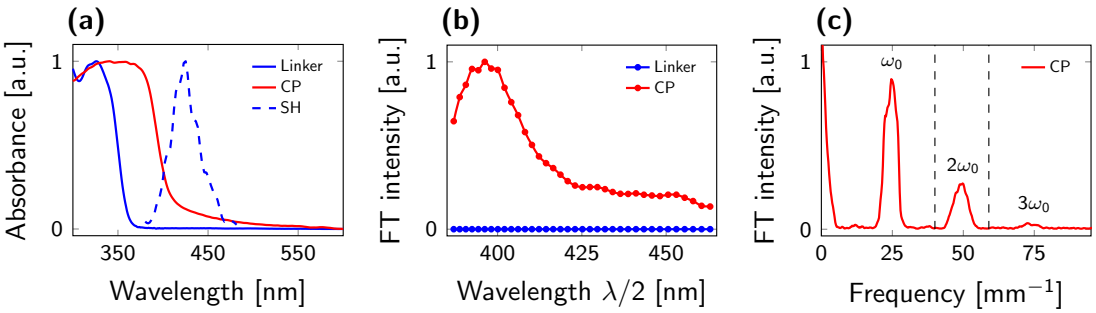

Figure 1.8: (a) UV–Vis absorption spectrum (solid blue) of the solvated H_4fbcd linker sample in DMF together with the diffuse reflectance spectrum (solid red) of the corresponding CP $Sr(H_2fbcd)(DMAc)_{0.25}(H_2O)_{3.5}$ in a film. The SH spectrum (dashed blue) indicates the two-photon excitation energy range available in this work, i.e., 375–475 nm. (b) Two-photon excitation spectra of the H_4fbcd linker and the corresponding CP. (c) Fourier-transformation over the IAC trace of the two-photon induced fluorescence signal from H_4fbcd CP. Components except $2\omega_0$ representing 2PA can be filtered out using a window function (dashed line).

explains the lack of 2PEF we observe from this sample. Accordingly, the 2PA spectrum of the linker in Fig. 1.8(b) is represented by a zero-line. The spectrum of the CP is redshifted as compared to the solvated linker, see red vs. blue line in Fig. 1.8(a). Excitonic interaction of the linker molecules in the CP-environment serves as one possible explanation for this redshift, given that the interchromophore distance is strongly reduced compared to the linker molecules in solution [99]. The enhanced overlap between the frequency-doubled excitation spectrum (SH in Fig. 1.8(a)) and the CP absorption spectrum leads to a measurable 2PA spectrum, see red line in Fig. 1.8(b).

Due to the lack of a reference standard in the PMMA films for calibration, the two-photon excitation spectrum of the CP sample is plotted in arbitrary units in Fig. 1.8(b). However, Z-scan measurements of this CP sample allow us to get the 2PA cross-section values directly, as summarized in a previous publication showing that 2PA can be enhanced up to three orders of magnitude when incorporating H_4fbcd chromophores into CP [59]. As indicated in Fig. 1.8(b), we have observed two-photon induced fluorescence signals from H_4fbcd CP while 2PA for its linker sample is negligible in the current excitation range; a local maximum of 2PA for H_4fbcd CP appears at the fundamental wavelength of 790 nm.

We note that a $3\omega_0$ component can be distinguished from the Fourier spectrum of the CP sample, as depicted in Fig. 1.8(c). This implies coexistence of 2PA and three-photon absorption (3PA). 3PA does not affect the results of the 2PA spectra, as the 3PA component can be suppressed either by adjusting the input intensity until reaching the 2PA regime — i.e., by observing the center-to-background ratio of the IACs — or by Fourier-filtering as indicated by the dashed lines in Fig. 1.8(c). Compared with Z-scan, where one usually needs to fit the trace using either 2PA or MPA fitting functions, nonlinear Fourier-transform spectroscopy is

advantageous in this context as it provides not only an intuitive picture of the relative strength of the MPA contribution but also convenient ways of isolating 2PA components.

Chapter 2

Summary and context of publications

2.1 Coordination polymers based on carbazole-derived chromophore linkers for optimized multiphoton absorption: a structural and photophysical study

Weishäupl, S.J.[†]; Cui, Y.[†]; Deger, S.N.; Syed, H.; Ovsianikov, A.; Hauer, J.; Pöthig, A.; Fischer, R.A.

Chemistry of Materials, **34**(16):7402–7411, **2022**.
DOI: 10.1021/acs.chemmater.2c01525

Chromophore molecules featuring multiphoton absorption (MPA) properties are often limited by their thermal stability and uncontrolled aggregation in concentrated solutions. These effects can be largely suppressed by incorporating chromophore as linkers into metal–organic frameworks (MOFs) and coordination polymers (CPs) for their modular tunability to maintain chemical and thermal stabilities. Enhanced MPA in MOFs and CPs are reported compared to the uncoordinated molecule [26, 27, 100]. Carbazoles acting as electron donors show desirable properties for an MPA-active linker. Therefore, in this publication, we report the synthesis and photophysical characterization of two carbazole-based MPA-active linkers, and three different CPs with carbazole linkers incorporated. Nonlinear optical characterization of CPs was performed using an open-aperture Z-scan setup based on a tunable oscillator to obtain excitation-wavelength dependent two-photon excitation spectra in the range of 700 nm to 950 nm [58].

We synthesized three CPs, $Zn_2(sbcd)(DMAc)_2(H_2O)_{1.5}$, $Sr_2(fbcd)(DMAc)_{0.25}(H_2O)_{3.5}$, and $Ba_2(fbcd)(DMAc)_{2.5}(H_2O)_{1.5}$, which are abbreviated as **Zn-CP**, **Sr-CP**, and **Ba-CP**, respectively. They are based on two MPA-active carbazole-containing chromophore linkers H_4sbcd and H_4fbcd. Linker samples were prepared in liquid solutions while CPs were prepared into PMMA films to define their sample concentration more appropriately, especially compared with

powder samples. This is also an advantage of the Z-scan technique, as it is transmission-based and sets demands for an optimal sample concentration.

Single crystal X-ray diffraction reveals that all three CPs are in two dimensions. Steady-state spectroscopy of the CPs compared to free linkers displays a redshift of the absorption and emission bands due to the dipole interactions of the chromophores inside the solid network. Z-scan analysis of three CPs shows large 2PA cross-sections $\sigma^{(2)}$ of 2 100 to 33 000 GM, which is an enhancement of up to three orders of magnitude in comparison to the solvated linker. When incorporating the same linker H_4fbcd into CPs, **Sr-CP** exhibits a 3-fold increase of $\sigma^{(2)}$ compared with **Ba-CP**. First, this can be explained by the size of metal ions. With the same charge, strontium has a smaller ion radius and thus can polarize the chromophore more, which leads to an enhanced charge transfer (CT) character of the chromophore [101]. Another structure difference points towards the carbazole–carbazole distance between the layers in CPs, which is decreased from 3.65 Å in **Ba-CP** to 3.39 Å in **Sr-CP**. This subtle change may also influence the 2PA cross-section as it is the carbazole units that define the CT character of the ligand [27, 102].

As a perspective, with the topological approach published by Vittal et al. [103], we aim to develop the MPA efficiency of the CPs with pillar-layered structures. This idea leads to the next publication in Section 2.2.

2.2 Influence of chromophore packing on multiphoton absorption in carbazole-based pillar-layered coordination polymers

Deger, S.N.[†]; Cui, Y.[†]; Warnan, J.; Fischer, R.A.; Šanda, F.; Hauer, J.; Pöthig, A.
ACS Applied Optical Materials, **xx**(xx):xxxx–xxxx, **2024**.
DOI: 10.1021/acsaom.4c00080

Coordination polymers are a promising class of modular MPA-active materials. A detailed knowledge of the structure–property relationship or generalized design principles is crucial for synthesizing optical materials with enhanced MPA properties. In this publication, we examine the 2PA property of three carbazole-based CPs by incorporating the pillars with different spatial arrangements; they show enhanced 2PA cross sections compared with a previously synthesized CP containing the same chromophore but not pillar.

In general, pillar-layered MOFs offer the possibility of modifying the structure of MOFs without altering the chromophore linkers or SBUs. Via the introduction of "pillar" (linker) molecules, various aspects such as interlinker distances, pore size, and other structural features can be varied [104], and examples of pillar-layered MOFs have been previously synthesized and investigated toward MPA activity [103, 105–107].

In this publication, we present the synthesis of two pillar-layered Zn-based CPs Zn_{2n}(sbcd)-(bpy)$(DMAc)_{2n}(H2O)_{3n}$ (**CP2**) and Zn_{2n}(sbcd)(bpe)$(DMAc)_{3n}(H_2O)$ (**CP3**) using the linker H_4sbcd (9,9'-stilbene-bis-carbazole-3,6-dicarboxylic acid) with identical metals in the SBUs and chromophore linkers, differing only in the chemical structure of the incorporated "pillars", which are 4,4'-bipyridine (bpy) and 1,2-bis(4-pyridyl)ethane (bpe). This allows for the investigation of a potential structure–property relationship (between the chromophore packing and their NLO properties). The results are compared with the corresponding, pristine two-dimensional (pillar-free) CP structure Zn_{2n}(sbcd)$(DMAc)_{2n}(H_2O)_{1.5n}$ (**CP1**, named as **Zn-CP** in Section 2.1), previously published by our cooperative group [59] for which no direct structure–NLO-property relationship could be established. Compared to those of the nonpillar-layered **CP1**, the obtained data for **CP2** and **CP3** show the increase of $\sigma^{(2)}$. This indicates that the pillar-layering approach is a potential avenue to get a more comprehensive understanding of the effects of structural changes on the MOF's NLO properties and control as well as improve them.

Compared with the excitation spectrum of the linker H_4sbcd, all three CPs show a redshift of approximately 50 nm and broadening. This can be explained by a higher excitonic interaction in the CPs than in the linker [59]. Besides, This effect may also point towards structure rigidification or interligand charge transfer [108–111]. For the case of emission spectra compared with the linker, **CP1** shows a redshift of 25 nm while **CP2** and **CP3** show a redshift up to 60 nm. The observed redshift in CPs compared to the linker is rationalized by two structural effects. First, the π–π interactions between adjacent linker molecules in the solid state may facilitate efficient intermolecular interactions through π-stacking [112]. Second, the increased planarity of the linker in **CP2** and **CP3** as compared to **CP1** may maximize the intramolecular π-

orbital overlap and promote further π–π interactions, explaining the extra shift of the emission band [113, 114].

Nonlinear optical characterization of the linker and CPs was conducted via nonlinear Fourier-transform spectroscopy, as described in detail in Section 1.3.2. The NLO characterization demonstrated enhanced 2PA in the CPs compared to the free linker, with **CP3** exhibiting a remarkable 2.4-fold increase in $\sigma^{(2)}$ compared to **CP2** and 3.2-fold increase over **CP1**. The coplanar alignment of chromophores in **CP3**, along with its 3D structure, likely contributes to this increase, emphasizing the importance of structural considerations influencing the 2PA activity. Accordingly, future CP design should target rigid 3D structures with closely packed chromophores to obtain a high 2PA activity. On a more general level, we find that fine-tuning nonresonant levels has the potential to strongly increase 2PA activity, for centrosymmetric linkers such as stilbene, the desired redshift of nonresonant levels is accompanied by a — maybe subtle — bathochromic shift of the one-photon absorption spectrum. This could be further probed by impedance spectroscopy to further study the influence of the polarization and dielectric constant of the MOFs on the nonresonant levels [115, 116].

The obtained pillar-layered CPs have the highest $\sigma^{(2)}$ among other pillared-layer CPs. The first synthesized pillar-layered CPs by Vittal et al. using the An2Py linker reached values of up to 32.7 GM [105, 107, 117]. Fischer and colleagues synthesized pillar-layered CPs using the MPA-active linker tetra-(4-carboxylphenyl)ethylene (H_4TCPE), reaching values of up to 476 GM, and Vittal et al. improved on this with values up to 74 000 GM by changing the used pillars [103, 106]. This competitive performance of pillar-layered systems shows the potential of carbazole-based chromophores in MPA-active CPs and MOFs.

The findings show that the pillar-layering approach is a potent way to produce varied CP materials implementing the same chromophores. It generally contributes to the broader field of CPs and their potential applications in nonlinear optical devices.

Chapter 3

Conclusion and outlook

MPA is a nonlinear optical effect widely used in various optoelectronic applications. MPA-active CPs are of high interest in material science and nonlinear optics due to their modular design and versatile applications. To understand the structure–property relationship in those functional materials, especially the chromophore incorporation into CPs and the enhanced 2PA properties, we have implemented a common-path birefringent interferometer with 10-fs pulses to measure broadband two-photon excitation spectra via nonlinear Fourier-transform spectroscopy. Standard dye molecules were measured to evaluate our setup before extending the approach to chromophore linkers and their CPs. The experiment presented in this work is compact, alignment-friendly, and allows for user-defined spectral resolution as well as fast data acquisition.

Together with a fully-automated Z-scan setup designed previously [58], we are able to measure 2PA spectra (and 2PA cross-sections) for both solvated chromophore linkers and their corresponding CPs prepared into thin films. Method of choice mainly depends on the quantum yield of the substances under investigation, e.g., Z-scan is used for non-emissive samples to give 2PA cross-section values directly; 2P-FTS is a fluorescence-based technique to significantly reduce data acquisition time.

We demonstrated 2PA enhancement of up to three orders of magnitude after incorporating carbazole-containing chromophores linkers into CPs. We hypothesize that, besides the excitonic interaction of the linkers within the CPs, the choice of different metal nodes can also alter 2PA activity [59]. Based on this finding, we tested two new CPs using the same chromophore as in reference [59] but with a different spatial chromophore arrangement, the so-called pillared layer. The further enhanced 2PA in pillar-layered CPs can be explained by structure rigidification and coplanarity of chromophores in CPs. We also discussed the influence of 2PA by fine-tuning nonresonant levels of centrosymmetric linkers in CPs [118].

Two research directions are proposed for future work based on the current setup. The first is to investigate polarization-dependent 2PA in CP crystals. The second is constructing an experiment for a novel time-resolved spectroscopic method called ultrafast two-dimensional fluorescence excitation spectroscopy (2D-FLEX) [119].

The research presented in this thesis can be readily expanded toward implementing polarization control, addressing the problem of anisotropic 2PA in CP crystals. Recalling Eqs. 1.5 and 1.6, where we have components of the dipole moment operator along the polarization direction of the excitation light field, it is evident that the absorption cross section is polarization-dependent. This polarization effect is averaged out for an isotropic sample, e.g., in a chromophore linker solution where molecules are randomly oriented. Hence, one gets the same cross-section values regardless of the laser's polarization states. However, the situation may differ for ordered samples such as CP crystals. In an extreme case, such a crystal may be two-photon transparent along one axis but two-photon absorbing along another axis [11].

Polarization-dependent 2PA in CPs may lead to potential applications of polarization-dependent NLO devices, such as optical switches and sensors. Ji and co-workers examined 2PA and second-harmonic generation in a single crystal of Ag(I) complex. They showed that two-photon excited fluoresce intensities reach a maximum change of ten times by varying the input polarization [120]. The authors measured this using a 1030 nm laser with a pulse width of 150 fs. Therefore, switching the excitation source from single wavelength to broadband 10-fs pulses is natural and may provide rich information about those CPs.

CP crystals are usually small, with a maximum size of several hundreds of micrometers. Using the microscope objective installed in the current setup, we already integrated an imaging unit with a resolution of 10 µm so it is safe to find the crystal position and focus the laser beam on it. CP crystal will be held using a goniometer to set the relative angle between the crystal axis and the polarization direction of the excitation laser.

Transient absorption (TA) is the most widespread method in ultrafast spectroscopy. The time-dependence of the recorded signals reports on population and coherence dynamics on electronic ground- and excited states. While TA signals are comprehensive, they suffer under spectral overlap, hindering a straightforward analysis of the underlying dynamics. In the context of photochemical transformation, it would be advantageous to have a method exclusively reporting on excited state processes, as ground state dynamics are not contributing to photoproduct formation. This makes fluorescence an attractive observable. In an effort to maximize spectroscopic information content, changes in the fluorescence spectrum should be recorded on an ultrafast timescale as provided by fluorescence upconversion experiments [121]. Furthermore, the signal should be recorded in frequency dispersion, both for excitation and emission. The step towards excitation frequency resolution takes us from fluorescence upconversion to 2D-FLEX, which will be detailed below.

2D-FLEX is an ideal spectroscopic method as (i) it is ultrafast by employing two-photon excitation with sub-10 fs pump pulses from a NOPA; (ii) it is multidimensional as excitation frequency dependence is retrieved in a Fourier-transform approach, analogous to 2D electronic spectroscopy (2D-ES) [122], and crucially, (iii) 2D-FLEX is selective to excited states as the molecular observable is fluorescence. The prospect of readily isolating excited state dynamics in 2D-FLEX is promising but calls for ultra-broadband excitation pulses and optimized time

resolution. Furthermore, fluorescence signals need to be broadband detected and recorded at different delay times for subsequent Fourier transformation.

In essence, 2D-FLEX requires broadband detection of a time-gated fluorescence signal after double-pulse excitation. The most widespread technique to resolve fluorescence signals on femtosecond timescales is fluorescence upconversion [121, 123–126]. Briefly, fluorescence from a photo-excited sample is amplified by an ultrashort gating pulse in a nonlinear medium such as a BBO crystal to create a sum-frequency or upconverted signal. Kerr-gating experiments also allow for broadband and time-resolved detection of fluorescence [127]. As a disadvantage, this method relies on a high extinction ratio of the employed crossed polarizers to suppress unwanted, slowly decaying signal backgrounds. This issue is avoided in fluorescence upconversion by spatial separation of the upconverted signal, which explains the high signal-to-noise levels in this technique [121]. Joo and co-workers have demonstrated that 33 fs time resolution is possible by employing two-photon excitation with 20 fs pump pulses at 800 nm [128]. Temporal resolution is crucial to resolve vibronic beating signals as it scales inversely with the maximal beating frequency that can still be resolved. A more standard realization of fluorescence upconversion yields temporal resolutions of 80 fs [121]. Two-photon excitation as employed in this thesis bears several advantages in the context of time-resolved fluorescence. First, theory predicts a reduction in time resolution as compared to one-photon absorption by a factor of $\sqrt{2}$ [129]. Second, fluorescence collection efficiency is higher after two-photon excitation due to the strongly reduced excitation volume. Third, the probability of photodamage is lowered as the central wavelength of the driving pulses must be far detuned from optical resonances in the sample.

A general disadvantage of fluorescence upconversion is the demand for high-intensity NIR gate pulses, calling for an optical parametric amplifier. This is in addition to the laser source used for pumping the sample. NOPA technology is a promising alternative [130–132]. When using a NOPA process to amplify and time resolve a fluorescence signal (NOPA-FL), gain factors of up to 10^6 were observed [133]. It has been shown that the detection limit for NOPA-based approaches is five attojoules, corresponding to 15 photons at 580 nm [133]. This high sensitivity is advantageous for 2D-FLEX, where the excitation frequency axis is retrieved from Fourier transformation (FT) of weak modulations of signal intensities at different delays. Another advantage of NOPA-FL is that the fluorescence photons are amplified directly without changing the frequency, as in fluorescence upconversion. This mitigates the problems of less sensitive detection in the UV range. The time resolution in NOPA-FL is given by the amplifying pump pulse in the BBO crystal. Experimental time resolutions on the order of 100 fs have been shown [132], yet no systematic attempts for optimization have been reported.

The successfully tested 2P-FTS spectrometer depicted in Fig. 1.4 forms the basis for the proposed 2D-FLEX experiment. The FT along the TWINS-induced delay leads to excitation frequency resolution in 2D-FLEX spectra. The rest of the work is to upgrade the existing 2P-FTS spectrometer to a 2D-FLEX experiment with NOPA-FL detection and optimized time

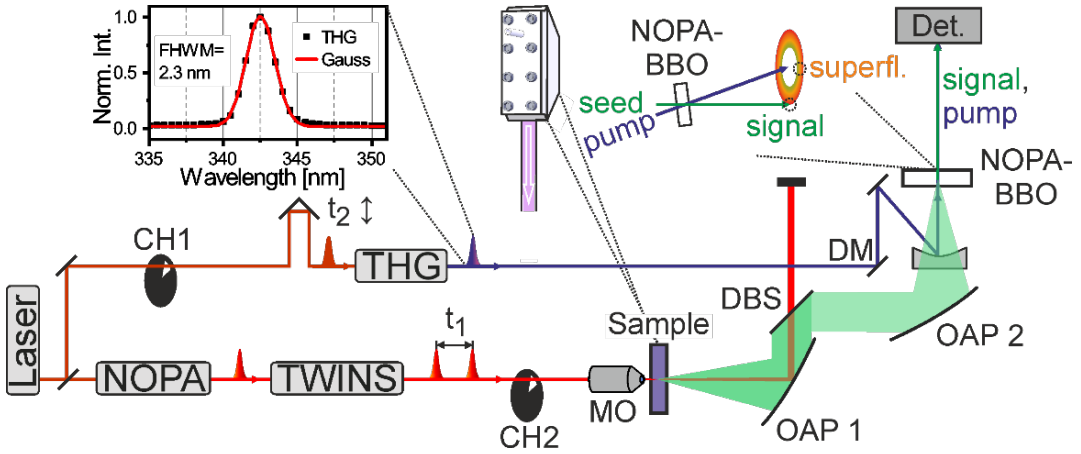

Figure 3.1: Experimental realisation of 2D-FLEX. A NOPA pulse is turned into a double pulse in a commercial double pulse interferometer (TWINS). An off-axis parabolic mirror (OAP 1) collates the two-photon-induced fluorescence of a sample in a wire-guided jet (green). A dichroic beamsplitter (DBS) separates the excitation light from the fluorescence light, which gets focussed onto a BBO-crystal for amplification (NOPA-BBO). The amplifying pump pulse is derived from the fundamental laser beam's third harmonic generation (THG).

resolution. The corresponding experimental design is shown in Fig. 3.1. Instead of detecting fluorescence in back reflection (see Fig. 1.4), we propose to measure the fluorescence transmitted through a window-free flow jet [134, 135]. The lack of cuvette walls decreases pump light scatter and avoids any additional chirping of the fluorescence light, aiding broadband amplification in detection by NOPA-FL. The 2PEF is then collimated by an off-axis parabolic mirror (OAP 1) and imaged onto the NOPA-BBO using OAP 2 for amplification. The pump pulse is the fundamental laser's third harmonic generation (THG) with its measured parameters given in Fig. 3.1. When choosing optimal parameters for the NOPA-FL process, the pump intensity and the crystal thickness must be considered to obtain a high gain ratio and optimal time resolution. In summary, 2D-FLEX is a novel and highly promising spectroscopic method, building up on the two-photon excitation experiment designed, implemented, and tested in this thesis.

Bibliography

[1] Maria Göppert-Mayer. Über Elementarakte mit zwei Quantensprüngen. *Annalen der Physik*, 401(3):273–294, 1931.

[2] W. Kaiser and C. G. B. Garrett. Two-photon excitation in CaF_2:Eu^{2+}. *Physical Review Letters*, 7:229–231, 1961.

[3] T. H. Maiman. Stimulated optical radiation in ruby. *Nature*, 187(4736):493–494, 1960.

[4] Robin M. Hochstrasser, J. E. Wessel, and H. N. Sung. Two-photon excitation spectrum of benzene in the gas phase and the crystal. *The Journal of Chemical Physics*, 60(1):317–318, 1974.

[5] E. Riedle, H. J. Neusser, and E. W. Schlag. Electronic spectra of polyatomic molecules with resolved individual rotational transitions: Benzene. *The Journal of Chemical Physics*, 75(9):4231–4240, 1981.

[6] W. Denk, J. H. Strickler, and W. W. Webb. Two-photon laser scanning fluorescence microscopy. *Science*, 248(4951):73–76, 1990.

[7] Guang S. He, Jayant D. Bhawalkar, Chan F. Zhao, and Paras N. Prasad. Optical limiting effect in a two-photon absorption dye doped solid matrix. *Applied Physics Letters*, 67(17):2433–2435, 1995.

[8] En-Shinn Wu, James H. Strickler, W. R. Harrell, and Watt W. Webb. Two-photon lithography for microelectronic application. In John D. Cuthbert, editor, *Optical/Laser Microlithography V*, volume 1674, pages 776–782. International Society for Optics and Photonics, SPIE, 1992.

[9] Shoji Maruo, Osamu Nakamura, and Satoshi Kawata. Three-dimensional microfabrication with two-photon-absorbed photopolymerization. *Optics Letters*, 22(2):132–134, 1997.

[10] Victor Mizrahi, K. W. DeLong, G. I. Stegeman, M. A. Saifi, and M. J. Andrejco. Two-photon absorption as a limitation to all-optical switching. *Optics Letters*, 14(20):1140–1142, 1989.

[11] Guang S. He, Loon-Seng Tan, Qingdong Zheng, and Paras N. Prasad. Multiphoton absorbing materials: molecular designs, characterizations, and applications. *Chemical Reviews*, 108(4):1245–1330, 2008.

[12] Miłlosz Pawlicki, Hazel A. Collins, Robert G. Denning, and Harry L. Anderson. Two-photon absorption and the design of two-photon dyes. *Angewandte Chemie International Edition*, 48(18):3244–3266, 2009.

[13] Koji Ohta and Kenji Kamada. Theoretical investigation of two-photon absorption allowed excited states in symmetrically substituted diacetylenes by *ab initio* molecular-orbital method. *The Journal of Chemical Physics*, 124(12):124303, 2006.

[14] P. N. Butcher and D. Cotter. *The Elements of Nonlinear Optics*. Cambridge University Press, Cambridge, 1990.

[15] M. Born and K. Huang. *Dynamic Theory of Crystal Lattices*. Oxford University Press, Oxford, 2002.

[16] T. Buckup, J. Dorn, J. Hauer, S. Härtner, N. Hampp, and M. Motzkus. The photoinduced cleavage of coumarin dimers studied with femtosecond and nanosecond two-photon excitation. *Chemical Physics Letters*, 439(4):308–312, 2007.

[17] Fritjof Helmchen and Winfried Denk. Deep tissue two-photon microscopy. *Nature Methods*, 2(12):932–940, 2005.

[18] Grant Walters, Brandon R. Sutherland, Sjoerd Hoogland, Dong Shi, Riccardo Comin, Daniel P. Sellan, Osman M. Bakr, and Edward. H. Sargent. Two-photon absorption in organometallic bromide perovskites. *ACS Nano*, 9(9):9340–9346, 2015.

[19] Weiwei Liu, Jun Xing, Jiaxin Zhao, Xinglin Wen, Kai Wang, Peixiang Lu, and Qihua Xiong. Giant two-photon absorption and its saturation in 2d organic–inorganic perovskite. *Advanced Optical Materials*, 5(7):1601045, 2017.

[20] Feng Zhou, Xing Ran, Dianyuan Fan, Shunbin Lu, and Wei Ji. Perovskites: Multiphoton absorption and applications. *Advanced Optical Materials*, 9(23):2100292, 2021.

[21] Lauren E. Kreno, Kirsty Leong, Omar K. Farha, Mark Allendorf, Richard P. Van Duyne, and Joseph T. Hupp. Metal–organic framework materials as chemical sensors. *Chemical Reviews*, 112(2):1105–1125, 2012.

[22] Hongli Wang, Zhen Li, Pin Shao, Jingui Qin, and Zhen-Li Huang. Two-photon absorption property of a conjugated polymer: Influence of solvent and concentration on its property. *The Journal of Physical Chemistry B*, 114(1):22–27, 2010.

[23] Jian Li Hua, Bo Li, Fan Shun Meng, Fang Ding, Shi Xiong Qian, and He Tian. Two-photon absorption properties of hyperbranched conjugated polymers with triphenylamine as the core. *Polymer*, 45(21):7143–7149, 2004.

[24] Sebastian J. Weishäupl, David C. Mayer, Erling Thyrhaug, Jürgen Hauer, Alexander Pöthig, and Roland A. Fischer. A nitrophenyl-carbazole based push-pull linker as a building block for non-linear optical active coordination polymers: A structural and photophysical study. *Dyes and Pigments*, 186:109012, 2021.

[25] Alexander J. C. Kuehne and Malte C. Gather. Organic lasers: Recent developments on materials, device geometries, and fabrication techniques. *Chemical Reviews*, 116(21):12823–12864, 2016.

[26] Raghavender Medishetty, Jan K. Zaręba, David Mayer, Marek Samoć, and Roland A. Fischer. Nonlinear optical properties, upconversion and lasing in metal–organic frameworks. *Chemical Society Review*, 46:4976–5004, 2017.

[27] Sebastian J. Weishäupl, David C. Mayer, Yang Cui, Pushpendra Kumar, Harald Oberhofer, Roland A. Fischer, Jürgen Hauer, and Alexander Pöthig. Recent advances of multiphoton absorption in metal–organic frameworks. *Journal of Materials Chemistry C*, 10:6912–6934, 2022.

[28] Stuart R. Batten, Neil R. Champness, Xiao-Ming Chen, Javier Garcia-Martinez, Susumu Kitagawa, Lars Öhrström, Michael O'Keeffe, Myunghyun Paik Suh, and Jan Reedijk. Coordination polymers, metal–organic frameworks and the need for terminology guidelines. *CrystEngComm*, 14(9):3001–3004, 2012.

[29] Stuart R. Batten, Neil R. Champness, Xiao-Ming Chen, Javier Garcia-Martinez, Susumu Kitagawa, Lars Öhrström, Michael O'Keeffe, Myunghyun Paik Suh, and Jan Reedijk. Terminology of metal–organic frameworks and coordination polymers (IUPAC Recommendations 2013). *Pure and Applied Chemistry*, 85(8):1715–1724, 2013.

[30] James H. Strickler and Watt W. Webb. 3-D optical data storage by two-photon excitation. *Advanced Materials*, 5(6):479–481, 1993.

[31] Shuangyan Liu, Shencheng Fu, Xintong Zhang, Xinnong Wang, Lihong Kang, Xiuxiu Han, Xi Chen, Jiarui Wu, and Yichun Liu. UV-resistant holographic data storage in noble-metal/semiconductor nanocomposite films with electron-acceptors. *Optical Materials Express*, 8(5):1143–1153, 2018.

[32] A. S. Dvornikov, E. P. Walker, and P. M. Rentzepis. Two-photon three-dimensional optical storage memory. *The Journal of Physical Chemistry A*, 113(49):13633–13644, 2009.

[33] S. Sanyal, A. Painelli, S. K. Pati, F. Terenziani, and C. Sissa. Aggregates of quadrupolar dyes for two-photon absorption: the role of intermolecular interactions. *Physical Chemistry Chemical Physics*, 18:28198–28208, 2016.

[34] Shunzhi Wang, C. Michael McGuirk, Andrea d'Aquino, Jarad A. Mason, and Chad A. Mirkin. Metal–organic framework nanoparticles. *Advanced Materials*, 30(37):1800202, 2018.

[35] A. Morsali and L. Hashemi. Nanoscale coordination polymers: Preparation, function and application. In Daniel Ruiz-Molina Rudi van Eldik, editor, *Advances in Inorganic Chemistry*, volume 76, chapter 2, pages 33–72. Academic Press, 2020.

[36] Omar M. Yaghi. Reticular chemistry—construction, properties, and precision reactions of frameworks. *Journal of the American Chemical Society*, 138(48):15507–15509, 2016.

[37] Hao Jiang, Dalal Alezi, and Mohamed Eddaoudi. A reticular chemistry guide for the design of periodic solids. *Nature Reviews Materials*, 6(6):466–487, 2021.

[38] Chen Cao, Shu-Jin Bao, Xiao-Yan Tang, Ze-Ming Xu, Chun-Yan Ni, and Jian-Ping Lang. Heterobimetallic cluster-based coordination polymers: Assembly, structures and third-order nonlinear optical properties. *Chemistry An Asian Journal*, 16(18):2674–2680, 2021.

[39] Mayank Gupta, Dileep Kottilil, Kapil Tomar, Shunbin Lu, C. Vijayan, Wei Ji, and Parimal K. Bharadwaj. Two-photon absorption and fluorescence in micrometer-sized single crystals of a rhodamine b coordinated metal–organic framework. *ACS Applied Nano Materials*, 1(10):5408–5413, 2018.

[40] David C. Mayer, Aurora Manzi, Raghavender Medishetty, Benedikt Winkler, Christian Schneider, Gregor Kieslich, Alexander Pöthig, Jochen Feldmann, and Roland A. Fischer. Controlling multiphoton absorption efficiency by chromophore packing in metal–organic frameworks. *Journal of the American Chemical Society*, 141(29):11594–11602, 2019.

[41] Yihua Jiang, Yaochuan Wang, Jianli Hua, Jin Tang, Bo Li, Shixiong Qian, and He Tian. Multibranched triarylamine end-capped triazines with aggregation-induced emission and large two-photon absorption cross-sections. *Chemical Communications*, 46(26):4689–4691, 2010.

[42] Zhichao Hu, Guangxi Huang, William P. Lustig, Fangming Wang, Hao Wang, Simon J. Teat, Debasis Banerjee, Deqing Zhang, and Jing Li. Achieving exceptionally high luminescence quantum efficiency by immobilizing an AIE molecular chromophore into a metal–organic framework. *Chemical Communications*, 51(15):3045–3048, 2015.

[43] P. Sperber and A. Penzkofer. S_0–S_n two-photon absorption dynamics of rhodamine dyes. *Optical and Quantum Electronics*, 18(5):381–401, 1986.

[44] Lee W. Tutt and Thomas F. Boggess. A review of optical limiting mechanisms and devices using organics, fullerenes, semiconductors and other materials. *Progress in Quantum Electronics*, 17(4):299–338, 1993.

[45] M. Sheik-Bahae, A. A. Said, and E. W. Van Stryland. High-sensitivity, single-beam n^2 measurements. *Optics Letters*, 14(17):955–957, 1989.

[46] P. B. Chapple, J. Staromlynska, J. A. Hermann, T. J. Mckay, and R. G. Mcduff. Single-beam Z-scan: measurement techniques and analysis. *Journal of Nonlinear Optical Physics & Materials*, 06(03):251–293, 1997.

[47] R. L. Sutherland. *Handbook of Nonlinear Optics*. Marcel Dekker, 1996.

[48] P. Zinsli P. Esherick and M. A. El-Sayed. The low energy two-photon spectrum of pyrazine using the phosphorescence photoexcitation method. *Chemical Physics*, 10(2):415–432, 1975.

[49] L. Singer, Z. Baram, A. Ron, and S. Kimel. The two-photon phosphorescence excitation spectrum of triphenylene. *Chemical Physics Letters*, 47(2):372–376, 1977.

[50] D. S. Kliger A. J. Twarowski. Multiphoton absorption spectra using thermal blooming: I. Theory. *Chemical Physics*, 20(2):253–258, 1977.

[51] David S. Kliger. Thermal lensing: a new spectroscopic tool. *Accounts of Chemical Research*, 13(5):129–134, 1980.

[52] S. S. Chunosova, Valerii A. Svetlichnyi, and Yu. P. Meshalkin. Measurement of the two-photon absorption cross sections of dicyanomethylene-pyrans by the z-scan method. *Quantum Electronics*, 35(5):415–418, 2005.

[53] D. L. Silva, L. Misoguti, and C. R. Mendonça. Control of two-photon absorption in organic compounds by pulse shaping: Spectral dependence. *The Journal of Physical Chemistry A*, 113(19):5594–5597, 2009.

[54] Shaul Pearl, Shlomo Fastig, Yosef Ehrlich, and Raphael Lavi. Limited efficiency of a silver selenogallate optical parametric oscillator caused by two-photon absorption. *Applied Optics*, 40(15):2490–2492, 2001.

[55] Ioulia B. Zotova and Yujie J. Ding. Optical parametric oscillators in the presence of strong two-photon absorption for extended applications of nonlinear optical materials. *Optics Communications*, 198(4):453–458, 2001.

[56] Aliasghar Ajami, Wolfgang Husinsky, Aleksandr Ovsianikov, and Robert Liska. Dispersive white light continuum single Z-scan for rapid determination of degenerate two-photon absorption spectra. *Applied Physics B*, 124(7):142, 2018.

[57] Aliasghar Ajami, Wolfgang Husinsky, Maximilian Tromayer, Peter Gruber, Robert Liska, and Aleksandr Ovsianikov. Measurement of degenerate two-photon absorption spectra of a series of developed two-photon initiators using a dispersive white light continuum Z-scan. *Applied Physics Letters*, 111(7):071901, 2017.

[58] Wolfgang Steiger, Peter Gruber, Dominik Theiner, Agnes Dobos, Markus Lunzer, Jasper Van Hoorick, Sandra Van Vlierberghe, Robert Liska, and Aleksandr Ovsianikov. Fully automated Z-scan setup based on a tunable fs-oscillator. *Optical Materials Express*, 9(9):3567–3581, 2019.

[59] Sebastian J. Weishäupl, Yang Cui, Simon N. Deger, Hamad Syed, Aleksandr Ovsianikov, Jürgen Hauer, Alexander Pöthig, and Roland A. Fischer. Coordination polymers based on carbazole-derived chromophore linkers for optimized multiphoton absorption: A structural and photophysical study. *Chemistry of Materials*, 34(16):7402–7411, 2022.

[60] P. N. Prasad and D. J.Williams. *Introduction to Nonlinear Optical Effects in Molecules and Polymers,*. Wiley, 1991.

[61] Bahman Taheri, Huimin Liu, B. Jassemnejad, D. Appling, Richard C. Powell, and J. J. Song. Intensity scan and two photon absorption and nonlinear refraction of c60 in toluene. *Applied Physics Letters*, 68(10):1317–1319, 1996.

[62] Yuanxin Li, Ningning Dong, Saifeng Zhang, Xiaoyan Zhang, Yanyan Feng, Kangpeng Wang, Long Zhang, and Jun Wang. Giant two-photon absorption in monolayer MoS_2. *Laser & Photonics Reviews*, 9(4):427–434, 2015.

[63] Chris Xu and Watt W. Webb. Measurement of two-photon excitation cross sections of molecular fluorophores with data from 690 to 1050 nm. *Journal of the Optical Society of America B*, 13(3):481–491, 1996.

[64] Nikolay S. Makarov, Mikhail Drobizhev, and Aleksander Rebane. Two-photon absorption standards in the 550–1600 nm excitation wavelength range. *Optics Express*, 16(6):4029–4047, 2008.

[65] Kevin T. Early and David J. Nesbitt. Ultrafast laser studies of two-photon excited fluorescence intermittency in single CdSe/ZnS quantum dots. *Nano Letters*, 15(12):7781–7787, 2015.

[66] Zengle Cao, Bihu Lv, Huichao Zhang, Yan Lv, Chunfeng Zhang, Yong Zhou, Xiaoyong Wang, and Min Xiao. Two-photon excited photoluminescence of single perovskite nanocrystals. *The Journal of Chemical Physics*, 151(15):154201, 2019.

[67] Victor Krivenkov, Pavel Samokhvalov, Daria Dyagileva, Alexander Karaulov, and Igor Nabiev. Determination of the single-exciton two-photon absorption cross sections of semiconductor nanocrystals through the measurement of saturation of their two-photon-excited photoluminescence. *ACS Photonics*, 7(3):831–836, 2020.

[68] M. Bellini, A. Bartoli, and T. W. Hänsch. Two-photon Fourier spectroscopy with femtosecond light pulses. *Optics Letters*, 22(8):540–542, 1997.

[69] Jennifer P. Ogilvie, Kevin J. Kubarych, Antigoni Alexandrou, and Manuel Joffre. Fourier transform measurement of two-photon excitation spectra: applications to microscopy and optimal control. *Optics Letters*, 30(8):911–913, 2005.

[70] Keisuke Isobe, Akira Suda, Masahiro Tanaka, Fumihiko Kannari, Hiroyuki Kawano, Hideaki Mizuno, Atsushi Miyawaki, and Katsumi Midorikawa. Fourier-transform spectroscopy combined with a 5-fs broadband pulse for multispectral nonlinear microscopy. *Physical Review A*, 77:063832, 2008.

[71] Hiroshi Hashimoto, Keisuke Isobe, Akira Suda, Fumihiko Kannari, Hiroyuki Kawano, Hideaki Mizuno, Atsushi Miyawaki, and Katsumi Midorikawa. Measurement of two-photon excitation spectra of fluorescent proteins with nonlinear Fourier-transform spectroscopy. *Applied Optics*, 49(17):3323–3329, 2010.

[72] Keisuke Isobe, Akira Suda, Masahiro Tanaka, Hiroshi Hashimoto, Fumihiko Kannari, Hiroyuki Kawano, Hideaki Mizuno, Atsushi Miyawaki, and Katsumi Midorikawa. Nonlinear optical microscopy and spectroscopy employing octave spanning pulses. *IEEE Journal of Selected Topics in Quantum Electronics*, 16(4):767–780, 2010.

[73] Fabrizio Preda, Aurelio Oriana, Julien Réhault, Lucia Lombardi, Andrea C. Ferrari, Giulio Cerullo, and Dario Polli. Linear and nonlinear spectroscopy by a common-path birefringent interferometer. *IEEE Journal of Selected Topics in Quantum Electronics*, 23(3):88–96, 2017.

[74] Aurelio Oriana, Julien Réhault, Fabrizio Preda, Dario Polli, and Giulio Cerullo. Scanning Fourier transform spectrometer in the visible range based on birefringent wedges. *Journal of the Optical Society of America A*, 33(7):1415–1420, 2016.

[75] Julien Réhault, Margherita Maiuri, Aurelio Oriana, and Giulio Cerullo. Two-dimensional electronic spectroscopy with birefringent wedges. *Review of Scientific Instruments*, 85(12):123107, 2014.

[76] Rocio Borrego-Varillas, Aurelio Oriana, Lucia Ganzer, Anton Trifonov, Ivan Buchvarov, Cristian Manzoni, and Giulio Cerullo. Two-dimensional electronic spectroscopy in the ultraviolet by a birefringent delay line. *Optics Express*, 24(25):28491–28499, 2016.

[77] Katherine A. Walowicz, Igor Pastirk, Vadim V. Lozovoy, and Marcos Dantus. Multiphoton intrapulse interference. 1. control of multiphoton processes in condensed phases. *The Journal of Physical Chemistry A*, 106(41):9369–9373, 2002.

[78] Mathias Hedegaard Kristensen, Peter Kjær Kristensen, Kjeld Pedersen, and Esben Skovsen. Fourier transform second harmonic generation for high-resolution nonlinear spectroscopy. *Optics Communications*, 482:126593, 2021.

[79] Jinendra K. Ranka, Alexander L. Gaeta, Andrius Baltuska, Maxim S. Pshenichnikov, and Douwe A. Wiersma. Autocorrelation measurement of 6-fs pulses based on the two-photon-induced photocurrent in a GaAsP photodiode. *Optics Letters*, 22(17):1344–1346, 1997.

[80] T. Brixner, N. H. Damrauer, B. Kiefer, and G. Gerber. Liquid-phase adaptive femtosecond quantum control: Removing intrinsic intensity dependencies. *The Journal of Chemical Physics*, 118(8):3692–3701, 2003.

[81] Christian Schriever, Stefan Lochbrunner, Patrizia Krok, and Eberhard Riedle. Tunable pulses from below 300 to 970 nm with durations down to 14 fs based on a 2 MHz ytterbium-doped fiber system. *Optics Letters*, 33(2):192–194, 2008.

[82] Maximilian Bradler and Eberhard Riedle. Sub-20 fs μJ-energy pulses tunable down to the near-UV from a 1 MHz Yb-fiber laser system. *Optics Letters*, 39(9):2588–2591, 2014.

[83] M. Bradler, P. Baum, and E. Riedle. Femtosecond continuum generation in bulk laser host materials with sub-μJ pump pulses. *Applied Physics B*, 97(3):561–574, 2009.

[84] Daniele Brida, Cristian Manzoni, and Giulio Cerullo. Phase-locked pulses for two-dimensional spectroscopy by a birefringent delay line. *Optics Letters*, 37(15):3027–3029, 2012.

[85] Antonio Perri, Fabrizio Preda, Cosimo D'Andrea, Erling Thyrhaug, Giulio Cerullo, Dario Polli, and Jürgen Hauer. Excitation–emission Fourier-transform spectroscopy based on a birefringent interferometer. *Optics Express*, 25(12):A483–A490, 2017.

[86] Lukas Wolz, Constantin Heshmatpour, Antonio Perri, Dario Polli, Giulio Cerullo, Jonathan J. Finley, Erling Thyrhaug, Jürgen Hauer, and Andreas V. Stier. Time-domain photocurrent spectroscopy based on a common-path birefringent interferometer. *Review of Scientific Instruments*, 91(12):123101, 2020.

[87] Y. R. Shen. *The Principles of Nonlinear Optics*. Wiley, 1984.

[88] Sung-Jae Chung, Mariacristina Rumi, Valérie Alain, Stephen Barlow, Joseph W. Perry, and Seth R. Marder. Strong, low-energy two-photon absorption in extended amine-terminated cyano-substituted phenylenevinylene oligomers. *Journal of the American Chemical Society*, 127(31):10844–10845, 2005.

[89] Mariacristina Rumi, Jeffrey E. Ehrlich, Ahmed A. Heikal, Joseph W. Perry, Stephen Barlow, Zhongying Hu, Dianne McCord-Maughon, Timothy C. Parker, Harald Röckel, Sankaran Thayumanavan, Seth R. Marder, David Beljonne, and Jean-Luc Brédas. Structure-property relationships for two-photon absorbing chromophores: bis-donor diphenylpolyene and bis(styryl)benzene derivatives. *Journal of the American Chemical Society*, 122(39):9500–9510, 2000.

[90] Jeffrey B. Guild, Chris Xu, and Watt W. Webb. Measurement of group delay dispersion of high numerical aperture objective lenses using two-photon excited fluorescence. *Applied Optics*, 36(1):397–401, 1997.

[91] Ivan Amat-Roldán, Iain G. Cormack, Pablo Loza-Alvarez, Emilio J. Gualda, and David Artigas. Ultrashort pulse characterisation with SHG collinear-FROG. *Optics Express*, 12(6):1169–1178, 2004.

[92] Gero Stibenz and Günter Steinmeyer. Interferometric frequency-resolved optical gating. *Optics Express*, 13(7):2617–2626, 2005.

[93] Rick Trebino, Kenneth W. DeLong, David N. Fittinghoff, John N. Sweetser, Marco A. Krumbügel, Bruce A. Richman, and Daniel J. Kane. Measuring ultrashort laser pulses in the time-frequency domain using frequency-resolved optical gating. *Review of Scientific Instruments*, 68(9):3277–3295, 1997.

[94] M. Müller, J. Squier, R. Wolleschensky, U. Simon, and J. Brakenhoff. Dispersion pre-compensation of 15 femtosecond optical pulses for high-numerical-aperture objectives. *Journal of Microscopy*, 191(2):141–150, 1998.

[95] J. Jasapara and W. Rudolph. Characterization of sub-10-fs pulse focusing with high-numerical-aperture microscope objectives. *Optics Letters*, 24(11):777–779, 1999.

[96] Adam M. Larson and Alvin T. Yeh. *Ex vivo* characterization of sub-10-fs pulses. *Optics Letters*, 31(11):1681–1683, 2006.

[97] Jean-Claude Diels and Wolfgang Rudolph. *Ultrashort Laser Pulse Phenomena*. Elsevier, 2006.

[98] Takanori Wakebe and Edward Van Keuren. The excitation spectra of two-photon induced fluorescence in xanthene dyes. *Japanese Journal of Applied Physics*, 38(Part 1, No. 6A):3556–3561, 1999.

[99] Leonas Valkunas, Darius Abramavicius, and Tomás Mancal. Quantum states of molecules and aggregates. In *Molecular Excitation Dynamics and Relaxation: Quantum Theory and Spectroscopy*, chapter 5, pages 101–132. Wiley, 2013.

[100] M. D. Allendorf, C. A. Bauer, R. K. Bhakta, and R. J. T. Houk. Luminescent metal–organic frameworks. *Chemical Society Reviews*, 38:1330–1352, 2009.

[101] Sheridan Few, Jarvist M. Frost, James Kirkpatrick, and Jenny Nelson. Influence of chemical structure on the charge transfer state spectrum of a polymer: Fullerene complex. *The Journal of Physical Chemistry C*, 118(16):8253–8261, 2014.

[102] B. N. Jagatap and William J. Meath. Contributions of permanent dipole moments to molecular multiphoton excitation cross sections. *Journal of the Optical Society of America B*, 19(11):2673–2681, 2002.

[103] Naifang Liu, Zhihui Chen, Wenxuan Fan, Jie Su, Tingting Lin, Si Xiao, Jianqiao Meng, Jun He, Jagadese J. Vittal, and Jianzhuang Jiang. Highly efficient multiphoton absorption of zinc-aiegen metal–organic frameworks. *Angewandte Chemie International Edition*, 61(12):e202115205, 2022.

[104] Farnoosh ZareKarizi, Monika Joharian, and Ali Morsali. Pillar-layered MOFs: functionality, interpenetration, flexibility and applications. *J. Mater. Chem. A*, 6:19288–19329, 2018.

[105] Hong Sheng Quah, Venkatram Nalla, Kezhi Zheng, Chloe Aloycia Lee, Xiaogang Liu, and Jagadese J. Vittal. Tuning two-photon absorption cross section in metal organic frameworks. *Chemistry of Materials*, 29(17):7424–7430, 2017.

[106] David C. Mayer, Jan K. Zareba, Gabriele Raudaschl-Sieber, Alexander Pöthig, Marta Chołuj, Robert Zaleśny, Marek Samoć, and Roland A. Fischer. Postsynthetic framework contraction enhances the two-photon absorption properties of pillar-layered metal–organic frameworks. *Chemistry of Materials*, 32(13):5682–5690, 2020.

[107] Bibhuti Bhusan Rath, Dileep Kottilil, Wei Ji, and Jagadese J. Vittal. Enhancement in two-photon absorption and photoluminescence in single crystals of Cd(II) metal–organic frameworks. *ACS Applied Materials & Interfaces*, 15(22):26939–26945, 2023.

[108] Zhaoyang Yao, Lin Yang, Yanchun Cai, Cancan Yan, Min Zhang, Ning Cai, Xiandui Dong, and Peng Wang. Rigidifying the π-linker to enhance light absorption of organic dye-sensitized solar cells and influences on charge transfer dynamics. *The Journal of Physical Chemistry C*, 118(6):2977–2986, 2014.

[109] Hui Huang, Lei Yang, Antonio Facchetti, and Tobin J. Marks. Organic and polymeric semiconductors enhanced by noncovalent conformational locks. *Chemical Reviews*, 117(15):10291–10318, 2017.

[110] Brian D. McCarthy, Eric R. Hontz, Shane R. Yost, Troy Van Voorhis, and Mircea Dincă. Charge transfer or J-coupling? assignment of an unexpected red-shifted absorption band in a naphthalenediimide-based metal–organic framework. *The Journal of Physical Chemistry Letters*, 4(3):453–458, 2013.

[111] Long Yang, Yuyan Yu, Jie Feng, Juying Wu, Long Jiang, Yi Dan, and Yong Qiu. Charge transfer induced unexpected red-shift absorption of Zn and Cu porous coordination polymers based on electron-withdrawing ligand. *Journal of Photochemistry and Photobiology A: Chemistry*, 350:103–110, 2018.

[112] Tamara A. Vaganova, Yurij V. Gatilov, Enrico Benassi, Igor P. Chuikov, Denis P. Pishchur, and Evgenij V. Malykhin. Impact of molecular packing rearrangement on solid-state fluorescence: polyhalogenated n-hetarylamines vs. their co-crystals with 18-crown-6. *CrystEngComm*, 21:5931–5946, 2019.

[113] Yuxuan Che and Dmitrii F. Perepichka. Quantifying planarity in the design of organic electronic materials. *Angewandte Chemie International Edition*, 60(3):1364–1373, 2021.

[114] Christina A. Bauer, Tatiana V. Timofeeva, Thomas B. Settersten, Brian D. Patterson, Vincent H. Liu, Blake A. Simmons, and Mark D. Allendorf. Influence of connectivity and porosity on ligand-based luminescence in zinc metal–organic frameworks. *Journal of the American Chemical Society*, 129(22):7136–7144, 2007.

[115] Małgorzata Wielgus, Joanna Michalska, Marek Samoc, and Wojciech Bartkowiak. Two-photon solvatochromism III: Experimental study of the solvent effects on two-photon absorption spectrum of *p*-nitroaniline. *Dyes and Pigments*, 113:426–434, 2015.

[116] Simona Sorbara, Soumya Mukherjee, Andreas Schneemann, Roland A. Fischer, and Piero Macchi. Hydrophobicity and dielectric properties across an isostructural family of MOFs: a duet or a duel? *Chemical Communications*, 58:12823–12826, 2022.

[117] Hong Sheng Quah, Weiqiang Chen, Martin K. Schreyer, Hui Yang, Ming Wah Wong, Wei Ji, and Jagadese J. Vittal. Multiphoton harvesting metal–organic frameworks. *Nature Communications*, 6(1):7954, 2015.

[118] Simon N. Deger, Yang Cui, Julien Warnan, Roland A. Fischer, František Šanda, Jürgen Hauer, and Alexander Pöthig. Influence of chromophore packing on multiphoton absorption in carbazole-based pillar-layered coordination polymers. *ACS Applied Optical Materials*, xx(xx):xxxx–xxxx, 2024.

[119] Jianmin Yang, Maxim F. Gelin, Lipeng Chen, František Šanda, Erling Thyrhaug, and Jürgen Hauer. Two-dimensional fluorescence excitation spectroscopy: A novel technique for monitoring excited-state photophysics of molecular species with high time and frequency resolution. *The Journal of Chemical Physics*, 159(7):074201, 2023.

[120] Aswin Alexander, Mayank Gupta, Dileep Kottilil, Bibhuti Bhusan Rath, Jagadese J. Vittal, and Wei Ji. Anisotropic two-photon absorption and second harmonic generation in single crystals of silver(I) coordination complexes. *ACS Applied Materials & Interfaces*, 13(27):31891–31897, 2021.

[121] Lijuan Zhao, J. Luis Pérez Lustres, Vadim Farztdinov, and Nikolaus P. Ernsting. Femtosecond fluorescence spectroscopy by upconversion with tilted gate pulses. *Physical Chemistry Chemical Physics*, 7:1716–1725, 2005.

[122] David M. Jonas. Two-dimensional femtosecond spectroscopy. *Annual Review of Physical Chemistry*, 54:425–463, 2003.

[123] J. Shah. Ultrafast luminescence spectroscopy using sum frequency generation. *IEEE Journal of Quantum Electronics*, 24(2):276–288, 1988.

[124] Mario Gerecke, Genaro Bierhance, Michael Gutmann, Nikolaus P. Ernsting, and Arnulf Rosspeintner. Femtosecond broadband fluorescence upconversion spectroscopy: Spectral coverage versus efficiency. *Review of Scientific Instruments*, 87(5):053115, 2016.

[125] Ismael A. Heisler and Stephen R. Meech. Altered relaxation dynamics of excited state reactions by confinement in reverse micelles probed by ultrafast fluorescence up-conversion. *Chemical Society Reviews*, 50:11486–11502, 2021.

[126] Bas Gobets, John T. M. Kennis, Janne A. Ihalainen, Michela Brazzoli, Roberta Croce, Ivo H. M. van Stokkum, Roberto Bassi, Jan P. Dekker, Herbert van Amerongen, Graham R. Fleming, and Rienk van Grondelle. Excitation energy transfer in dimeric light harvesting complex I: A combined streak-camera/fluorescence upconversion study. *The Journal of Physical Chemistry B*, 105(41):10132–10139, 2001.

[127] J. Takeda, K. Nakajima, S. Kurita, S. Tomimoto, S. Saito, and T. Suemoto. Time-resolved luminescence spectroscopy by the optical Kerr-gate method applicable to ultrafast relaxation processes. *Physical Review B*, 62:10083–10087, 2000.

[128] Chul Hoon Kim and Taiha Joo. Ultrafast time-resolved fluorescence by two photon absorption excitation. *Optics Express*, 16(25):20742–20747, 2008.

[129] C. Radzewicz, Y.B. Band, G.W. Pearson, and J.S. Krasinski. Short pulse nonlinear frequency conversion without group-velocity-mismatch broadening. *Optics Communications*, 117(3):295–302, 1995.

[130] Jing-Yuan Zhang, Aparna Prasad Shreenath, Mark Kimmel, Erik Zeek, Rick Trebino, and Stephan Link. Measurement of the intensity and phase of attojoule femtosecond light pulses using optical-parametric-amplification cross-correlation frequency-resolved optical gating. *Optics Express*, 11(6):601–609, 2003.

[131] Hailong Chen, Yuxiang Weng, and Jingyuan Zhang. Noncollinear optical parametric amplifier based femtosecond time-resolved transient fluorescence spectra: characterization and correction. *Journal of the Optical Society of America B*, 26(8):1627–1634, 2009.

[132] Piotr Fita, Yuriy Stepanenko, and Czeslaw Radzewicz. Femtosecond transient fluorescence spectrometer based on parametric amplification. *Applied Physics Letters*, 86(2):021909, 2005.

[133] Xiao-Feng Han, Xing-Hai Chen, Yu-Xiang Weng, and Jing-Yuan Zhang. Ultrasensitive femtosecond time-resolved fluorescence spectroscopy for relaxation processes by using parametric amplification. *Journal of the Optical Society of America B*, 24(7):1633–1638, 2007.

[134] James Lim, David Paleček, Felipe Caycedo-Soler, Craig N. Lincoln, Javier Prior, Hans von Berlepsch, Susana F. Huelga, Martin B. Plenio, Donatas Zigmantas, and Jürgen Hauer. Vibronic origin of long-lived coherence in an artificial molecular light harvester. *Nature Communications*, 6(1):7755, 2015.

[135] Alessandra Picchiotti, Valentyn I. Prokhorenko, and R. J. Dwayne Miller. A closed-loop pump-driven wire-guided flow jet for ultrafast spectroscopy of liquid samples. *Review of Scientific Instruments*, 86(9):093105, 2015.

Appendix

A. Full-length article of Section 2.1

CHEMISTRY OF MATERIALS

pubs.acs.org/cm

Article

Coordination Polymers Based on Carbazole-Derived Chromophore Linkers for Optimized Multiphoton Absorption: A Structural and Photophysical Study

Sebastian J. Weishäupl,[⊥] Yang Cui,[⊥] Simon N. Deger, Hamad Syed, Aleksandr Ovsianikov, Jürgen Hauer,* Alexander Pöthig,* and Roland A. Fischer*

Cite This: *Chem. Mater.* 2022, 34, 7402−7411

Read Online

ACCESS | Metrics & More | Article Recommendations | Supporting Information

ABSTRACT: Multiphoton absorption (MPA), as a subgroup of non-linear optical effects, is of high interest in modern materials research since it has a great applicability in optoelectronics. However, most of the commonly used materials featuring MPA properties are chromophore molecules, which are limited by their thermal stability and uncontrolled aggregation in high-concentration solutions. A prominent material class which could in principle overcome these problems are metal−organic frameworks and coordination polymers (CPs) as they can be modularly tuned to possess chemical and thermal stability. In addition, by incorporating chromophores as linkers in the framework, their molecular properties can be retained or even enhanced. In this article, we report the synthesis and characterization of three new and highly MPA-active CPs, $Zn_2(sbcd)(DMAc)_2(H_2O)_{1.5}$, $Sr(fbcd)(DMAc)_{0.25}(H_2O)_{3.5}$, and $Ba(fbcd)(DMAc)_{2.5}(H_2O)_{1.5}$, based on two carbazole-containing chromophore linkers: a previously reported 9,9′-stilbene-bis-carbazole-3,6-dicarboxylic acid (H_4sbcd) and the new 2,7-fluorene-9,9′-dimethyl-bis-carbazole-3,6-dicarboxylic acid (H_4fbcd). Single-crystal structure analysis of the zinc-based CP reveals a *sql* network, whereas the barium- and strontium-based CPs are isostructural, showing a 4,8-c network topology. Z-scan analysis of the networks shows large two-photon absorption cross-sections $\sigma^{(2)}$ of 2100 to 33,300 GM, which is an enhancement of up to 3 orders of magnitude in comparison to the solvated linker and is also one of the highest MPA-cross-sections reported for CPs up to date.

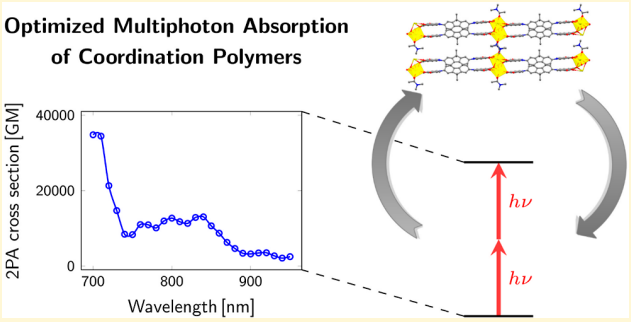

INTRODUCTION

Non-linear optics (NLO) is the study of light-induced phenomena with above-linear scaling with respect to the incident light intensity.[1] NLO-related effects such as second-harmonic generation or multiphoton absorption (MPA) have a wide range of applications ranging from 3D-data storage and optical limiting to bio-imaging.[2] In this respect, coordination polymers (CPs) or metal−organic frameworks (MOFs) featuring chromophore linkers are a promising material class as they are known to be chemically versatile and stable even under intense light conditions.[3−5]

CPs or MOFs are a hybrid material class comprising inorganic metal nodes—often built from metal-oxo-clusters—bridged by organic linkers often having dicarboxylic acids or pyridyls as donor groups.[6] The versatility in the choice of linker and metal nodes explains the enormous variability of these materials. Molecular linker properties, for example, regarding photo- or electrocatalytic activity, can be transferred directly into a solid framework, preserving the properties of the monomer unit. Furthermore, interactions of the molecules within the framework allow for additional and directed modifications of the linker properties.[7]

Accordingly, MPA-active molecules inside an MOF can show an enhanced MPA cross-section as compared to the uncoordinated molecule.[8−11] This enhancement can be explained by structural rigidity and multi-chromophore effects such as excitonic coupling, all of which are due to the special steric arrangements of the linkers in the MOF. The relative orientation of the linkers can also be engineered using different metals or different additives in order to synthesize a variety of topologies to directly influence the optical properties of the MOF.[12−14] Additionally, an appropriate choice of metal centers may open charge transfer channels such as ligand-to-metal charge transfer or metal-to-ligand charge transfer.[15] Such extra decay channels may heavily influence the photophysical properties of the solid-state material.

Received: May 20, 2022
Revised: July 19, 2022
Published: August 8, 2022

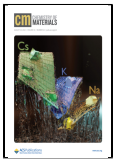

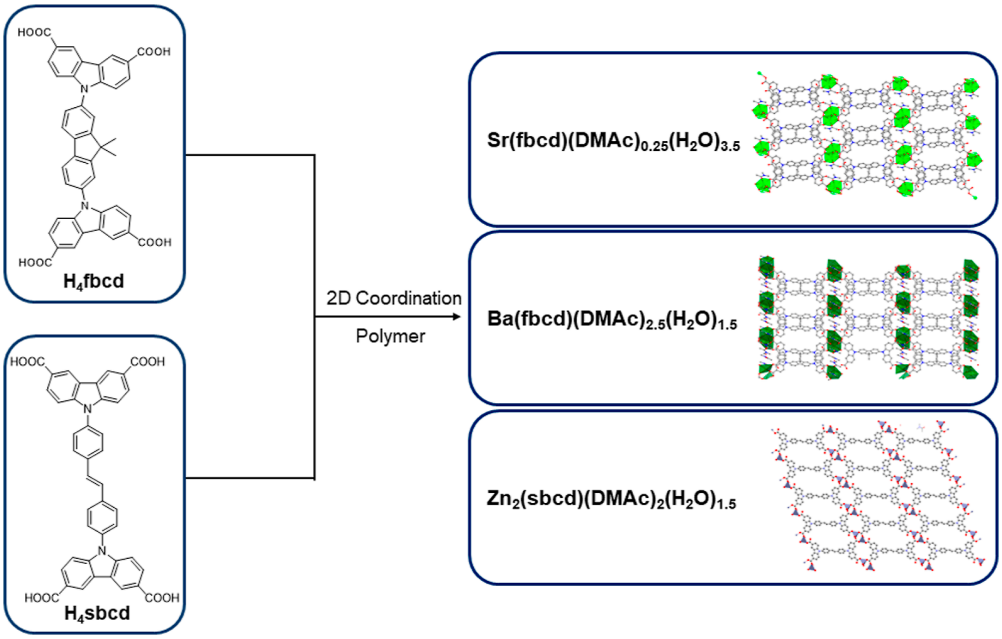

Figure 1. Overview of the synthesized and characterized materials in this work.

The properties of the linker molecule are another decisive factor when synthesizing MPA-active MOFs or CPs. For example, a strong intramolecular charge-transfer character is known to be beneficial for a large MPA cross-section.[16,17] Hence, chromophores bearing electron-pushing groups (electron donor), electron-pulling groups (electron acceptor), or both connected with large aromatic systems are molecular designs sought after when aiming for an MPA-active linker.[18,19] In this context, carbazoles show desirable properties as they act as electron donors.[20,21] From the point of view of optoelectronic research, carbazoles are well established systems due to their chemical stability, robustness, and generally desirable electronic properties.

In this article, we report the synthesis and photophysical characterization of two carbazole-based MPA-active chromophore linkers, namely, the new 2,7-fluorene-9,9′-dimethyl-bis-carbazole-3,6-dicarboxylic acid (H_4fbcd) and 9,9′-stilbene-bis-carbazole-3,6-dicarboxylic acid (H_4sbcd), which were recently reported first by Krause et al. for gas sorption studies incorporated in a copper MOF in 2020.[22] Furthermore, three different CPs were successfully synthesized employing a solvothermal synthesis strategy, resulting in single-crystalline materials of $Zn_2(sbcd)(DMAc)_2(H_2O)_{1.5}$, $Sr(fbcd)(DMAc)_{0.25}(H_2O)_{3.5}$, and $Ba(fbcd)(DMAc)_{2.5}(H_2O)_{1.5}$ with the above-mentioned linkers incorporated (Figure 1). Their corresponding crystal structures were determined, revealing that all materials are 2D CPs: the zinc-based stilbene CP crystallizes in the *sql* topology, whereas the fluorene-based main-group metal CPs crystallize in a 4,8-c net topology with two linker molecules anti-parallel arranged to each other. Z-scan measurements of the synthesized materials were performed with a fully automated setup based on a tunable femtosecond oscillator to obtain excitation-wavelength-dependent two-photon excitation spectra.[23] The results on the CP materials showed large two-photon absorption cross-sections $\sigma^{(2)}$ in the range of 2100−33,300 GM, which is an enhancement of up to 3 orders of magnitude as compared to the free linker in solution. Hence, MOFs or CPs with specifically designed linker molecules represent ideal candidates for MPA-active materials.

EXPERIMENTAL SECTION

Material and Methods. All purchased reagents were received from chemical suppliers and used without any further purification if not otherwise stated. Dipropyl-9-(4-nitrophenyl)-carbazole-3,6-dicarboxylate was synthesized following the previous published synthesis procedure.[20] All reactions with air- and moisture-sensitive compounds were carried out under standard Schlenk techniques using Argon 4.6 (Westfalen) or in a glovebox (*UNIlab*, M. Braun). Required glassware was flame-dried in vacuo prior to use. Elemental analysis was performed at the micro analytic laboratory at the Technical University of Munich. Analysis of C, H, and N values was conducted by the flash combustion method at 1800 °C. NMR spectra were recorded on a Bruker AV400 at room temperature at 400 MHz. LIFDI-MS data were recorded on an *Exactive Plus* Orbitrap system by Thermo Fisher Scientific equipped with an ion source (LIFDI) from LINDEN CMS GmbH.[24] Single-crystal X-ray diffraction (SC-XRD) data were collected on a BRUKER *D8 Venture* system equipped with a Mo TXS rotating anode (λ = 0.71073 Å) and a CMOS photon 100 detector (for detailed information, see the Supporting Information). Capillary PXRD measurements were recorded in transmission geometry on a Stoe *STADI P* diffractometer equipped with Mo radiation (λ = 0.7093 Å), a curved Ge(111) monochromator, and a Dectris Mythen 1K detector. UV/Vis spectra in solution were recorded on a double-beam *Lambda 365* UV−Vis spectrophotometer from PerkinElmer. Diffuse reflectance UV/vis measurements of sample powder were performed on a Shimadzu *UV-3600 Plus* UV−Vis−NIR spectrophotometer by fixing it between two quartz glass slides. Fluorescence measurements were recorded on an *FS5* spectrofluorometer from Edinburgh Instruments either in solution (linker) or in a PMMA matrix (CPs). IR measurements were conducted on a PerkinElmer *Frontier* FT-IR spectrometer. Excitation-wavelength-dependent Z-scans were performed using a femtosecond oscillator as part of an experimental setup designed previously.[23]

Synthesis. *4,4′-Dibromostilbene 2.* To a suspension of zinc powder (6.00 g, 90.69 mmol, 5.60 equiv) in THF (150 mL) at 0 °C, slowly, $TiCl_4$ (5 mL, 8.61 g, 45.34 mmol, 2.80 equiv) is added via a syringe. Subsequently, the reaction mixture is heated to 80 °C, and bromobenzaldehyde (3.00 g, 16.2 mmol, 1.00 equiv) and THF (50 mL) is added and heated for 5 h at reflux. After completion, saturated

https://doi.org/10.1021/acs.chemmater.2c01525
Chem. Mater. 2022, 34, 7402−7411

$NaHCO_3$ solution is added dropwise at room temperature. Afterward, the organic layer is separated and the water is extracted with chloroform (3 × 100 mL). The combined organic layers are dried with magnesium sulfate, filtered, and then concentrated on a rotary evaporator to yield a white solid (2.56 g, 93%). ^{1}H NMR (400 MHz, $CDCl_3$): δ (ppm) 7.02 (s, 2H), 7.36 (d, J = 8.47 Hz, 4H), 7.48 (d, J = 8.45 Hz, 4H).

4,4′-Diiodostilbene **3**. 2.5 M nBuLi solution (5.45 mL, 13.6 mmol, 4.60 equiv) was slowly dropped into a mixture of *trans*-4,4′-dibromostilbene (6) (1.00 g, 2.96 mmol, 1.00 equiv) in THF (150 mL) at −78 °C. Then the yellow solution was stirred at −78 °C for 4 h. Afterward, it was warmed up to 0 °C, whereby the color of the solution was changed from yellow to grayish yellow. The reaction mixture was cooled down again to −78 °C, and a solution of iodine (2.82 g, 11.1 mmol, 3.75 equiv) in THF (48 mL) was added. Finally, the reddish-brown solution was quenched with a solution of sodium thiosulfate (2 spatulas $Na_2S_2O_3$ in 150 mL H_2O) and filtrated through a glass filter. The filter cake was then washed multi-times with water and dried at 100 °C to get a yellowish solid (1.07 g, 100%). ^{1}H NMR (400 MHz, $CDCl_3$): δ (ppm) 7.04 (d, 4H), 7.26 (d, J = 14.2 Hz), 7.70 (dd, J = 8.3, 1.9 Hz, 4H).

Dipropyl-9,9′-(stilbyl)-bis-(carbazole-3,6-dicarboxylate) **4** *(Pr_4sbcd)*. Dipropyl-carbazole-3,6-dicarboxylate (0.785 g, 2.32 mmol, 2 equiv), 4,4′-iodostilbene (0.5 g, 1.16 mmol, 1 equiv), K_3PO_4 (1.97 g, 9.26 mmol, 8 equiv), DMEDA (0.186 mL, 1.74 mmol, 1.5 equiv), and CuI (66 mg, 0.34 mmol, 0.3 equiv) were dissolved in 15 mL of dry toluene in a 50 mL Schlenk flask and heated to 115 °C for 3 days. After cooling, the suspension was dissolved in 60 mL of aq. NH_4Cl solution, extracted with chloroform (3 × 50 mL). The organic phases were combined and then dried with $MgSO_4$. The solvent was evaporated on a rotary evaporator to give a brown solid. The crude product was then dissolved in 5 mL of dichloromethane (DCM) and added dropwise to 35 mL of MeCN in a centrifuge tube. The precipitate was collected by centrifugation and washed with MeCN twice to give pale-yellow powder. Subsequently, the raw product is then subjected to column chromatography (DCM 100%) to give an off-white powder (810 mg, 0.94 mmol, 82%). ^{1}H NMR (400 MHz, $CDCl_3$): δ (ppm) 1.12 (t, J = 7.4 Hz, 12H, CH_3), 1.89 (h, J = 7.2 Hz, 8H), 4.38 (t, J = 6.7 Hz, 8H), 7.26 (d, 4H), 7.49 (d, J = 8.5 Hz, 4H), 7.69 (d, J = 14.2 Hz, 2H), 7.86 (dd, J = 8.3, 1.9 Hz, 4H), 8.23 (dd, J = 1.5 Hz, 4H), 8.89 (s, 4H). ^{13}C NMR (101 MHz, 298 K, $CDCl_3$) δ (ppm) 10.76, 22.43, 66.72, 109.94, 123.18, 123.41, 123.48, 127.52, 128.40, 128.42, 129.05, 136.14, 137.35, 144.27, 167.20. LIFDI-MS: m/z $[M]^+$ calcd for $C_{54}H_{50}N_2O_8$, 854.3562; found, 854.3545. EA calcd for $C_{54}H_{50}N_2O_8$: C, 75.86; H, 5.89; N, 3.28; found: C, 74.76; H, 5.87; N, 3.45.

9,9′-(Stilbyl)-bis-(carbazole-3,6-dicarboxylic acid) **5** *(H_4sbcd)*. To a solution of Pr_4sbcd (450 mg, 0.59 mmol, 1.00 equiv) in 150 mL of THF and 15 mL of MeOH, an aqueous NaOH solution (2.5 g in 250 mL of water) is added and heated for 18 h at 90 °C. After completion of the reaction, THF and MeOH are removed under vacuum on a rotary evaporator. Subsequently, the aqueous phase is acidified with a 2 N HCl solution till it reacts acidic. The resulting white precipitate is filtered, washed with water, and then dried, giving a white powder (335 mg, 0.48 mmol, 85%). ^{1}H NMR (400 MHz, 298 K, DMSO-d_6) δ (ppm) 7.52 (d, 4H), 7.61 (s, 2H) 7.74 (d, 4H), 8.02 (d, 4H), 8.12 (dd, 4H), 8.99 (s, 4H), 12.81 (s, 4H); ^{13}C NMR (101 MHz, 298 K, DMSO-d_6) δ (ppm) 110.03, 122.56, 123.03, 123.05, 123.45, 127.26, 128.32, 128.43, 128.79, 137.18, 143.44, 167.63; LIFDI-MS: m/z $[M]^+$ calcd for $C_{42}H_{26}N_2O_8$, 686.1684; found, 686.1667. EA calcd for $C_{42}H_{26}N_2O_8$: C, 73.46; H, 3.82; N, 4.08. Found: C, 70.87; H, 4.2; N, 4.02.

2,7-Diiodofluorene **6**. A Schlenk flask is filled with 5.00 g (30.05 mmol, 1.00 equiv) of fluorene, 40.70 mL of acetic acid, 8.15 mL of water, and 1.22 mL of conc. H_2SO_4 and heated up to 80 °C to dissolve fluorene completely. Subsequently, the mixture is cooled down to 60 °C, treated with 5.10 g (20.08 mmol, 0.67 equiv) of I_2 and 2.30 g (10.09 mmol, 0.34 equiv) of H_5IO_6, and stirred for 4 h. The violet-red solution is filtered and recrystallized with 100 mL *n*-hexane. The precipitation is dried to a fine orange-yellow powder. ^{1}H NMR (400 MHz, $CDCl_3$): δ (ppm) 7.87 (d, J = 1.5 Hz, 2H), 7.70 (dd, J = 8.0, 1.6 Hz, 2H), 7.49 (d, J = 8.0 Hz, 2H), 3.83 (s, 2H).

2,7-Diiodo-9,9-dimethyl fluorene **7**. In a Schlenk flask, 4.17 g (9.97 mmol, 1.00 equiv) of 2,7-diiodofluorene is dissolved in 30 mL of dry THF and cooled down to 0 °C. Afterward, 2.56 g (26.64 mmol, 2.67 equiv) of Na^{t}OBu is added to the mixture and stirred at room temperature for 2 h. At 0 °C, the mixture is treated with 1.86 mL (29.88 mmol, 3.00 equiv) of MeI and stirred overnight at room temperature. Subsequently, the dark-yellow solution is filtered with Celite and evaporated to a bright orange-yellow powder. The crude product is recrystallized with 30 mL of toluene to give an orange-brown powder. ^{1}H NMR (400 MHz, $CDCl_3$): δ (ppm) 7.74 (d, J = 1.6 Hz, 2H), 7.66 (dd, J = 8.0, 1.6 Hz, 2H), 7.43 (d, J = 8.0 Hz, 2H), 1.45 (s, 6H).

Dipropyl-2,7-flourene-9,9-dimethyl-bis-carbazole-3,6-dicarboxylate **8** *(Pr_4fbcd)*. 9,9-Dimethyl-2,7-diiodofluorene (500 mg, 1.12 mmol, 1.00 equiv), carbazole-3,6-dipropyl-ester (761 mg, 2.24 mmol, 2.00 equiv), CuI (64.04 mg, 0,336 mmol, 0.3 equiv), DMEDA (0.18 mL, 1.68 mmol,1.5 equiv), and K_3PO_4 (1.90 g, 8.97 mmol, 8.00 equiv) are dissolved in 15 mL of dry toluene to give a yellow suspension, which is heated to 115 °C for 2 days under an argon atmosphere. The resulting brown solution is extracted with chloroform (3 × 50 mL) and NH_4Cl solution, the organic phases are combined and dried with $MgSO_4$, and the solvent is subsequently removed under vacuum. The resulting brown solid is redissolved in a small amount of DCM and is then poured dropwise into 35 mL of acetonitrile. The white precipitate is then centrifuged and washed three times with acetonitrile. The remaining off-white solid is then subjected to column chromatography (DCM 100%) to give a white powder (732 mg, 0.84 mmol, 75%). ^{1}H NMR (400 MHz, $CDCl_3$): δ (ppm) 1.11 (t, J = 7.5 Hz, 12H), 1.66 (s, 6H), 1.89 (h, J = 7.2 Hz, 8H), 4.38 (t, J = 6.7 Hz, 8H), 7.48 (d, J = 8.7 Hz, 4H), 7.61 (dd, J = 8.0, 1.9 Hz, 2H), 7.68 (d, J = 1.9 Hz, 2H), 8.07 (d, J = 8.0 Hz, 2H), 8.21 (dd, J = 8.6, 1.7 Hz, 4H), 9.00−8.96 (m, 4H). ^{13}C NMR (400 MHz, $CDCl_3$): 10.76, 22.39, 27.20, 47.81, 66.68, 109.90, 121.69, 121.95, 123.17, 123.34, 123.36, 128.38, 136.10, 138.48, 144.37, 156.14, 167.16. LIFDI-MS: m/z $[M]^+$ calcd for $C_{55}H_{52}N_2O_8$, 868.3718; found, 868.3694. EA calcd for $C_{55}H_{52}N_2O_8$: C, 76.02; H, 6.03; N, 3.22. Found: C, 75.20; H, 5.92; N, 3.21.

2,7-Fluorene-9,9-dimethyl-bis-carbazole-3,6-dicarboxylic Acid **9** *(H_4fbcd)*. To a solution of Pr_4fbcd (450 mg, 0.57 mmol, 1.00 equiv) in 150 mL of THF and 15 mL of MeOH, an aqueous NaOH solution (2.5 g in 250 mL of water) is added and heated for 18 h at 90 °C. After completion of the reaction, THF and MeOH are removed under vacuum on a rotary evaporator. Subsequently, the aqueous phase is acidified with a 2 N HCl solution until it reacts acidic. The resulting white precipitate is filtered, washed with water, and then dried, giving a white powder (336 mg, 0.48 mmol, 84%). ^{1}H NMR (400 MHz, DMSO): δ (ppm) 1.63 (s, 6H), 7.52 (d, J = 8.6 Hz, 2H), 7.72 (dd, J = 8.0, 1.9 Hz, 2H), 8.01 (d, J = 1.9 Hz, 2H), 8.14 (dd, J = 8.7 Hz, 1.7 Hz, 4H), 8.30 (d, J = 8.1 Hz, 2H), 9.01 (d, J = 1.7 Hz, 4H). ^{13}C NMR (400 MHz, DMSO-d_6): δ (ppm) 27.40, 47.51, 110.04, 121.82, 122.31, 122.53, 123.04, 123.42, 126.14, 128.34, 135.25, 137.89, 143.62, 156.08, 167.63. LIFDI-MS: m/z $[M]^+$ calcd for $C_{43}H_{28}N_2O_8$, 700.1840; found, 700.1830. EA calcd for $C_{43}H_{28}N_2O_8$: C, 73.71; H, 4.03; N, 4.00. Found: C, 70.07; H, 4.25; N, 2.97.

Zn_2(sbcd)(DMAc)$_2$(H_2O)$_{1.5}$. In a 4 mL screw cap vial, 10 mg of H_4sbcd and 11.12 mg of $Zn(NO_3)_2$ (3 equiv) were dissolved in a DMAc/water mixture (2/0.5 mL) and heated at 90 °C for 2 days. The resulting precipitate was filtered, washed with DMAc, and dried to give white frost-flower shaped crystals (6.6 mg, 45%). EA calcd for $Zn_2C_{42}H_{22}N_2O_8{\cdot}2C_4H_9O{\cdot}1.5H_2O$: C, 58.67; H, 4.33; N, 5.47; Zn, 12.77. Found: C, 58.71; H, 4.52; N, 5.81; Zn, 12.3.

Sr(fbcd)(DMAc)$_{0.25}$(H_2O)$_{3.5}$. In a 4 mL screw cap vial, 10 mg of H_4fbcd and 9.24 mg of $Sr(NO_3)_2$ (3 equiv) were dissolved in a DMAc/water mixture (2/0.5 mL) and heated at 100 °C for 2 days. The resulting precipitate was filtered, washed with DMAc, and dried to give a white crystalline needle (5.2 mg, 42%). EA calcd for $SrC_{43}H_{26}N_2O_8{\cdot}0.25C_4H_9O{\cdot}3.5H_2O$: C, 60.46; H, 3.89; N, 3.6. Found: C, 60.67; H, 4.08; N, 3.62.

https://doi.org/10.1021/acs.chemmater.2c01525
Chem. Mater. 2022, 34, 7402−7411

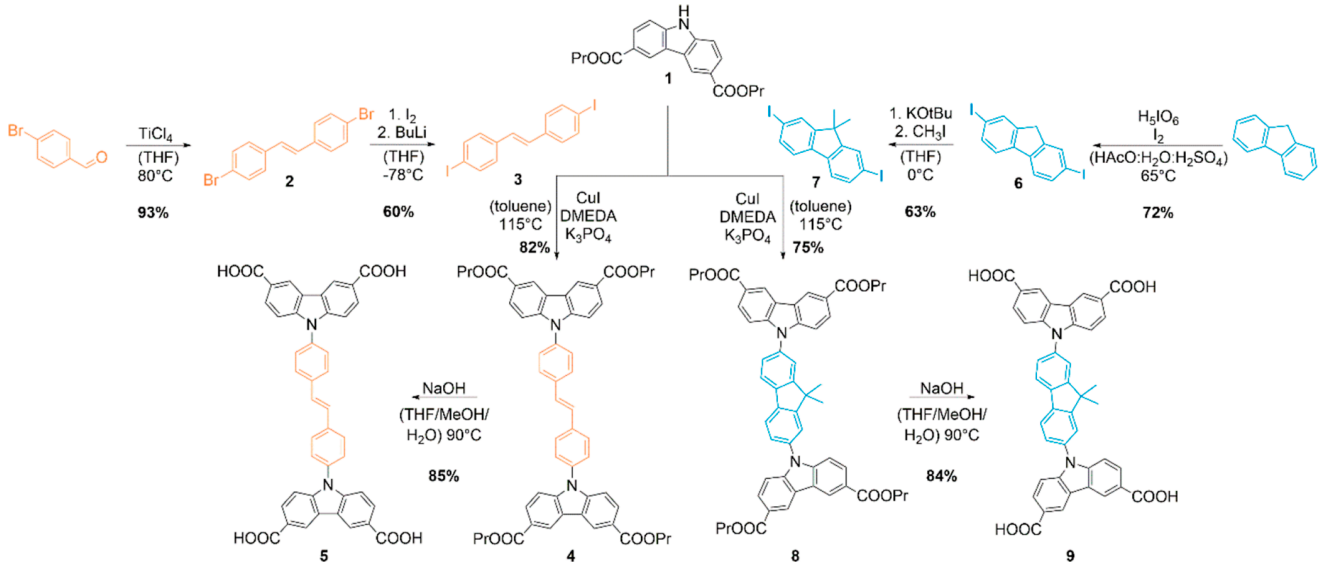

Figure 2. Multi-step synthesis procedure toward the carbazole-based linkers H_4sbcd **5** and H_4fbcd **9**.

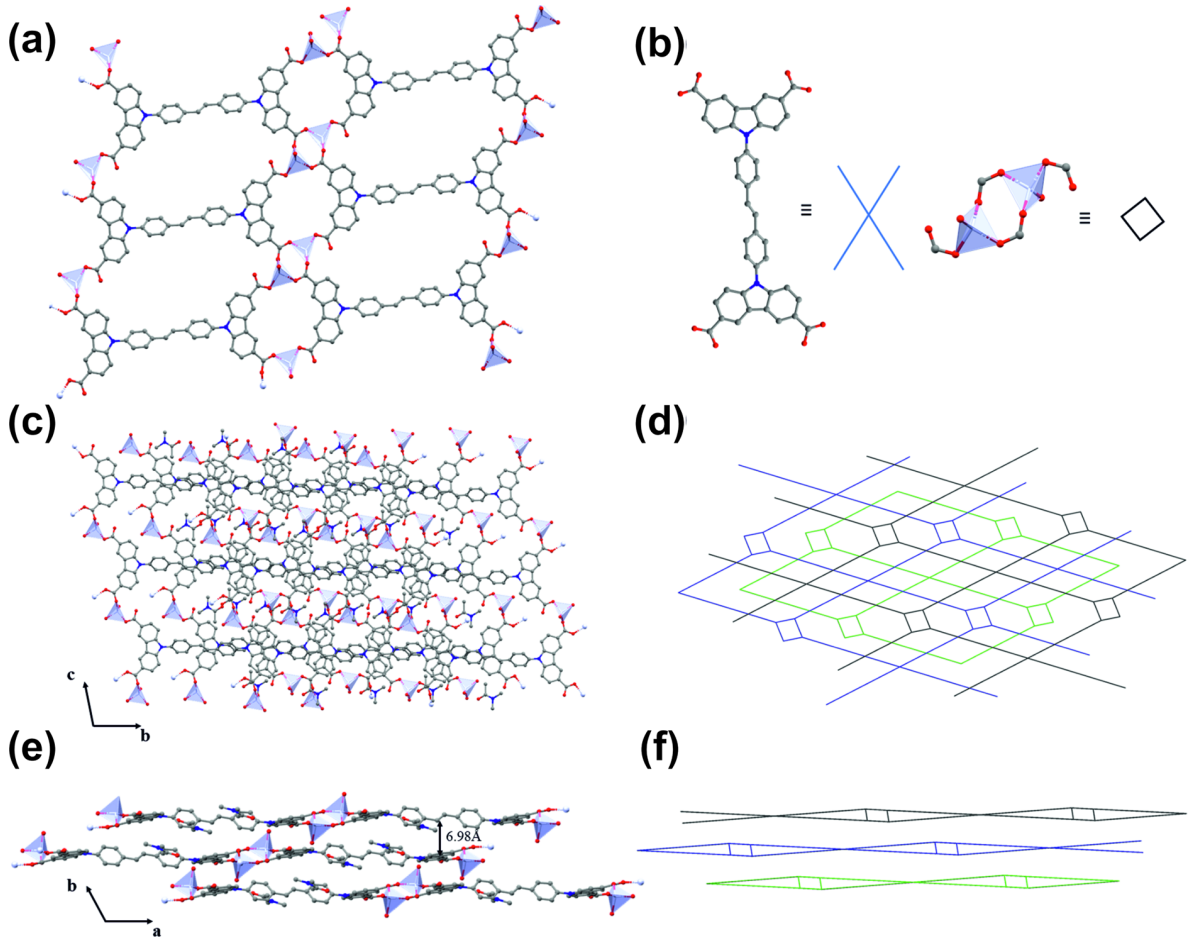

Figure 3. (a) Depiction of a monolayer cut-out of the Zn_2(sbcd)$(DMAc)_2(H_2O)_{1.5}$ 2D-CP. (b) Depiction of the SBU containing two Zn^{2+} atoms with four coordinated oxygen atoms and representation of the four-connecting stilbene linker. (c) Depiction of the crystal structure of the network alongside the *a*-axis. (d) Schematic representation of the underlying network topology of the *sql*-network topology alongside the *a*-axis. (e) Depiction of the parallel packing of the network layers with a mean chromophore distance of 6.98 Å alongside the *ab*-plane. (f) Schematic representation of the underlying network topology along the *c*-axis. Note: hydrogen atoms are omitted for clarity. Color coding: gray = carbon, blue = nitrogen, red = oxygen, and light gray = zinc.

https://doi.org/10.1021/acs.chemmater.2c01525
Chem. Mater. 2022, 34, 7402−7411

Ba(fbcd)(DMAc)$_{2.5}$(H$_2$O)$_{1.5}$. In a 4 mL screw cap vial, 10 mg of H_4fbcd and 11.12 mg of $Ba(NO_3)_2$ (3 equiv) were dissolved in a DMAc/water mixture (2/0.25 mL) and heated at 100 °C for 2 days. The resulting precipitate was filtered, washed with DMAc, and dried to give white crystalline needles (6.7 mg, 43%). EA calcd for $BaC_{43}H_{26}N_2O_8{\cdot}2.5C_4H_9O{\cdot}1.5H_2O$: C, 58.9; H, 4.8; N, 6.01. Found: C, 58.9; H, 4.87; N, 6.01.

RESULTS AND DISCUSSION

Synthesis of the Carbazole-Based Donor−π−Donor-Linker Molecules. The synthesis of the chromophore units (Figure 2) that were incorporated in the CP starts with the carbazole donor **1** synthesis, which was previously published by our group in 2020 (cf. Supporting Information).[20] Being a reliable synthesis method for C−N hetero-coupling reactions for carbazoles, the *Ullmann* reaction using copper as a metal catalyst was employed. Therefore, first, the halogenated aromatic cores have to be synthesized in order to subsequently couple them with the carbazole moiety.

For the synthesis of the stilbene core, a *McMurry* reaction with 4-bromobenzaldehyde using titanium tetrachloride as a reduction agent was performed, yielding 4,4′-dibromostilbene **2** according to a synthesis procedure by Jeong and co-workers.[25] In principle, **2** could be used directly for a subsequent *Ullmann* reaction as it was reported earlier by Krause et al. in 2020.[22] However, we found that the reaction time of 10 days can be significantly reduced via an additional synthetic step to substitute the bromine atoms with iodine, making the molecule more reactive toward the coupling. Within this improved synthesis, a bromine−iodine exchange reaction was performed using butyllithium for the bromine−metal exchange, followed by addition of iodine solution in THF for the metal−iodine exchange to yield **3**. Finally, via *Ullmann* reaction following our previously reported protocol, the stilbene core is coupled to the carbazole moiety using a copper catalyst ligated with two molecules of *N*,*N*-dimethylethylenediamine, leading to **4** in good purity and yields. As a last step toward the final linker, the ester groups are saponificated via alkaline hydrolysis reaction with NaOH, yielding **5** in excellent purity.

For the synthesis of the fluorene core, first, the terminal 2 and 7 positions were subjected to a substitution reaction using a periodic acid and elemental iodine in a solvent mixture of acetic acid, water, and sulfuric acid toward **6**, in accordance with Tsutsui and co-workers from 2001.[26] Afterward, the two protons at position 9 of the synthesized 2,7-diiodofluorene have to be substituted since they would hinder the following *Ullmann* reaction due to their acidic character. This was done according to an adapted synthesis procedure from a publication by West et al., where first the fluorene is deprotonated with potassium-*tert*-butoxide and afterward by adding methyliodine as an electrophilic reagent, yielding 9,9′-dimethyl-2,7-diiodofluorene **7**.[27] The aromatic core is then also coupled with the carbazole moiety using the same conditions and the same work-up procedure as for **4**, resulting in excellent yields and purity for **8** and later on after alkaline hydrolysis for **9**.

SC-XRD Analysis of the Coordination Polymers. *SC-XRD Analysis of Zn$_2$(sbcd)(DMAc)$_2$(H$_2$O)$_{1.5}$.* After 2 days reaction time of a one-batch solvothermal synthesis using $Zn(NO_3)_2$, DMAc, and water, small frost flower-shaped single crystals could be obtained, which were analyzed via SC-XRD. It revealed that the CP Zn$_2$(sbcd)(DMAc)$_2$(H$_2$O)$_{1.5}$ crystallizes in the triclinic space group *P*-1 with its unit cell parameters of a = 9.256(3) Å, b = 11.735(4) Å, and c = 12.319(4) Å and the respective cell angles of α = 73.267(10)°, β = 78.637(8)°, and γ = 68.362° with two linker-node moieties per unit cell (Z = 2).

In Figure 3a, a monolayer cut-out of the CP is depicted, showing that two carboxylic acid group atoms connect two zinc centers, forming a Zn_2O_8 cluster as a secondary building unit (SBU) with two water molecules on the top of each tetrahedron (Figure 3b). These SBUs in turn connect four linker molecules, which leads to a 2D sheet-like *sql*-network topology. Alongside the *b*/*c*-plane, the shifted stacking of each layer can be seen in Figure 3c, which means that the carbazole units are lying over the stilbene moieties. This is further illustrated in a schematic representation of the whole network in Figure 3d. This can also be observed in Figure 3e,f alongside the *c*-axis, where the side view of the packing is depicted, which reveals an interchromophoric distance of 6.98 Å.

In Figure 4, the powder X-ray diffractogram of Zn$_2$(sbcd)-(DMAc)$_2$(H$_2$O)$_{1.5}$ is depicted, which shows a high degree of crystallinity and intense reflections at 3.75, 4.50, 6.11, 9.95, 7.58, 9.02, and 10.11°. Pawley fit on the data reveals an R_{wp} value of 5.01% and a goodness of fit (GoF) of 4.95, which shows that the proposed structure model is in good agreement with the bulk material.

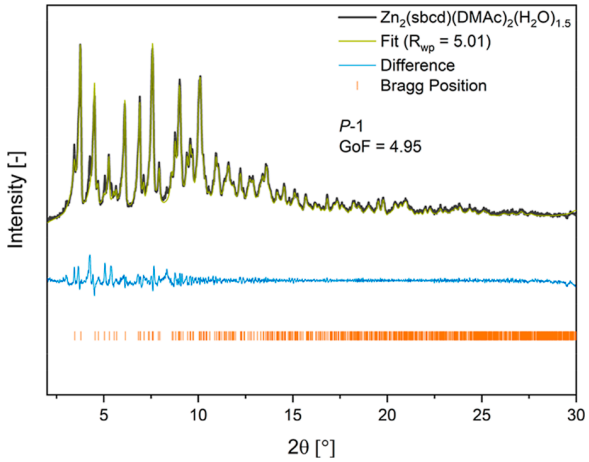

Figure 4. Plot of the powder XRD data of the Zn$_2$(sbcd)-(DMAc)$_2$(H$_2$O)$_{1.5}$ network (dark gray), the simulated Pawley fit (green), the difference plot (blue), and the Bragg positions (orange).

SC-XRD Analysis of Sr(fbcd)(DMAc)$_{0.25}$(H$_2$O)$_{3.5}$ and Ba-(fbcd)(DMAc)$_{2.5}$(H$_2$O)$_{1.5}$. After 2 days of solvothermal synthesis using H_4fbcd as a linker mixed with either strontium or barium in a dimethylacetamide/water mixture, needle-shaped single crystals suitable for SC-XRD could be obtained. Analysis of single crystals of the strontium CP revealed that it crystallizes in the triclinic space *P*-1 with the unit cell lengths of a = 10.076(3) Å, b = 12.140(3) Å, and c = 23.401(6) Å and cell angles of α = 93.793(7)°, β = 90.197(8)°, and γ = 93.276(8)° with two linker-node moieties per unit cell (Z = 2). The barium-based CP crystallizes in the monoclinic space group $P2_1/n$ with the cell axis lengths of a = 12.1780(10) Å, b = 20.5805(17) Å, and c = 46.760(4) Å and its monoclinic angle of β = 90.270(2)° with four linker-node moieties per unit cell (Z = 4).

https://doi.org/10.1021/acs.chemmater.2c01525
Chem. Mater. 2022, 34, 7402−7411

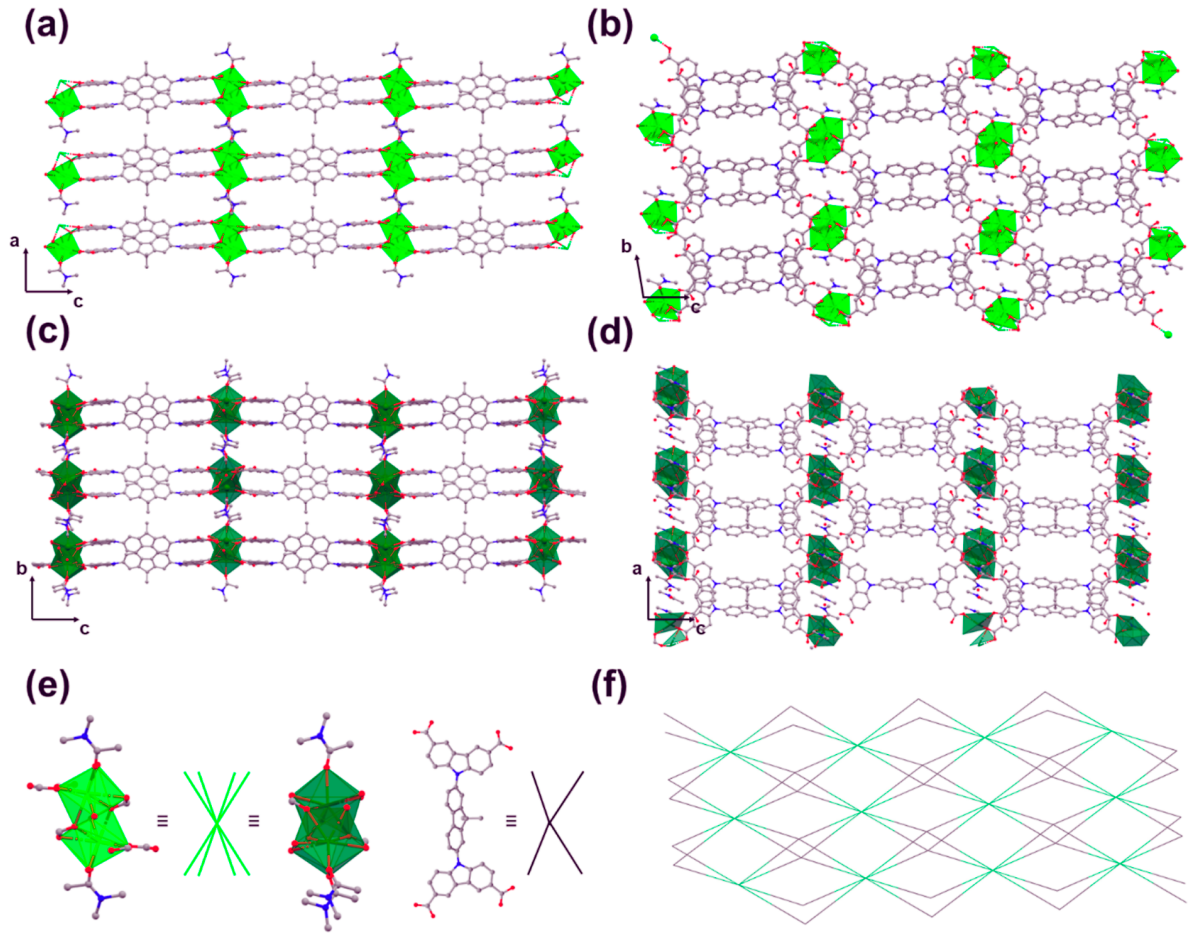

Figure 5. (a) Side view alongside the *a*/*c*-plane of the 2D coordination network of $Sr(fbcd)(DMAc)_{0.25}(H_2O)_{3.5}$. (b) Depiction of a monolayer cut-out of $Sr(fbcd)(DMAc)_{0.25}(H_2O)_{3.5}$ along the *a*-axis. (c) Side view alongside the *b*/*c*-plane of the 2D coordination network of $Ba(fbcd)(DMAc)_{2.5}(H_2O)_{1.5}$. (d) Depiction of a monolayer cut-out of $Ba(fbcd)(DMAc)_{2.5}(H_2O)_{1.5}$ along the *b*-axis. (e) Depiction of the Sr_2O_{12} SBU (left) containing two coordinated DMAc molecules and the Ba_2O_{15} SBU (right) containing three coordinated DMAc molecules and representation of the four-connecting fluorene-based linker. (f) Schematic representation of the underlying 4,8-c network topology for both CPs. Note: hydrogen atoms are omitted for clarity. Color coding: gray = carbon, blue = nitrogen, red = oxygen, light green = strontium, and dark green = barium.

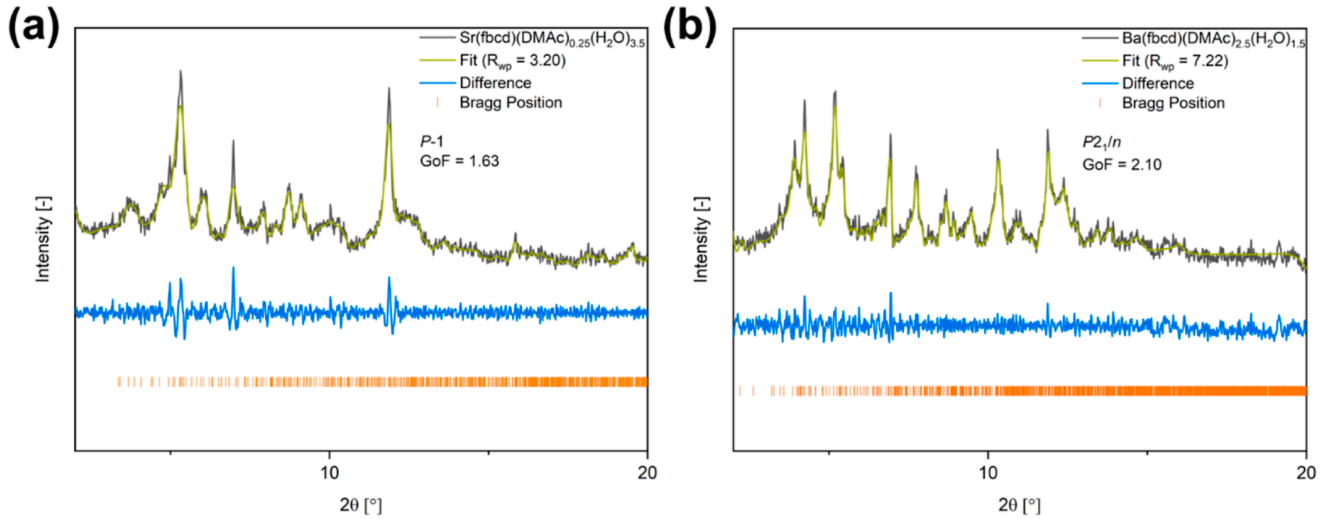

Figure 6. Plot of the measured powder XRD data (dark gray), the simulated Pawley fit (green), the difference plot (blue), and the Bragg positions (orange) of (a) $Sr(fbcd)(DMAc)_{0.25}(H_2O)_{3.5}$ and (b) $Ba(fbcd)(DMAc)_{2.5}(H_2O)_{1.5}$.

https://doi.org/10.1021/acs.chemmater.2c01525
Chem. Mater. 2022, 34, 7402−7411

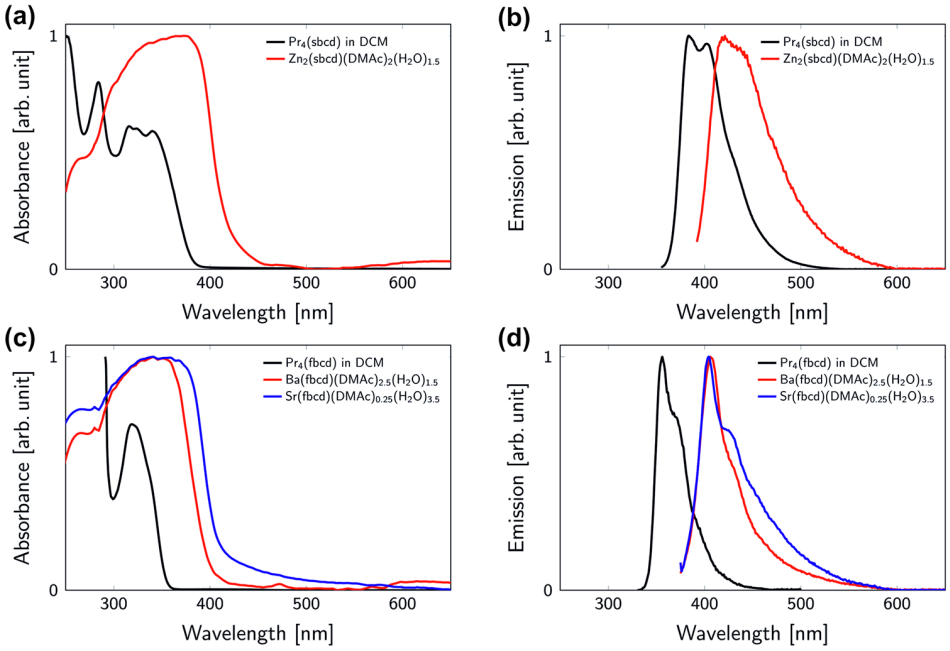

Figure 7. (a) UV/vis spectra of the linker Pr_4(sbcd) in DCM solution (black) and its corresponding zinc CP (red) in the solid state. (b) Emission spectra of the linker Pr_4(sbcd) in DCM solution (black) and its corresponding CP (red) in the solid state. (c) UV/vis spectra of the linker Pr_4(fbcd) in DCM solution (black) and its corresponding strontium CP (blue) and barium CP (red) in the solid state. (d) Emission spectra of the linker Pr_4(fbcd) in DCM solution (black) and its corresponding strontium CP (blue) and barium CP (red) in the solid state.

In Figure 5a, $Sr(fbcd)(DMAc)_{0.25}(H_2O)_{3.5}$ 2D layers are depicted, which are parallel-packed alongside the *a*/*c*-plane with an intralayer chromophore distance of 3.39 Å and an interlayer distance of 10.08 Å. This monolayer can be seen in Figure 5b, which shows a parallel packing of always pairs of two chromophores with an inversed fluorene center. For the barium-based $Ba(fbcd)(DMAc)_{2.5}(H_2O)_{1.5}$ CP, the same packing of chromophores is observed with a slightly larger intralayer chromophore distance of 3.65 Å and a smaller interlayer distance of 9.044 Å (Figure 5c,d). However, their overall topology of a 4,8-c network (Figure 5f) is the same for both CPs, which renders them being isostructural. A main difference can be observed in their SBUs because the strontium-based SBU has two strontium ions with two dimethylacetamide molecules coordinated at each metal forming a Sr_2O_{12} metal-oxo-cluster, whereas the barium-based CP has a Ba_2O_{15} metal oxo-cluster with three dimethylacetamide molecules coordinated to the SBU (Figure 5e).

In Figure 6, the measured powder X-ray diffractogram of the CPs is depicted, which also shows a high degree of crystallinity for both materials. The strontium-based CP shows intense reflections at 5.32, 6.98, and 11.97°, whereas the barium-based CP shows 4.23, 5.18, 6.94, 7.73, 10.29, and 11.87°. Pawley fit on both networks reveals a R_{wp} value of 3.20% for Sr-CP and 7.22% for Ba-CP as well as a goodness of fit (GoF) of 1.63 and 2.10, respectively, which indicates that structure models agree very well with the respective bulk material.

Photophysical Characterization of the CPs and Their Linkers. *Steady-State Spectroscopy of CPs and Linkers.* For a primary investigation of the photophysical properties of the synthesized materials, steady-state spectroscopy was performed (Figure 7) along with IR spectroscopy (cf. Figure S10). The absorption spectrum of the stilbene-based linker molecule shows four absorption bands located at 250, 270, 320, and 350 nm, which can be mainly attributed to $n-\pi^*$ and $\pi-\pi^*$ transitions as the linker molecule is dominated by its aromatic core structure (Figure 7a). However, the absorption spectrum of the respective CP shows a red shift of absorption bands of approximately 50 nm, leading to a broad strong absorption around 400 nm. When we assume that the solvent-related effects to the absorption spectra are negligible (Figure S18) and note that the linker and CP spectra were measured in DCM and in the solid state, respectively, the observed red shift can be explained by the excitonic interaction of the chromophores within the CP as the same trend can be seen for solid linker powder (Figure S19). In this environment, the interchromophore distance is strongly reduced as compared to the solvated, isolated chromophores.[28] A red shift of a similar magnitude is also observed when comparing the emission spectrum of the free linker with the emission spectrum of the CP in Figure 7b. We note that the transition in the visible range (above 550 nm in Figure 7a) is due to scattered light and does not represent a molecular transition; accordingly, the stilbene-based CP is a white powder. The absorption spectrum of the fluorene-based linker molecule shows two absorption bands located at 290 and 320 nm, tentatively attributed to transitions of the aromatic rings of the fluorene linker. The respective CP absorption spectra are broadened and featureless as compared to the linker. This holds true regardless of the choice of metal, that is, Sr or Ba (Figure 7c). The emission spectra however reveal a clear 50 nm red shift of the CPs (Figure 7d).

Z-Scan Measurements. Nonlinear optical properties of CPs $Zn_2(sbcd)(DMAc)_2(H_2O)_{1.5}$, $Sr(fbcd)(DMAc)_{0.25}(H_2O)_{3.5}$, and $Ba(fbcd)(DMAc)_{2.5}(H_2O)_{1.5}$ were characterized using the open-aperture Z-scan technique,[23,29] which is a method that allows one to extract two-photon absorption coefficient β by fitting the measured Z-scan traces (see the Supporting Information for more details). Afterward, values of two-photon

https://doi.org/10.1021/acs.chemmater.2c01525
Chem. Mater. 2022, 34, 7402−7411

Table 1. Two-Photon Absorption (Action) Cross-Sections of the Reported CPs/MOFs over Excitation Wavelengths Ranging from 550 to 960 nm

CPs/MOFs	2PA cross-section $\sigma^{(2)}$ (10^3 GM)	2PA action cross-section $\eta\sigma^{(2)}$ (10^3 GM)	literature
$Zn_2(sbcd)(DMAc)_2(H_2O)_{1.5}$	2.137−15.838		this work
$Sr(fbcd)(DMAc)_{0.25}(H_2O)_{3.5}$	20.724−33.355		this work
$Ba(fbcd)(DMAc)_{2.5}(H_2O)_{1.5}$	3.054−10.415		this work
$Zn_2(benzoate)_4(An2Py)_2$	0.89		36
$Zr/CO_2CF_3/TCPE_{kagome}$		3.582	30
$Zr/OH/TCPE_{kagome}$		2.59	30
$Zr_6O_4(OH)_8(ETTC)_2(H_2O)_4$		2.217	37
$Zn_2(TCPPE)$ (complex 1)		1.2×10^3 to 7.4×10^4	38

absorption cross-section $\sigma^{(2)}$ can be calculated accordingly and expressed in the unit of Göppert-Mayer GM (1 GM = 10^{-50} $cm^4 \cdot s \cdot photon^{-1} \cdot molecule^{-1}$). All three CP samples were prepared in a PMMA film with a thickness of c.a. 0.05 mm attached on a 1 mm thick quartz glass substrate; the calculated concentrations are in the range of 28−55 mM (see sample preparation, Supporting Information Section S8).

The preparation of MOF/CP samples for a given nonlinear characterization technique has proved to be challenging. Medishetty et al. and Quah et al. performed the measurements based on solid-state multiphoton excited fluorescence (SSMPEF) by packing MOF powders in a thin quartz cuvette to measure the MPA-induced fluorescence detected orthogonally with respect to the excitation beam.[30,31] In order to do so, one needs to find a standard sample as a reference (e.g., solid perylene or rhodamine dyes). In our method, we disperse the fine ground CP crystals in the PMMA film, which brings us several advantages. As compared to solid-state powders, the sample concentration can be defined more properly. This is advantageous for the Z-scan technique as it is transmission-based and sets demands for an optimal concentration regime. In the context of the measurements presented here, Z-scan is advantageous as the two-photon absorption cross-sections are measured directly and no reference sample is required. Unlike Z-scan, fluorescence-based methods (e.g., SSMPEF) require information of quantum efficiency η to calculate the 2PA cross-section $\sigma^{(2)}$. If η is not known, 2PA action cross-section $\eta\sigma^{(2)}$ is a commonly accepted parameter to quantify 2PA cross-section (Table 1).

The excitation range of the employed femtosecond oscillator is from 700 to 950 nm. $Zn_2(sbcd)(DMAc)_2(H_2O)_{1.5}$ gives $\sigma^{(2)}$ values in the range of 2137−15,838 GM. The H_4fbcd-based CPs $Sr(fbcd)(DMAc)_{0.25}(H_2O)_{3.5}$ (20,724−33,355 GM) and $Ba(fbcd)(DMAc)_{2.5}(H_2O)_{1.5}$ (3054−10,415 GM) exhibit $\sigma^{(2)}$ values that are 1 order of magnitude higher (Figure 8). Furthermore, $Sr(fbcd)(DMAc)_{0.25}(H_2O)_{3.5}$ shows two-photon cross-section values that are outcompeting most of the common state-of-the-art materials like organic lumophores, which normally show cross-sections in the range of 1×10^3 to 1×10^5 GM.[32,33] Additionally, for H_4tcpe-based MOFs (H_4tcpe = tetrakis[4-(4-carboxyphenyl)phenyl]ethylene), Medishetty et al. observed a maximum $\eta\sigma^{(2)}$ value of 3582 GM (Table 1). The appreciable enhancement of two-photon absorption of three CPs discussed here is attributed to the replacement of H_4tcpe (55 GM) with linkers exhibiting higher 2PA cross-sections, for example, H_4fbcd (170 GM).[30] When retaining H_4fbcd as a linker but selecting different metal ions, strontium-based materials exhibit a 3-fold increase of $\sigma^{(2)}$ values when compared to the barium CP. Both barium and strontium have the same charge, but the latter has a smaller ion

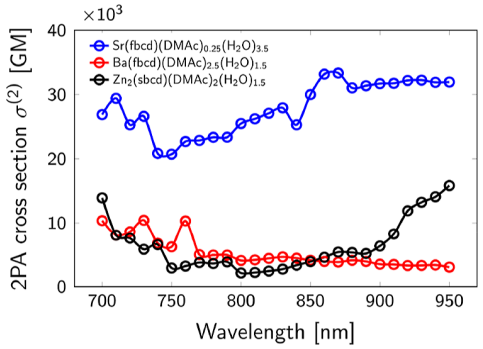

Figure 8. Comparison of the two-photon absorption cross-sections of the three CPs. Color coding: blue = $Sr(fbcd)(DMAc)_{0.25}(H_2O)_{3.5}$, red = $Ba(fbcd)(DMAc)_{2.5}(H_2O)_{1.5}$, and black = $Zn_2(sbcd)(DMAc)_2(H_2O)_{1.5}$. The error is estimated as 10%, mainly from the laser stabilities[23] and the determination of sample thicknesses.

radius, making strontium a "harder" ion; strontium can in turn polarize the chromophore more, which leads to an increase of the charge-transfer character of the chromophore. Similar effects are reported in the literature, showing that the choice of metal ions has an influence on the charge-transfer character.[34] When examining the structure of $Sr(fbcd)(DMAc)_{0.25}(H_2O)_{3.5}$ and $Ba(fbcd)(DMAc)_{2.5}(H_2O)_{1.5}$, we find that the carbazole−carbazole distance between the layers is decreased in the strontium case (3.39 vs 3.65 Å). It is the carbazole units that define the charge-transfer character of the ligand and therewith the 2PA cross-section.[14,35] Therefore, we hypothesize that the above-mentioned structural differences are another factor explaining the altered two-photon activity observed for the two CPs.

CONCLUSIONS AND OUTLOOK

In conclusion, we have synthesized and photophysically characterized two MPA-active chromophores, H_4sbcd and H_4fbcd, which were successfully incorporated into three MPA-active CPs. These CPs ($Zn_2(sbcd)(DMAc)_2(H_2O)_{1.5}$, $Sr(fbcd)(DMAc)_{0.25}(H_2O)_{3.5}$, and $Ba(fbcd)(DMAc)_{2.5}(H_2O)_{1.5}$) were investigated through single-crystal XRD, revealing that the three CPs are 2D CPs. The zinc-based CP shows an *sql*-network topology, whereas the main group CPs show a 4,8-c net topology. Steady-state spectroscopy of the free linkers compared to networks displays a red shift of the absorption and emission bands, which is due to dipole interactions of the chromophores inside the solid framework. Investigation of the MPA properties using the Z-scan technique showed that the three CPs exhibit high two-photon absorption cross-sections $\sigma^{(2)}$ of 10,415−33,355 GM, which are among highest cross-sections reported for MPA-active CPs (Table 1).[37] Very

https://doi.org/10.1021/acs.chemmater.2c01525
Chem. Mater. 2022, 34, 7402−7411

recently, Vittal and co-workers synthesized five MOF complexes utilizing H_4tcpe.[38] Surprisingly, one of the obtained complexes showed extremely large $\eta\sigma^{(2)}$ values (≈1.2 × 10^6 to 7.4 × 10^7 GM), which are among the highest $\eta\sigma^{(2)}$ values reported for MOFs/CPs up to date (Table 1).

As a perspective, we aim to further develop the MPA efficiency of these CP materials by combining the presented strong multiphoton absorbing chromophores (H_4sbcd and H_4fbcd) with the topological approach published by Vittal and co-workers,[38] which will potentially lead to modular tunable MPA materials significantly outcompeting the state of the art.

■ ASSOCIATED CONTENT

Supporting Information

The Supporting Information is available free of charge at https://pubs.acs.org/doi/10.1021/acs.chemmater.2c01525.

Additional synthetic procedures; NMR spectra; IR and TGA; Z-scan data processing; and single-crystal X-ray data (PDF)

Crystallographic data of Sr(fbcd) (CIF)

Crystallographic data of Zn(sbcd) (CIF)

Crystallographic data of Ba(fbcd) (CIF)

Accession Codes

Crystallographic data are available from the Cambridge Crystallographic Data Centre under the CCDC deposition numbers 2173885 (Zn(sbcd)), 2173886 (Sr(fbcd)), and 2173887 (Ba(fbcd)).

■ AUTHOR INFORMATION

Corresponding Authors

Jürgen Hauer − *Professorship for Dynamic Spectroscopy, Technical University of Munich, 85748 Garching, Germany;* orcid.org/0000-0002-6874-6138; Email: juergen.hauer@tum.de

Alexander Pöthig − *Chair of Inorganic and Metal−Organic Chemistry, Department of Chemistry & Catalysis Research Center, Technical University of Munich, 85748 Garching, Germany;* orcid.org/0000-0003-4663-3949; Email: alexander.poethig@tum.de

Roland A. Fischer − *Chair of Inorganic and Metal−Organic Chemistry, Department of Chemistry & Catalysis Research Center, Technical University of Munich, 85748 Garching, Germany;* orcid.org/0000-0002-7532-5286; Email: roland.fischer@tum.de

Authors

Sebastian J. Weishäupl − *Chair of Inorganic and Metal−Organic Chemistry, Department of Chemistry & Catalysis Research Center, Technical University of Munich, 85748 Garching, Germany*

Yang Cui − *Professorship for Dynamic Spectroscopy, Technical University of Munich, 85748 Garching, Germany; Department of Physics, Technical University of Munich, 85748 Garching, Germany;* orcid.org/0000-0003-2116-7611

Simon N. Deger − *Chair of Inorganic and Metal−Organic Chemistry, Department of Chemistry & Catalysis Research Center, Technical University of Munich, 85748 Garching, Germany*

Hamad Syed − *3D Printing and Biofabrication Group, Institute of Materials Science and Technology, Technische Universität Wien (TU Wien), 1060 Vienna, Austria*

Aleksandr Ovsianikov − *3D Printing and Biofabrication Group, Institute of Materials Science and Technology, Technische Universität Wien (TU Wien), 1060 Vienna, Austria*

Complete contact information is available at: https://pubs.acs.org/10.1021/acs.chemmater.2c01525

Author Contributions

⊥S.J.W. and Y.C. contributed equally to this work.

Author Contributions

Conceptualization and writing, original draft preparation, S.J.W. and Y.C.; synthesis and characterization, S.J.W. and S.N.D.; photophysical characterization, S.J.W., Y.C., and H.S.; methodology, S.J.W., Y.C., J.H., and A.P.; writing, review, and editing, J.H., A.O., A.P., and R.A.F.; project administration, R.A.F. All authors have given approval to the final version of the manuscript.

Funding

The authors would like to thank the German Research Foundation (DFG) for funding within the frame of EXC 2089 Cluster of Excellence and the Priority Programme "COOR-NETs" (SPP 1928).

Notes

The authors declare no competing financial interest.

■ ACKNOWLEDGMENTS

The TUM is very greatly acknowledged for institutional funding. S.J.W. and Y.C. would like to thank the TUM Graduate School for financial support. S.J.W. would like to thank Johannes Voigtland for experiments and Silva Kronawitter for measurement support. Y.C. would like to thank Franziska Chalupa-Gantner for measurement support.

■ REFERENCES

(1) Munn, R. W. Nonlinear optical phenomena. In *Principles and Applications of Nonlinear Optical Materials*; Munn, R. W., Ironside, C. N., Eds.; Springer Netherlands: Dordrecht, 1993; pp 5−19.

(2) Medishetty, R.; Zaręba, J. K.; Mayer, D.; Samoć, M.; Fischer, R. A. Nonlinear optical properties, upconversion and lasing in metal−organic frameworks. *Chem. Soc. Rev.* **2017**, *46*, 4976−5004.

(3) Mingabudinova, L. R.; Vinogradov, V. V.; Milichko, V. A.; Hey-Hawkins, E.; Vinogradov, A. V. Metal−organic frameworks as competitive materials for non-linear optics. *Chem. Soc. Rev.* **2016**, *45*, 5408−5431.

(4) Zaręba, J. K.; Nyk, M.; Samoć, M. Nonlinear Optical Properties of Emerging Nano- and Microcrystalline Materials. *Adv. Opt. Mater.* **2021**, *9*, 2100216.

(5) Shi, R.; Han, X.; Xu, J.; Bu, X.-H. Crystalline Porous Materials for Nonlinear Optics. *Small* **2021**, *17*, 2006416.

(6) Zhou, J. R. L.; Long, O. M.; Yaghi, O. M. Introduction to Metal−Organic Frameworks. *Chem. Rev.* **2012**, *112*, 673−674.

(7) Wang, Q.; Astruc, D. State of the Art and Prospects in Metal−Organic Framework (MOF)-Based and MOF-Derived Nanocatalysis. *Chem. Rev.* **2020**, *120*, 1438−1511.

(8) Allendorf, M. D.; Bauer, C. A.; Bhakta, R. K.; Houk, R. J. T. Luminescent metal−organic frameworks. *Chem. Soc. Rev.* **2009**, *38*, 1330−1352.

(9) Hu, Z.; Huang, G.; Lustig, W. P.; Wang, F.; Wang, H.; Teat, S. J.; Banerjee, D.; Zhang, D.; Li, J. Achieving exceptionally high luminescence quantum efficiency by immobilizing an AIE molecular chromophore into a metal−organic framework. *Chem. Commun.* **2015**, *51*, 3045−3048.

(10) Wei, Z.; Gu, Z.-Y.; Arvapally, R. K.; Chen, Y.-P.; McDougald, R. N.; Ivy, J. F.; Yakovenko, A. A.; Feng, D.; Omary, M. A.; Zhou, H.-

C. Rigidifying Fluorescent Linkers by Metal−Organic Framework Formation for Fluorescence Blue Shift and Quantum Yield Enhancement. *J. Am. Chem. Soc.* **2014**, *136*, 8269−8276.
(11) Shustova, N. B.; Ong, T.-C.; Cozzolino, A. F.; Michaelis, V. K.; Griffin, R. G.; Dincă, M. Phenyl Ring Dynamics in a Tetraphenylethylene-Bridged Metal−Organic Framework: Implications for the Mechanism of Aggregation-Induced Emission. *J. Am. Chem. Soc.* **2012**, *134*, 15061−15070.
(12) Mayer, D. C.; Manzi, A.; Medishetty, R.; Winkler, B.; Schneider, C.; Kieslich, G.; Pöthig, A.; Feldmann, J.; Fischer, R. A. Controlling Multiphoton Absorption Efficiency by Chromophore Packing in Metal−Organic Frameworks. *J. Am. Chem. Soc.* **2019**, *141*, 11594−11602.
(13) Mayer, D. C.; Zaręba, J. K.; Raudaschl-Sieber, G.; Pöthig, A.; Chołuj, M.; Zaleśny, R.; Samoć, M.; Fischer, R. A. Postsynthetic Framework Contraction Enhances the Two-Photon Absorption Properties of Pillar-Layered Metal−Organic Frameworks. *Chem. Mater.* **2020**, *32*, 5682−5690.
(14) Weishäupl, S. J.; Mayer, D. C.; Cui, Y.; Kumar, P.; Oberhofer, H.; Fischer, R. A.; Hauer, J.; Pöthig, A. Recent advances of multiphoton absorption in metal−organic frameworks. *J. Mater. Chem. C* **2022**, *10*, 6912−6934.
(15) Vogler, A.; Kunkely, H. Charge Transfer Excitation of Coordination Compounds. Generation of Reactive Intermediates. In *Photosensitization and Photocatalysis Using Inorganic and Organometallic Compounds*; Kalyanasundaram, K., Grätzel, M., Eds.; Springer Netherlands: Dordrecht, 1993; pp 71−111.
(16) He, X.; Xu, B.; Liu, Y.; Yang, Y.; Tian, W. Effect of intramolecular charge transfer on the two-photon absorption behavior of multibranched triphenylamine derivations. *J. Appl. Phys.* **2012**, *111*, 053516.
(17) Jia, J.; Wu, X.; Zhang, X.; Wang, Y.; Yang, J.; Fang, Y.; Song, Y. Effect of intramolecular charge transfer on nonlinear optical properties of chalcone derivatives: a visual description of the charge transfer process. *Phys. Chem. Chem. Phys.* **2022**, *24*, 955−965.
(18) Dar, A. H.; Gowri, V.; Gopal, A.; Muthukrishnan, A.; Bajaj, A.; Sartaliya, S.; Selim, A.; Ali, M. E.; Jayamurugan, G. Designing of Push−Pull Chromophores with Tunable Electronic and Luminescent Properties Using Urea as the Electron Donor. *J. Org. Chem.* **2019**, *84*, 8941−8947.
(19) He, G. S.; Tan, L.-S.; Zheng, Q.; Prasad, P. N. Multiphoton Absorbing Materials: Molecular Designs, Characterizations, and Applications. *Chem. Rev.* **2008**, *108*, 1245−1330.
(20) Weishäupl, S. J.; Mayer, D. C.; Thyrhaug, E.; Hauer, J.; Pöthig, A.; Fischer, R. A. A nitrophenyl-carbazole based push-pull linker as a building block for non-linear optical active coordination polymers: A structural and photophysical study. *Dyes Pigm.* **2021**, *186*, 109012.
(21) Sippola, R. J.; Hadipour, A.; Kastinen, T.; Vivo, P.; Hukka, T. I.; Aernouts, T.; Heiskanen, J. P. Carbazole-based small molecule electron donors: Syntheses, characterization, and material properties. *Dyes Pigm.* **2018**, *150*, 79−88.
(22) Krause, S.; Evans, J. D.; Bon, V.; Senkovska, I.; Ehrling, S.; Iacomi, P.; Többens, D. M.; Wallacher, D.; Weiss, M. S.; Zheng, B.; Yot, P. G.; Maurin, G.; Llewellyn, P. L.; Coudert, F.-X.; Kaskel, S. Engineering micromechanics of soft porous crystals for negative gas adsorption. *Chem. Sci.* **2020**, *11*, 9468−9479.
(23) Steiger, W.; Gruber, P.; Theiner, D.; Dobos, A.; Lunzer, M.; Van Hoorick, J.; Van Vlierberghe, S.; Liska, R.; Ovsianikov, A. Fully automated z-scan setup based on a tunable fs-oscillator. *Opt. Mater. Express* **2019**, *9*, 3567−3581.
(24) Muhr, M.; Heiß, P.; Schütz, M.; Bühler, R.; Gemel, C.; Linden, M. H.; Linden, H. B.; Fischer, R. A. Enabling LIFDI-MS measurements of highly air sensitive organometallic compounds: a combined MS/glovebox technique. *Dalton Trans.* **2021**, *50*, 9031−9036.
(25) Li, Q.; Shin, S. M.; Moon, D.; Jeong, K. S.; Jeong, N. Chiral porous metal−organic frameworks from chiral building units with different metrics. *CrystEngComm* **2013**, *15*, 10161−10164.
(26) Lee, S. H.; Nakamura, T.; Tsutsui, T. Synthesis and Characterization of Oligo(9,9-dihexyl-2,7-fluorene ethynylene)s: For Application as Blue Light-Emitting Diode. *Org. Lett.* **2001**, *3*, 2005−2007.
(27) West, K.; Wang, C.; Batsanov, A. S.; Bryce, M. R. Carbon-rich molecules: synthesis and isolation of aryl/heteroaryl terminal bis(butadiynes)(HC−C−C−C−Ar−C−C−C−CH) and their applications in the synthesis of oligo(arylenebutadiynylene) molecular wires. *Org. Biomol. Chem.* **2008**, *6*, 1934−1937.
(28) Valkunas, L.; Abramavicius, D.; Mančal, T. Quantum States of Molecules and Aggregates. In *Molecular Excitation Dynamics and Relaxation*; Wiley, 2013; pp 101−132.
(29) Sheik-Bahae, M.; Said, A. A.; Van Stryland, E. W. High-sensitivity, single-beam *n_2* measurements. *Opt. Lett.* **1989**, *14*, 955−957.
(30) Medishetty, R.; Nemec, L.; Nalla, V.; Henke, S.; Samoć, M.; Reuter, K.; Fischer, R. A. Multi-Photon Absorption in Metal−Organic Frameworks. *Angew. Chem., Int. Ed.* **2017**, *56*, 14743−14748.
(31) Quah, H. S.; Chen, W.; Schreyer, M. K.; Yang, H.; Wong, M. W.; Ji, W.; Vittal, J. J. Multiphoton harvesting metal−organic frameworks. *Nat. Commun.* **2015**, *6*, 7954.
(32) Kim, H. M.; Rae Cho, B. Two-photon materials with large two-photon cross sections. Structure−property relationship. *Chem. Commun.* **2009**, 153−164.
(33) Sadowski, B.; Kita, H.; Grzybowski, M.; Kamada, K.; Gryko, D. T. π-Expanded Dipyrrolonaphthyridinediones with Large Two-Photon Absorption Cross-Section Values. *J. Org. Chem.* **2017**, *82*, 7254−7264.
(34) Few, S.; Frost, J. M.; Kirkpatrick, J.; Nelson, J. Influence of Chemical Structure on the Charge Transfer State Spectrum of a Polymer:Fullerene Complex. *J. Phys. Chem. C* **2014**, *118*, 8253−8261.
(35) Jagatap, B. N.; Meath, W. J. Contributions of permanent dipole moments to molecular multiphoton excitation cross sections. *J. Opt. Soc. Am. B* **2002**, *19*, 2673−2681.
(36) Liu, M.; Quah, H. S.; Wen, S.; Li, Y.; Vittal, J. J.; Ji, W. Multiphoton absorption and two-photon-pumped random lasing in crystallites of a coordination polymer. *J. Phys. Chem. C* **2018**, *122*, 777−781.
(37) Chen, C. X.; Yin, S. Y.; Wei, Z. W.; Qiu, Q. F.; Zhu, N. X.; Fan, Y. N.; Pan, M.; Su, C. Y. Pressure-Induced Multiphoton Excited Fluorochromic Metal−Organic Frameworks for Improving MPEF Properties. *Angew. Chem.* **2019**, *131*, 14517−14523.
(38) Liu, N.; Chen, Z.; Fan, W.; Su, J.; Lin, T.; Xiao, S.; Meng, J.; He, J.; Vittal, J. J.; Jiang, J. Highly Efficient Multiphoton Absorption of Zinc-AIEgen Metal−Organic Frameworks. *Angew. Chem., Int. Ed.* **2022**, *61*, e202115205.

https://doi.org/10.1021/acs.chemmater.2c01525
Chem. Mater. 2022, 34, 7402−7411

A.1. Supporting information

Supporting information (SI) of Weishäupl, S.J.[†]; Cui, Y.[†]; Deger, S.N.; Syed, H.; Ovsianikov, A.; Hauer, J.; Pöthig, A.; Fischer, R.A. Coordination polymers based on carbazole-derived chromophore linkers for optimized multiphoton absorption: a structural and photophysical study. *Chemistry of Materials*, **34**(16):7402–7411, **2022**. The SI is available free of charge; thus, no reprint permission is necessary.

Supporting Information

For

Coordination Polymers Based on Carbazole-Derived Chromophore Linkers for Optimized Multiphoton Absorption: A Structural and Photophysical Study

Sebastian J. Weishäupl [1†], Yang Cui [2,3†], Simon Deger [1], Hamad Syed [4], Alexander Pöthig [1], Aleksandr Ovsianikov [4], Jürgen Hauer[2] and Roland A. Fischer [1*]*

[1] Chair of Inorganic and Metal−Organic Chemistry, Department of Chemistry & Catalysis Research Center, Technical University of Munich, Lichtenbergstraße 4, 85748 Garching, Germany;

[2] Professorship for Dynamic Spectroscopy, Technical University of Munich, Lichtenbergstraße 4, 85748 Garching, Germany;

[3] Department of Physics, Technical University of Munich, James-Franck-Straße 1, 85748 Garching, Germany;

[4] 3D Printing and Biofabrication Group, Institute of Materials Science and Technology, Technische Universität Wien (TU Wien), Getreidemarkt 9/308, Vienna 1060, Austria;

[†] These authors contributed equally to this work.

* Correspondence: roland.fischer@tum.de (RAF), alexander.poethig@tum.de (AP), juergen.hauer@tum.de (JH)

1. Synthetic procedures of the carbazole precursor

All reactions were carried out following our 2020 already published synthesis procedure.

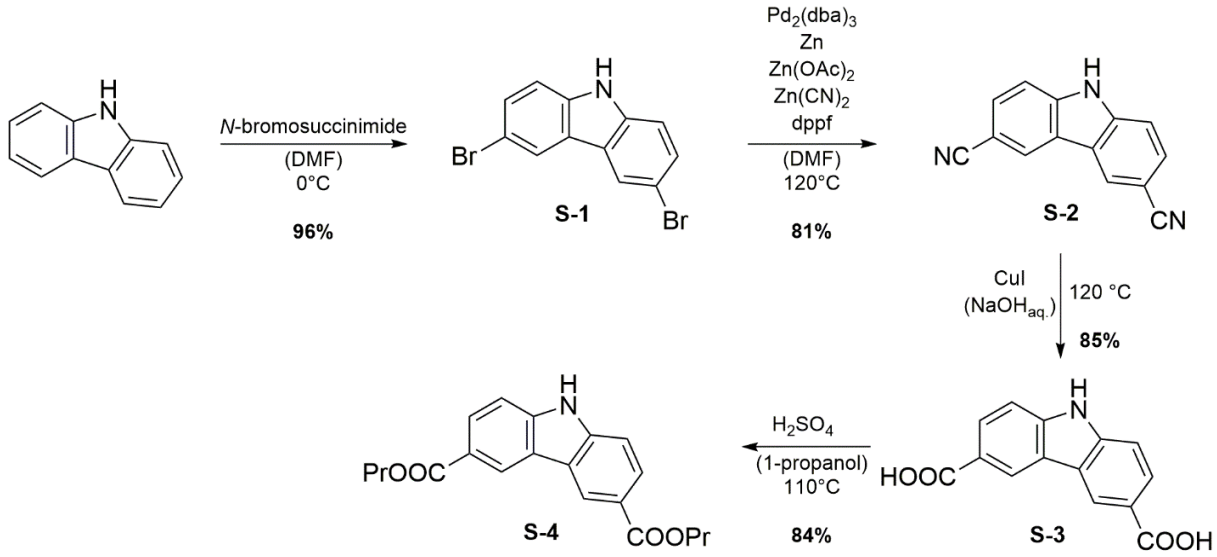

Fig. S1: Synthesis route towards the carbazole precursor.

3,6-Dibromocarbazole (**S-1)**: A solution of N-bromosuccinimide (22.35 g, 125 mmol) in 50 mL DMF was slowly added through a syringe pump to a stirring solution of carbazole (10 g, 59.80 mmol) in 20 mL DMF in an ice bath. After 24 hours of reaction time, the mixture was poured into 600 mL ice water and then filtered through a suction filter to give a dark grey powder. The crude product was recrystallized with Ethanol to give a grey powder of 3,6-Dibromocarbazole (18,68 g, 96%). ^{1}H-NMR (400 MHz, 298K, DMSO-d_6) δ (ppm) = 7.47 (d, J = 8.6 Hz, 2H), 7.53 (dd, J = 2.0, 8.6 Hz, 2H), 8.43 (d, J = 1.9, 2H), 11.59 (s, 1H, N-H). ^{13}C-NMR (101 MHz, 298K, DMSO-d_6) δ (ppm) = 110.96, 113.18, 123.35, 123.29, 128.70, 138.78.

Carbazole-3,6-Dicarbonitrile (**S-2**): 3,6-Dibromocarbazole (9.75 g, 30.0 mmol) and dppf (100 mg, 0.18 mmol) were added to a 100 mL Schlenk flask and solved in 30 mL DMF and 0.3 mL water. The suspension was degassed via bubbling argon for 1 hour through the mixture. Subsequently, $Zn(CN)_2$ (4.21 g, 36 mmol), zinc powder (78 mg, 1.2 mmol), $Zn(OAc)_2 \cdot 2\ H_2O$ (0.26 g, 1.2 mmol) and $Pd_2(dba)_3 \cdot$ dba (69.5 mg, 0,06 mmol) were added under a positive pressure of argon. This mixture was heated to 110 °C for 2 days. The

suspension was subsequently cooled and then poured into a 100 mL mixture of $H_2O/NH_4Cl/NH_3$ (5/4/1) and filtered through a suction filter. The filter cake was washed with the same volume of the above mixture, toluene (3 x 30 mL) and MeOH (3 x 30 mL) to give a grey solid. The crude product was recrystallized with DMF to give a white solid (5.2 g, 81%). ^{1}H-NMR (400 MHz, 298K, DMSO-d_6) δ (ppm) = 7.72 (d, J = 8.5 Hz, 2H), 7.85 (d, J = 9.9 Hz, 2H), 8.80 (s, 2H), 12.38 (s, 1H, N-H). ^{13}C-NMR (101 MHz, 298K, DMSO-d_6) δ (ppm) = 101.74, 112.84, 120.10, 121.85, 126.8, 129.93, 142.32.

Carbazole-3,6-dicarboxylic acid (**S-3**): Carbazole-3,6-Dicarbonitrile (4.2 g, 19.3 mmol) was suspended in an aqueous NaOH solution (12.45 g in 150 mL). To this solution CuI (37,5 mg, 0.195 mmol) was added and then quickly heated to 125 °C for 2 days, until the starting material was dissolved. Afterwards active carbon was added, and the mixture was again heated to 125 °C for 2 hours. After cooling, the suspension was filtered through celite, which was pre-washed with aq. NaOH-solution. The filtrate was acidified with 6M HCl-solution to give a white precipitate. The precipitate was filtered, washed with water and then dried to give a withe solid (4.0 g, 85%). ^{1}H-NMR (400 MHz, 298K, $CDCl_3$) δ (ppm) = 7.60 (d, J = 8.5 Hz, 2H), 8.06 (d, J = 8.4 Hz, 2H), 8.85 (s, 2H), 12.04 (s, 1H, N-H), 12.69 (bs, 2H, COOH). ^{13}C-NMR (101 MHz, 298K, DMSO-d6) δ (ppm) = 111.13, 122.00, 122.27, 122.79, 127.65, 143.12, 167.94.

Dipropyl-carbazole-3,6-dicarboxylate (**S-4**): Carbazole-3,6-dicarboxylic acid 4 (4.0 g, 15.64 mmol) was suspended in 100 mL 1-propanol. To this suspension, conc. sulfuric acid (2 mL) was added and then refluxed at 110 °C for 24 hours. After cooling, the suspension was concentrated on a rotary evaporator and extracted with 200 mL dichloromethane. The organic layer was washed with aq. NaHCO3 (150 mL) and then dried with MgSO4. The solvent was evaporated to give a yellowish solid (4.5 g, 84%). ^{1}H NMR (400 MHz, 298K, CDCl3) δ (ppm) = 1.09 (t, J = 7.4 Hz, 6H), 1.87 (h, J = 7.2 Hz, 4H), 4.36 (t, J = 6.7 Hz, 4H), 7.47 (d, J = 8.5 Hz, 2H), 8.18 (dd, J = 1.5 Hz, 2H), 8.86 (s, 2H). ^{13}C-NMR (101 MHz, 298K, $CDCl_3$) δ (ppm) = 10.77, 22.40, 66.67, 110.64, 122.89, 123.19, 128.28, 142.85, 167.35.

2. NMR spectroscopy

2.1 Pr_4sbcd

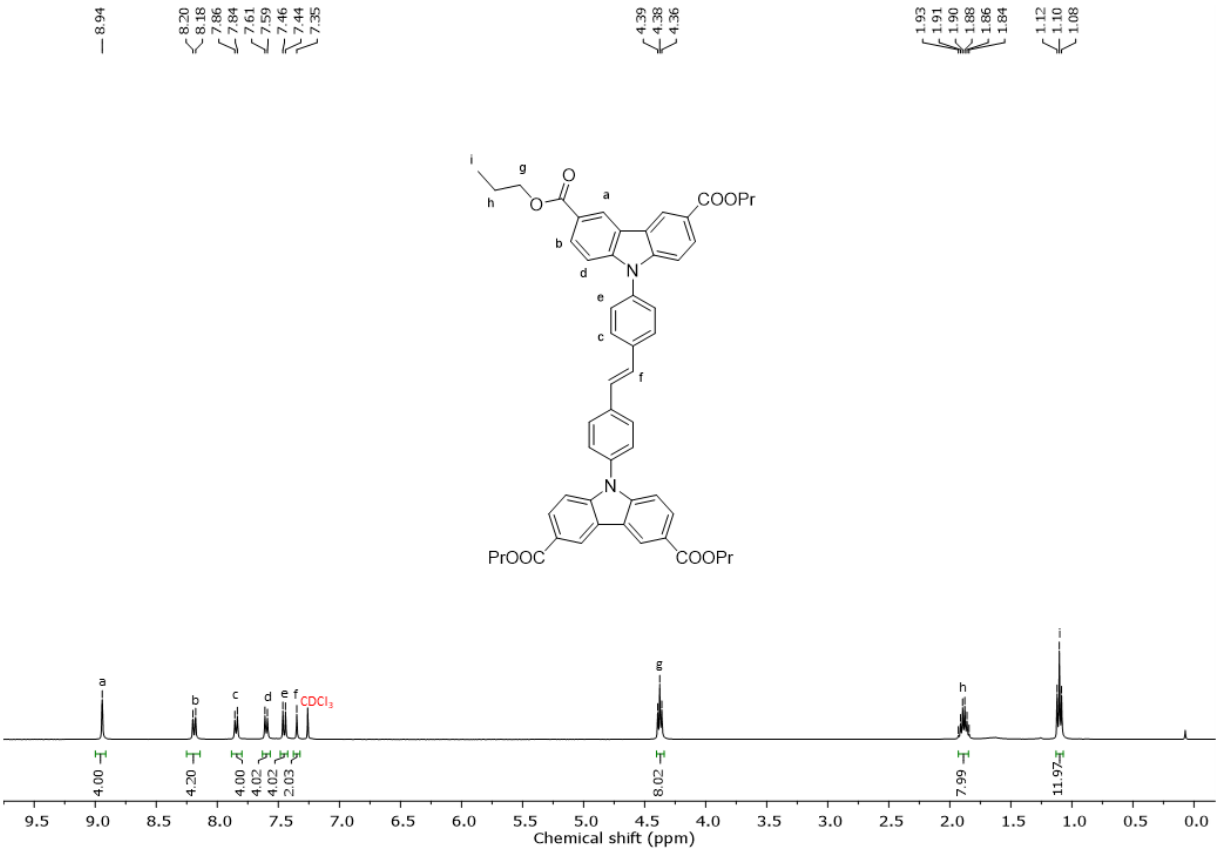

Fig. S2: ^{1}H-NMR of Pr_4sbcd with the respective chemical shifts in $CDCl_3$.

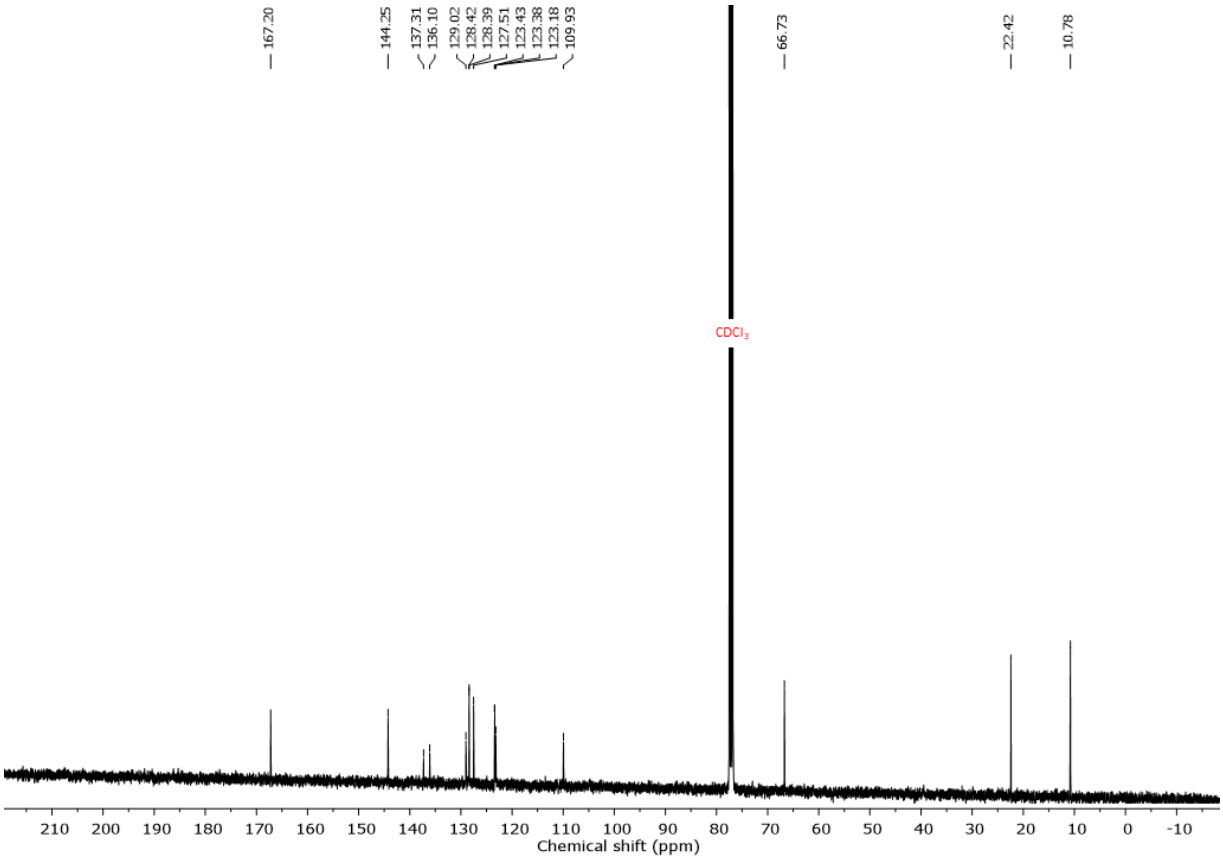

Fig. S3: ^{13}C-NMR of Pr_4sbcd with the respective chemical shifts in $CDCl_3$.

2.2 H_4sbcd

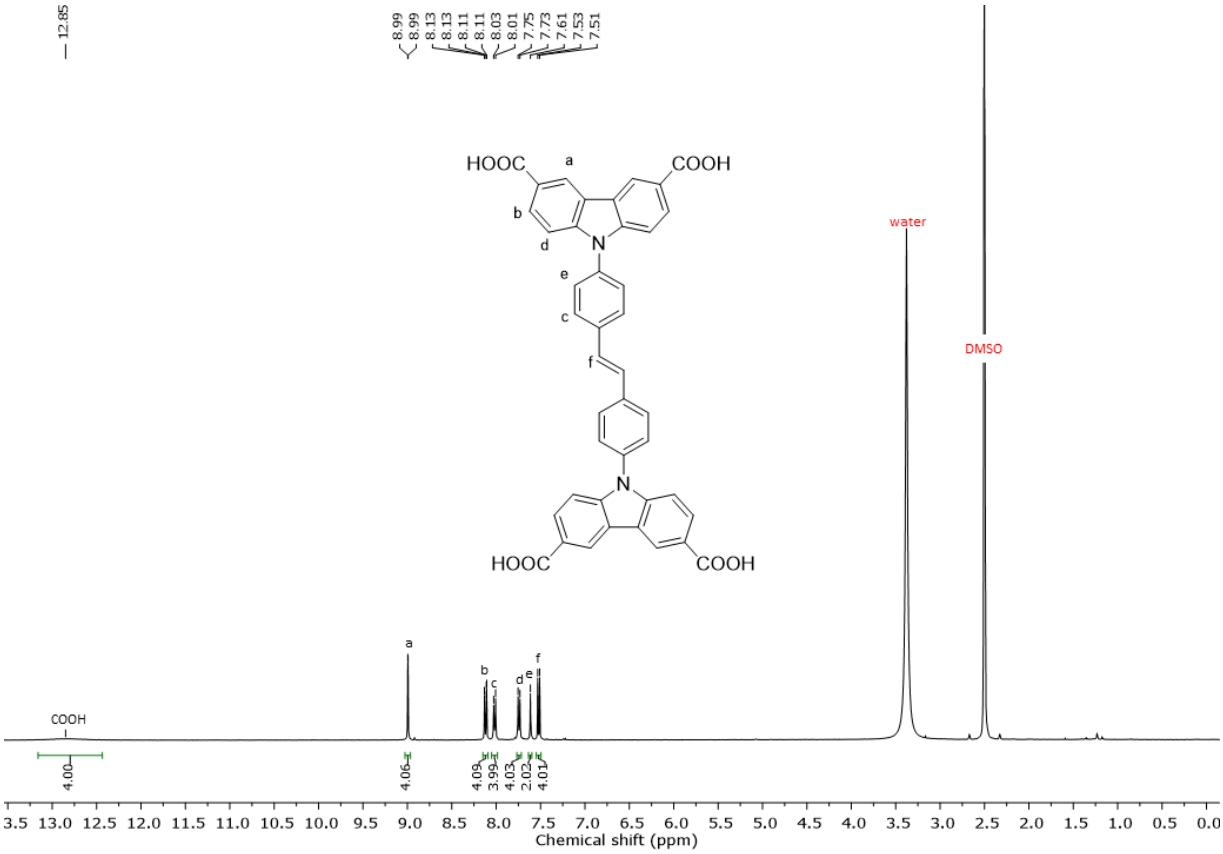

Fig. S4: ^{1}H-NMR of H_4sbcd with the respective chemical shifts in DMSO-d_6.

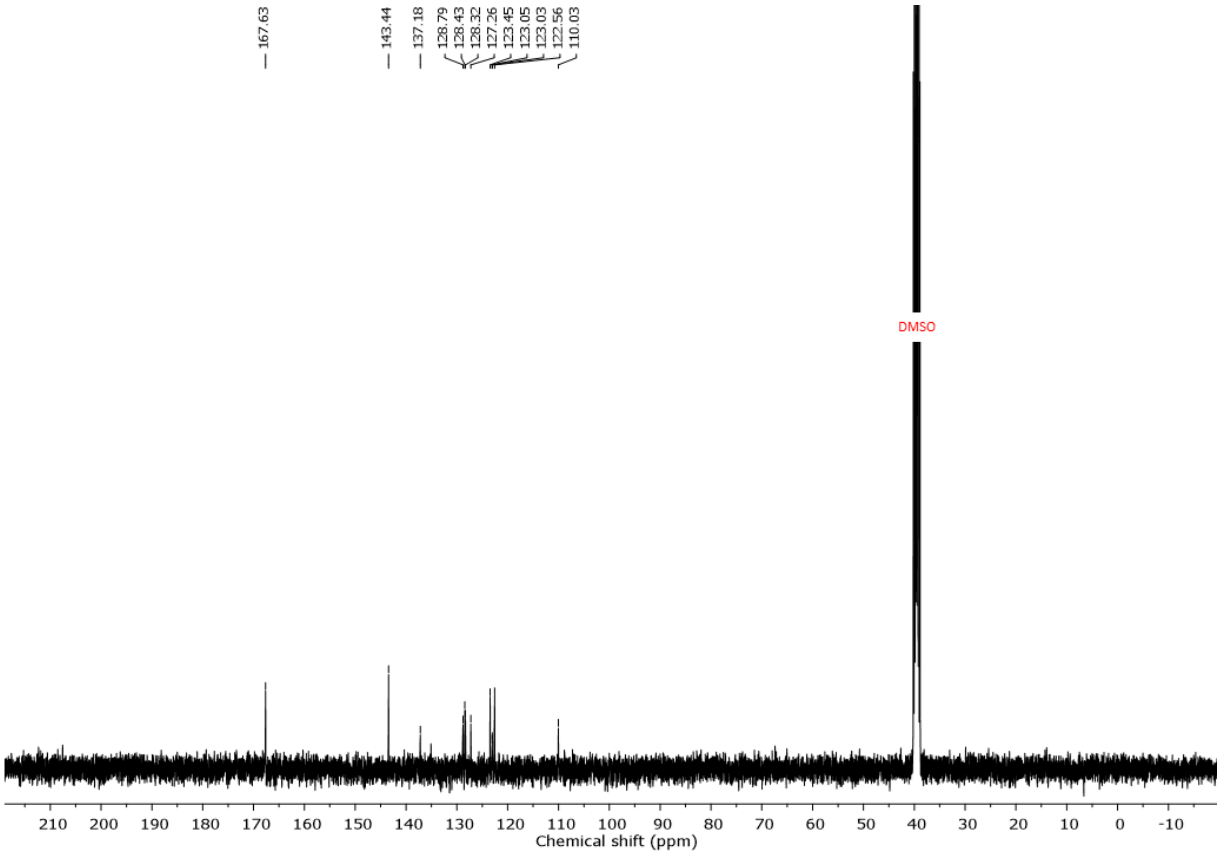

Fig. S5: ^{13}C-NMR of H_4sbcd with the respective chemical shifts in DMSO-d_6.

2.3 Pr_4fbcd

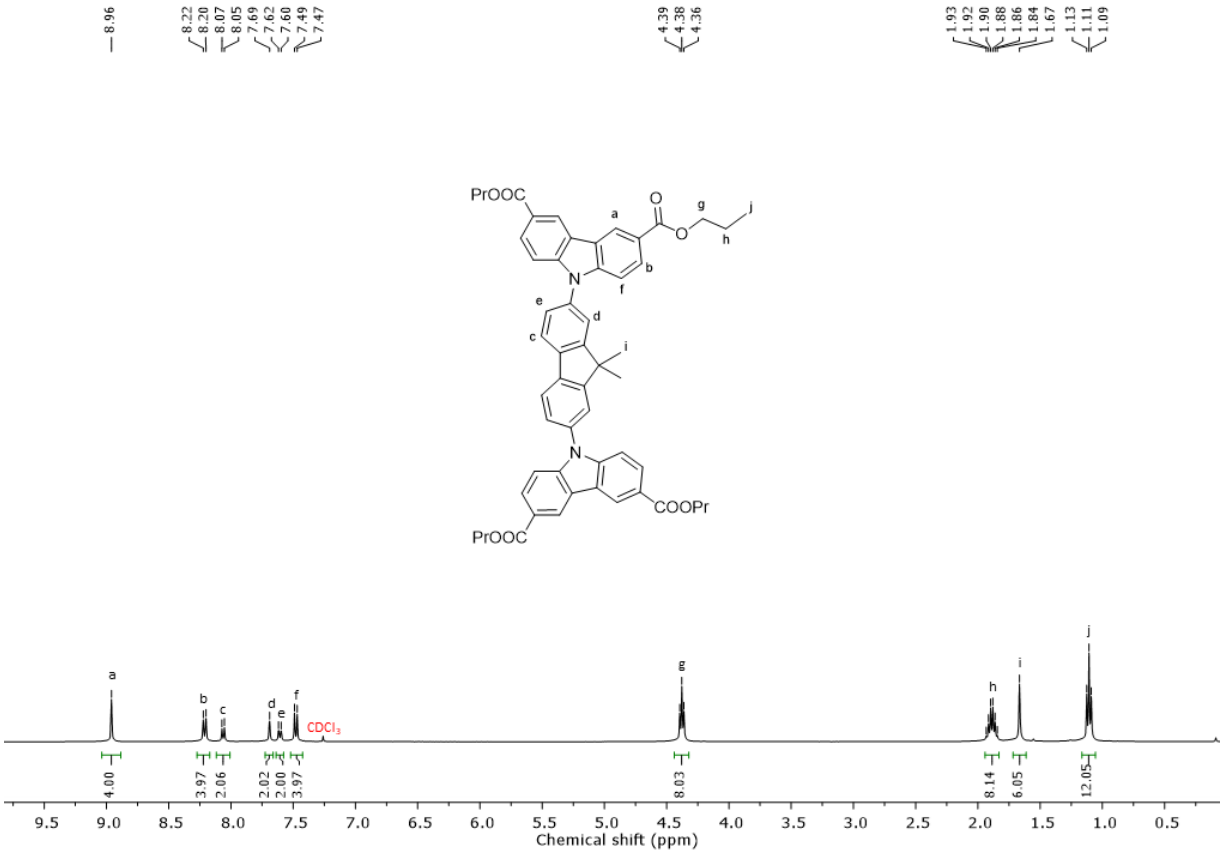

Fig. S6: ^{1}H-NMR of Pr_4fbcd with the respective chemical shifts in $CDCl_3$.

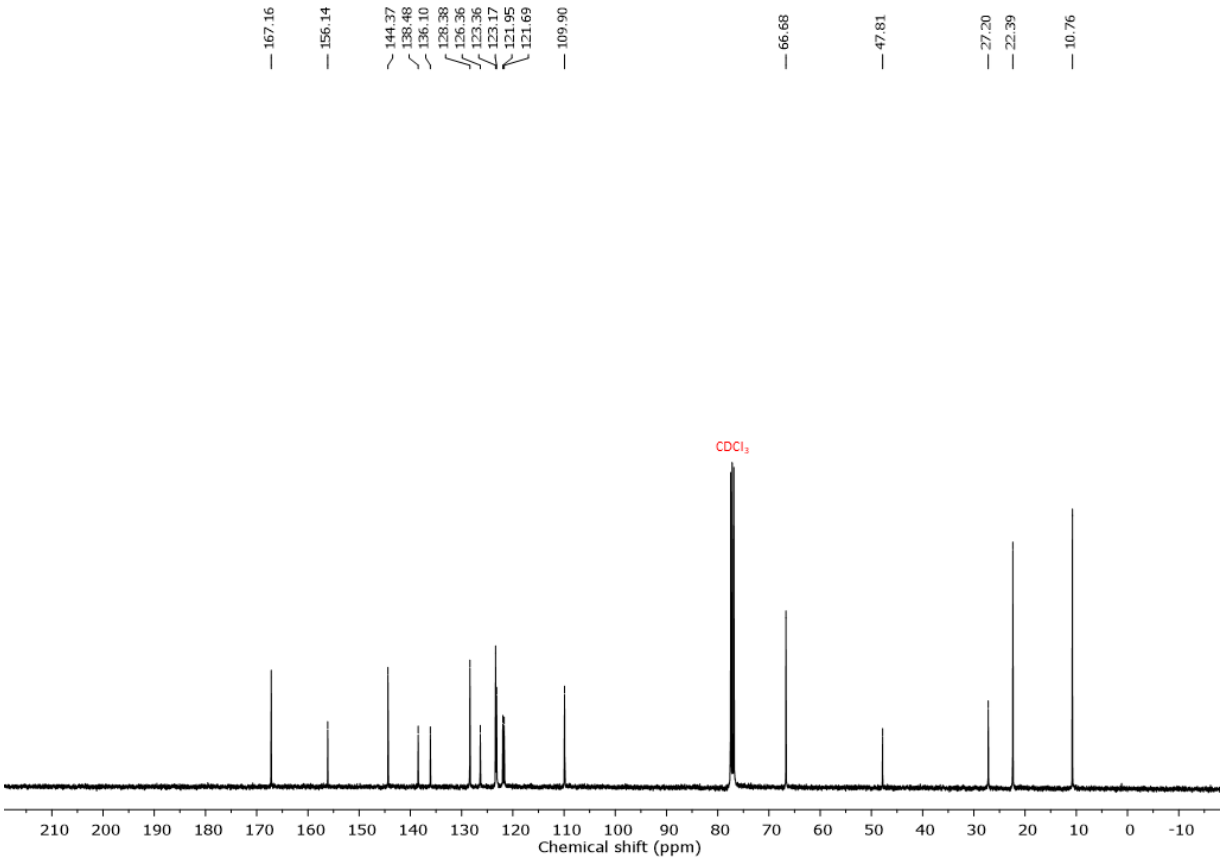

Fig. S7: ^{13}C-NMR of Pr_4fbcd with the respective chemical shifts in $CDCl_3$.

2.4 H_4fbcd

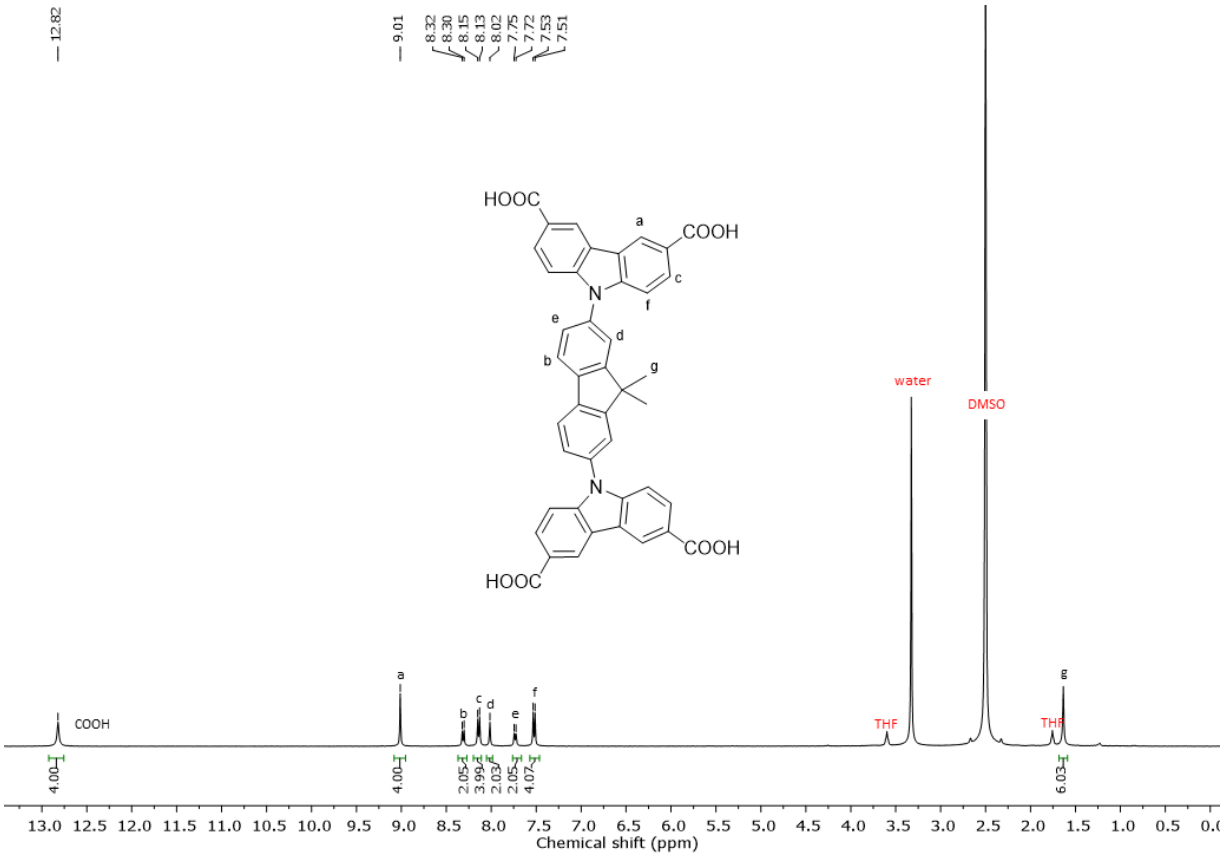

Fig. S8: ^{1}H-NMR of H_4fbcd with the respective chemical shifts in DMSO-d_6.

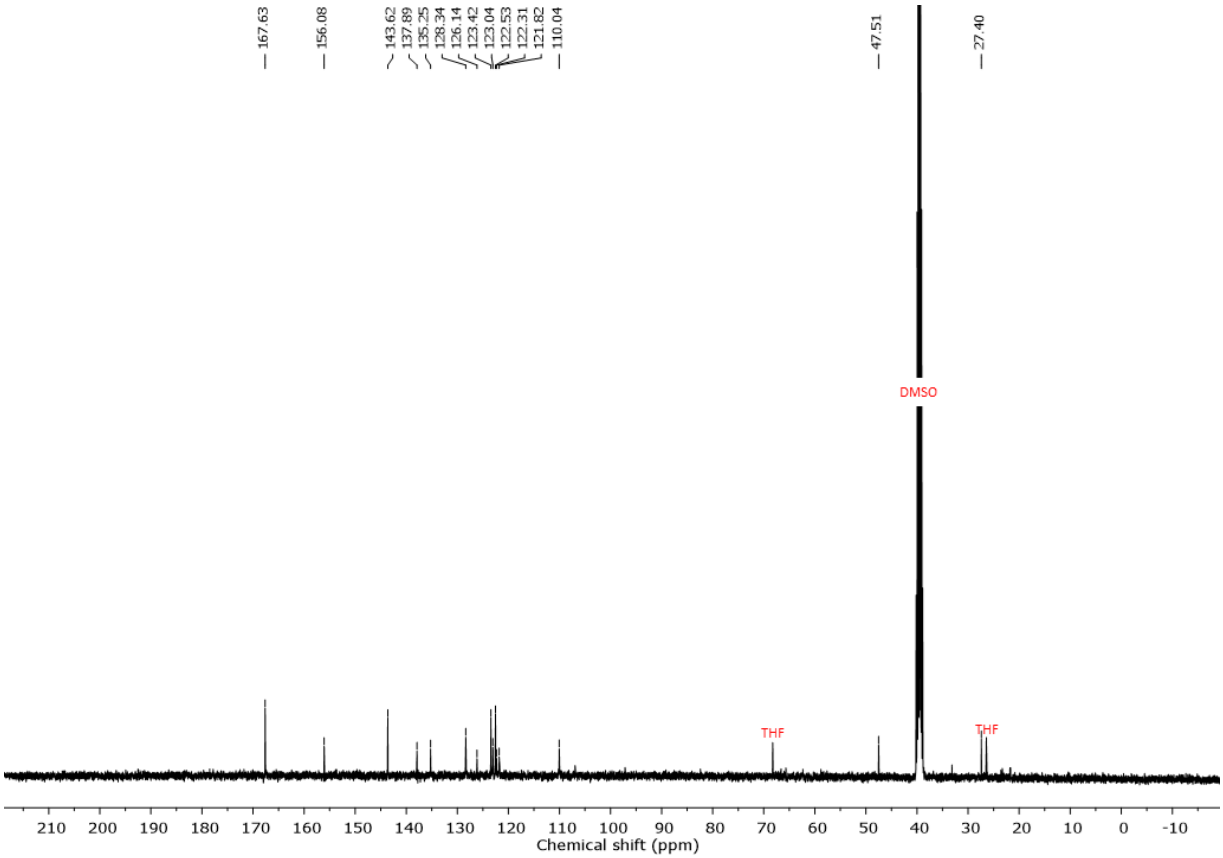

Fig. S9: ^{13}C-NMR of H_4fbcd with the respective chemical shifts in DMSO-d_6.

3. IR analysis of the coordination polymers and their linkers

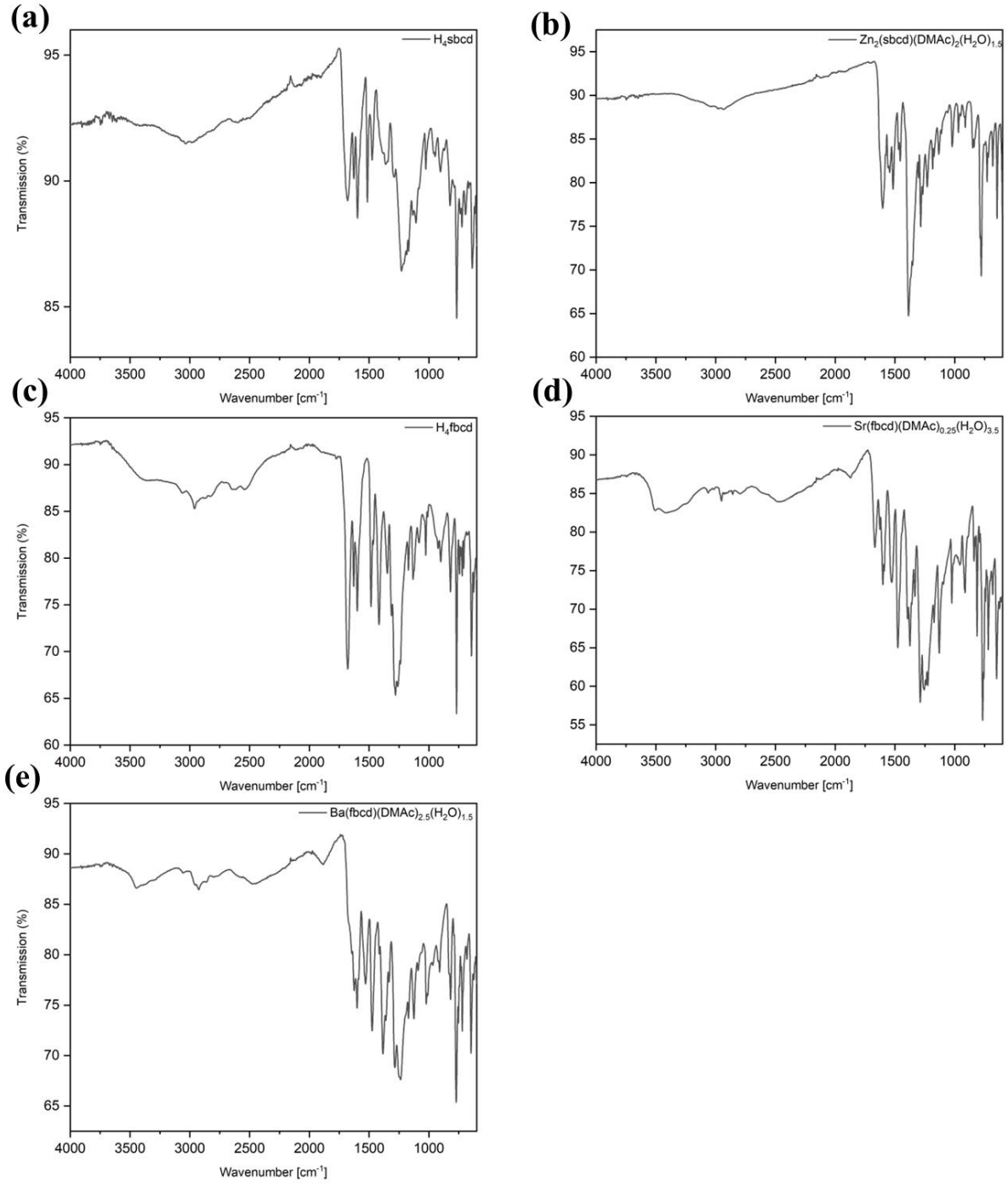

Fig. S10: IR spectrum of (a) H_4fbcd, (b) $Zn_2(sbcd)(DMAc)_2(H_2O)_{1.5}$, (c) H_4fbcd, (d) $Sr(fbcd)(DMAc)_{0.25}(H_2O)_{3.5}$ and (e) $Ba(fbcd)(DMAc)_{2.5}(H_2O)_{1.5}$.

4. Thermogravimetric analysis (TGA) of the coordination polymers

The TGA was carried out with a TGA/DSC 3+ STAR system from METTLER TOLEDO, to which a gas analysis system from THERMOStar was connected. The sample was filled into a crucible, which was tared beforehand, and the sample was weighed in the device.

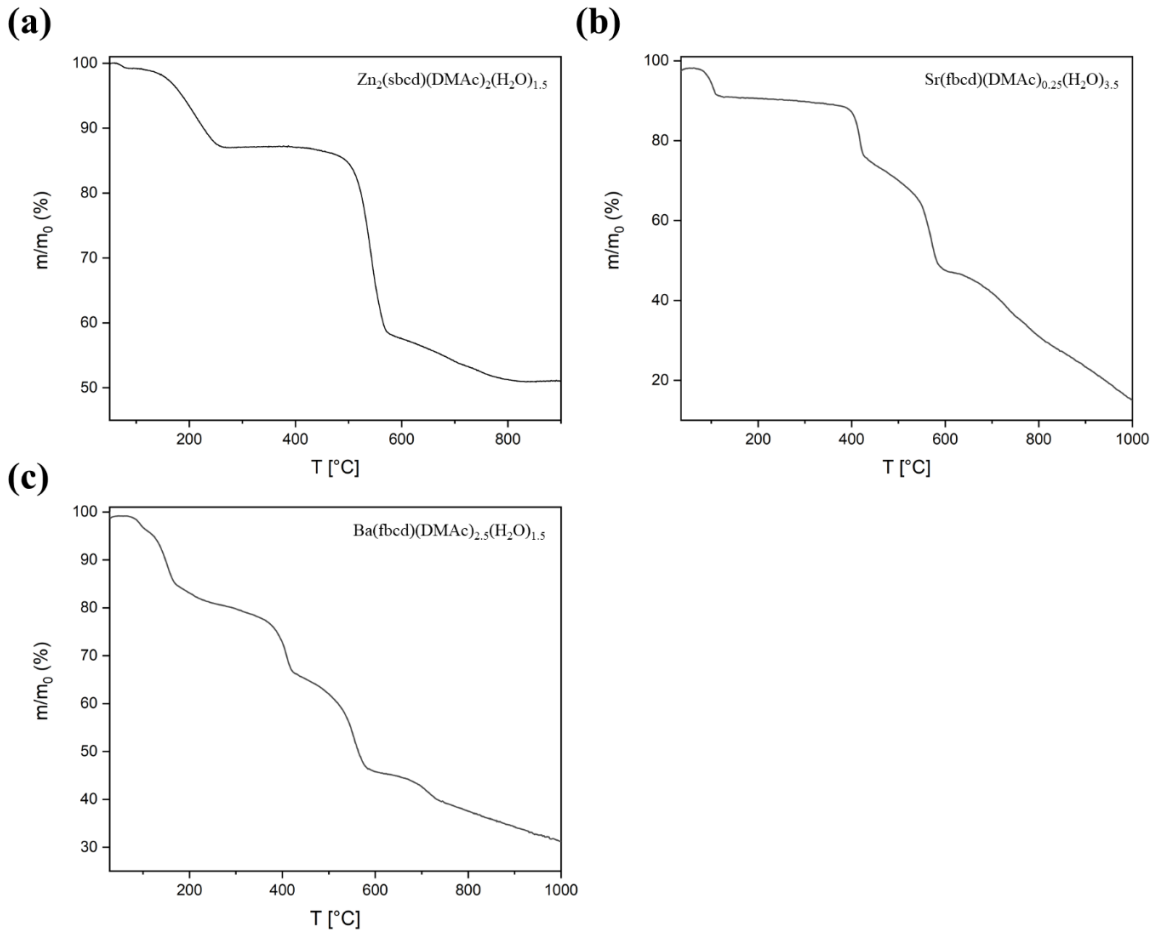

Fig. S11: TGA of the three coordination polymers (a) $Zn_2(sbcd)(DMAc)_2(H_2O)_{1.5}$, (b) $Sr(fbcd)(DMAc)_{0.25}(H_2O)_{3.5}$ and (c) $Ba(fbcd)(DMAc)_{2.5}(H_2O)_{1.5}$ with a heating rate of 10 K/min.

5. Z-scan data processing

The Z-scan setup is based on a high power femtosecond tunable oscillator (MaiTai DeepSee, Spectra Physics, Santa Clara, USA) with wavelength ranging from 690 to 1040 nm at a repetition rate of 81 MHz. The estimated pulse duration of the laser was 70 fs at 800 nm (central wavelength) and increased to 113 fs at lower wavelengths. The average power of the pulse (c.a. 70 fs) was about 3 W. The combination of Brewster-angle polarizer and half-wave plate were employed to tune the input power to the sample. The laser was directed to the custom-built mechanical chopper (142 Hz rotation frequency gives 78 μs on-time) and it decreases the exposure time of the sample to eliminate thermal effects. The laser pulses were focused onto the coordination polymers film samples by an achromatic doublet lens with focal length of 200 mm (AC254-200-B, Thorlabs). The sample was fixed on the motorized translation stage (LCS16-025-2(4)5, SMAC) and moved along the beam propagation direction *z* through monitoring the transmitted light from the sample by a photodiode (PDA100A-EC, Thorlabs) along with an oscilloscope (DS4024, Rigol). Moreover, a reference photodiode was used to compensate the signal fluctuations.[1] Nonlinear absorption studies were carried out by open-aperture Z-scan at various wavelengths from 700 nm to 950 nm with a spectral increment of 10 nm to comprehensively figure out the spectral dependent nonlinear absorption.

The measured Z-scan trace was fitted using the following equation

$$T_{\text{norm.}}(z) = 1 - \frac{1}{2\sqrt{2}} \frac{\beta I_0 L_{\text{eff}}}{1 + (\frac{z}{z_{\text{R}}})^2} \tag{1}$$

where

$$L_{\text{eff}} = \frac{1 - e^{-\alpha d}}{\alpha} \tag{2}$$

and

$$I_0 = 4\sqrt{\frac{\ln 2}{\pi}} \frac{P_{\text{avg}}}{\text{M}^2 \lambda z_{\text{R}} R \tau} \tag{3}$$

Two-photon absorption (2PA) coefficient β can be then extracted by fitting Equation (1), and, 2PA cross section $\sigma^{(2)}$ is calculated by

$$\sigma^{(2)}(\lambda) = \frac{hc}{\lambda}\frac{\beta(\lambda)}{N_{\mathrm{A}}\rho \times 10^{-3}}\ (\mathrm{cm}^4\ \mathrm{s\ photon}^{-1}\ \mathrm{molecule}^{-1}) \quad (4)$$

Related parameters are listed below:

$T_{\mathrm{norm.}}(z)$: normalized transmittance in terms of sample positon z

β: two-photon absorption coefficient

I_0: on-axis intensity of the laser

L_{eff}: effective optical path

z_{R}: Rayleigh length of the focusing beam

α: linear (one-photon) absorption coefficient

d: sample thickness

P_{avg}: average power of the laser

M^2: beam quality factor

λ: excitation wavelength

R: repetition rate of the pulsed laser

τ: laser pulse duration

h: Planck constant

c: speed of light in vacuum

N_{A}: Avogadro constant

ρ: sample concentration

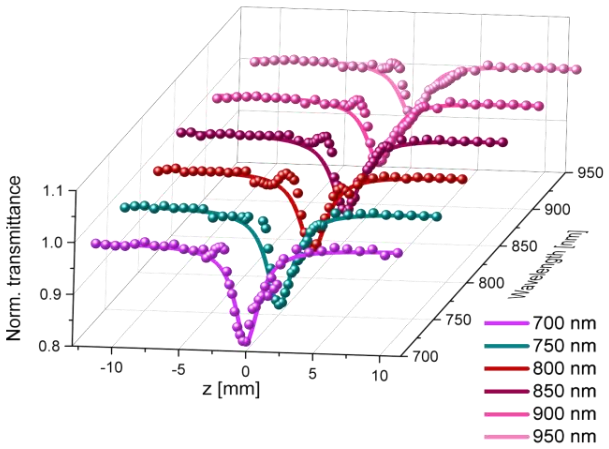

Fig. S12: Z-scan traces and data fitting for $Ba(fbcd)(DMAc)_{2.5}(H_2O)_{1.5}$ at different excitation wavelengths.

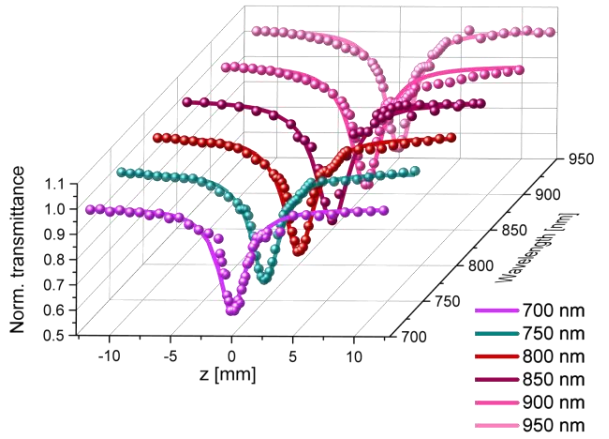

Fig. S13: Z-scan traces and data fitting for $Sr(fbcd)(DMAc)_{0.25}(H_2O)_{3.5}$ at different excitation wavelengths.

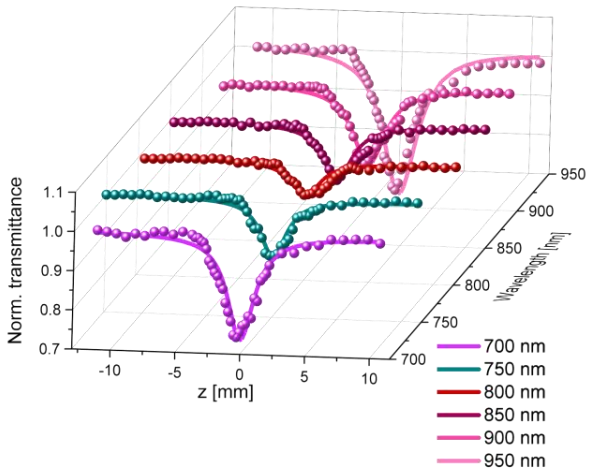

Fig. S14: Z-scan traces and data fitting for $Zn_2(sbcd)(DMAc)_2(H_2O)_{1.5}$ at different excitation wavelengths.

Table S1: Two-photon absorption coefficients $\beta(\lambda)$ in the unit of cm/GW and two-photon absorption cross-section values $\sigma^{(2)}(\lambda)$ in the unit of GM at different excitation wavelengths are tabulated. On-axis laser intensity for each samples are: $Zn_2(sbcd)(DMAc)_2(H_2O)_{1.5}$, 20–28 GW/cm^2; $Ba(fbcd)(DMAc)_{2.5}(H_2O)_{1.5}$, 28–39 GW/cm^2; $Sr(fbcd)(DMAc)_{0.25}(H_2O)_{3.5}$, 13–21 GW/cm^2..

Wavelength [nm]	$Zn_2(sbcd)(DMAc)_2(H_2O)_{1.5}$		$Ba(fbcd)(DMAc)_{2.5}(H_2O)_{1.5}$		$Sr(fbcd)(DMAc)_{0.25}(H_2O)_{3.5}$	
	β	$\sigma^{(2)}$	β	$\sigma^{(2)}$	β	$\sigma^{(2)}$
700	11.4	13922.80	6.2	10360.56	31	26885.96
710	6.7	8066.91	4.9	8073.24	34.4	29415.20
720	6.4	7599.59	5.3	8609.86	30	25297.51
730	5	5855.89	6.5	10415.49	32	26614.04
740	5.7	6585.69	4.3	6797.18	25.4	20839.91
750	5.66	2918.17	4	6238.03	25.6	20723.68
760	2.86	3216.68	6.7	10312.68	28.4	22687.87
770	3.4	3774.58	3.3	5012.68	29	22865.50
780	3.3	3617.09	3.3	4949.30	30	23347.95
790	3.58	3874.42	3.34	4946.48	30.4	23362.57
800	2	2136.90	2.8	4094.37	33.6	25497.08
810	2.1	2216.16	2.9	4187.32	35	26235.38
820	2.34	2439.73	3.1	4422.54	36.6	27097.95
830	2.66	2740.09	3.3	4650.70	38.2	27938.60
840	3.3	3358.72	3.2	4456.34	35	25299.71

850	3.9	3922.80	3	4128.17	42	30000
860	4.62	4592.90	2.9	3945.07	47	33179.82
870	5.5	5405.04	2.86	3845.49	47.8	33355.26
880	5.5	5343.28	3.1	4121.13	45	31045.32
890	5.4	5186.82	3	3942.25	46	31381.58
900	6.7	6364.38	2.7	3509.44	47	31703.22
910	8.8	8267.63	2.7	3470.85	47.6	31754.36
920	12.8	11888.83	2.6	3305.63	48.8	32200.29
930	14.4	13237.26	2.64	3319.72	49.4	32251.46
940	15.5	14097.79	2.72	3384.51	49.4	31907.89
950	17.6	15838.39	2.48	3053.52	50	31951.75

6. Single crystal X-ray diffraction

X-ray intensity data of the compound was collected at 100K using a Bruker D8 Venture diffractometer equipped with a Helios optic monochromator, a Photon 100 CMOS detector and a Mo IMS microsource (Mo-K_α radiation). The raw area detector data frames were reduced and corrected for absorption effects using the SAINT and SADABS programs with multi-scan absorption correction. Final unit cell parameters were determined by fast fourier transform refinement of the respective independent reflections taken from the data sets. The structure was solved by autostructure with SHELXT. Difference Fourier calculations and full-matrix least-squares refinements against F^2 were performed by SHELXL-2014/7 (Sheldrick, 2014). All non-hydrogen atoms were refined with anisotropic displacement parameters. Hydrogen atoms were refined by a mixture of independent and constrained refinement.

6.1 Single-crystal report of $Zn_2(sbcd)(DMAc)_2(H_2O)_{1.5}$ (CCDC deposition number:)

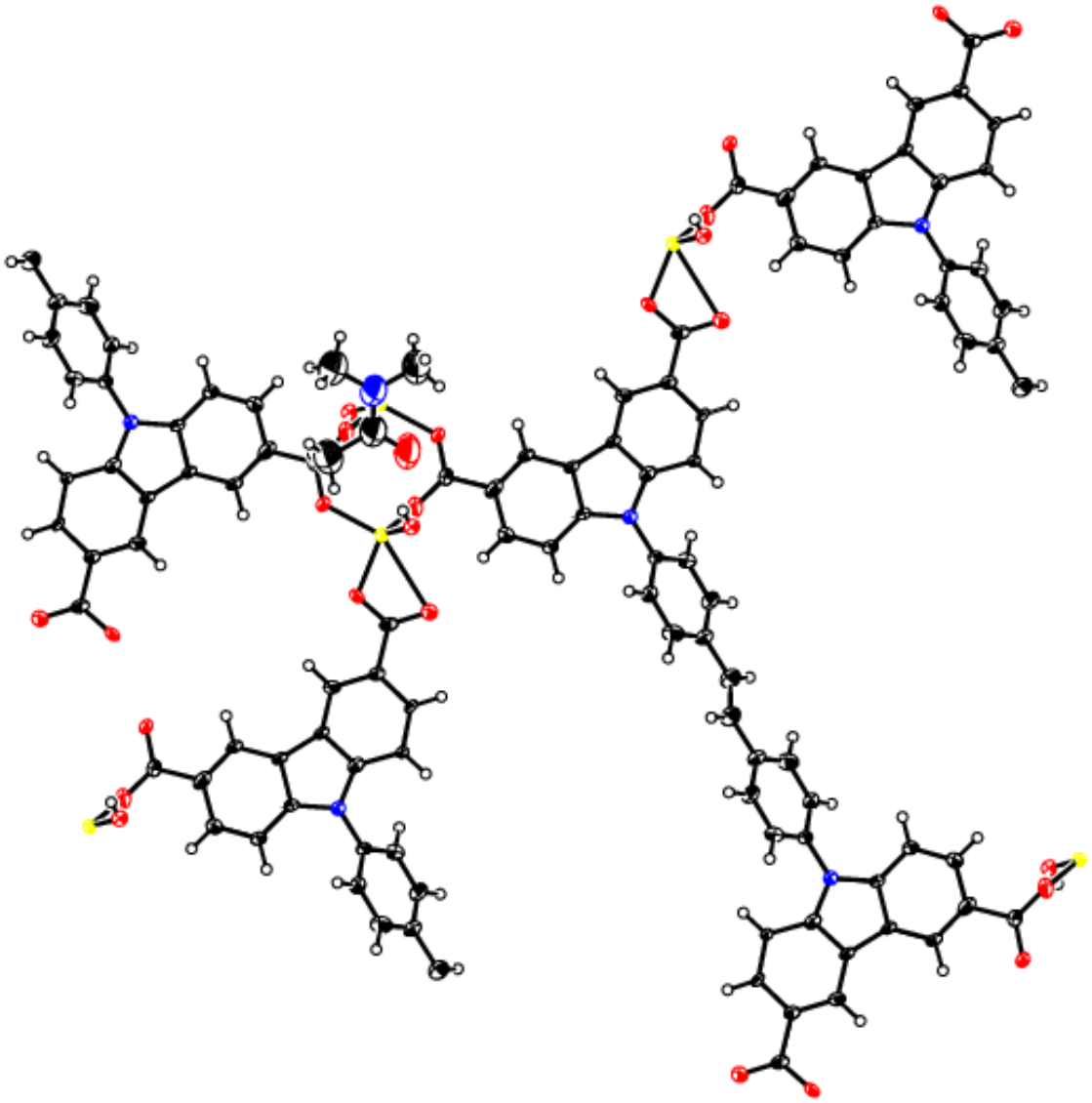

Fig. S15: ORTEP representation of the single-crystal structure of $Zn_2(sbcd)(DMAc)_2(H_2O)_{1.5}$ with thermal ellipsoids shown at the 50% probability level.

Crystal data	znsbcd_0m
Chemical formula	$C_{21}H_{11}NO_5Zn \cdot C_4H_9NO$
M_r	509.82

Crystal system, space group	Triclinic, *P* -1
Temperature (K)	103
a, *b*, *c* (Å)	9.256 (3), 11.735 (4), 12.319 (4)
α, β, γ (°)	73.267 (10), 78.637 (8), 68.362 (10)
V (Å^3)	1184.9 (7)
Z	2
Radiation type	Mo *K*α
μ (mm^{-1})	1.08
Crystal size (mm)	0.29 × 0.12 × 0.07
Data collection	
Diffractometer	Bruker Photon CMOS
Absorption correction	Multi-scan *SADABS* 2016/2, Bruker, 2016
T_{min}, T_{max}	0.550, 0.745
No. of measured, independent and observed [$I > 2\sigma(I)$] reflections	13863, 4247, 2440
R_{int}	0.116
$(\sin \theta/\lambda)_{max}$ (Å^{-1})	0.602
Refinement	
$R[F^2 > 2\sigma(F^2)]$, $wR(F^2)$, S	0.128, 0.349, 1.06
No. of reflections	4247
No. of parameters	315
No. of restraints	36
H-atom treatment	H atoms treated by a mixture of independent and constrained refinement $W = 1/[\Sigma^2(FO^2) + (0.1315P)^2 + 18.4592P]$ WHERE $P = (FO^2 + 2FC^2)/3$
$\Delta\rho_{max}$, $\Delta\rho_{min}$ (e Å^{-3})	1.71, −0.94

6.2 Single-crystal report of $Sr(fbcd)(DMAc)_{0.25}(H_2O)_{3.5}$ (CCDC deposition number:)

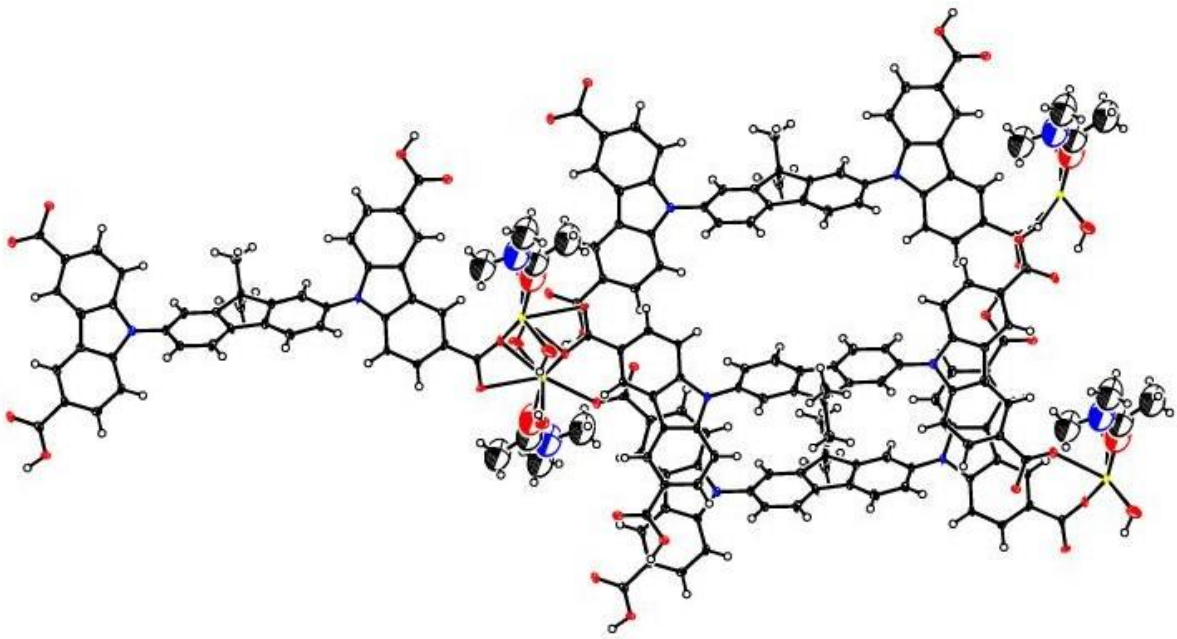

Fig. S16: ORTEP representation of the single-crystal structure of $Sr(fbcd)(DMAc)_{0.25}(H_2O)_{3.5}$ with thermal ellipsoids shown at the 50% probability level.

Crystal data	weise43_0ma_sq
Chemical formula	$C_{43}H_{26}N_2O_8Sr \cdot 2(OH) \cdot (C_4H_9NO)$
M_r	907.42
Crystal system, space group	Triclinic, *P* -1
Temperature (K)	100
a, *b*, *c* (Å)	10.076 (3), 12.140 (3), 23.401 (6)
α, β, γ (°)	93.793 (7), 90.197 (8), 93.276 (8)
V (Å^3)	2851.5 (13)
Z	2
Radiation type	Mo *K*α
μ (mm^{-1})	1.00

Crystal size (mm)	0.25 × 0.01 × 0.01
Data collection	
Diffractometer	Bruker Photon CMOS
Absorption correction	Multi-scan *SADABS* 2016/2, Bruker, 2016
T_{min}, T_{max}	0.660, 0.739
No. of measured, independent and observed [$I > 2\sigma(I)$] reflections	122464, 11211, 8779
R_{int}	0.112
$(\sin \theta/\lambda)_{max}$ (Å^{-1})	0.617
Refinement	
$R[F^2 > 2\sigma(F^2)]$, $wR(F^2)$, S	0.116, 0.324, 1.02
No. of reflections	11211
No. of parameters	572
No. of restraints	79
H-atom treatment	H atoms treated by a mixture of independent and constrained refinement
	W = 1/[$\Sigma^2(FO^2)$ + (0.172P)^2 + 35.4396P] WHERE P = (FO^2 + 2FC^2)/3
$\Delta\rho_{max}$, $\Delta\rho_{min}$ (e Å^{-3})	7.39, −1.36

6.3 Single-crystal report of Ba(fbcd)(DMAc)$_{2.5}$(H_2O)$_{1.5}$ (CCDC deposition number:)

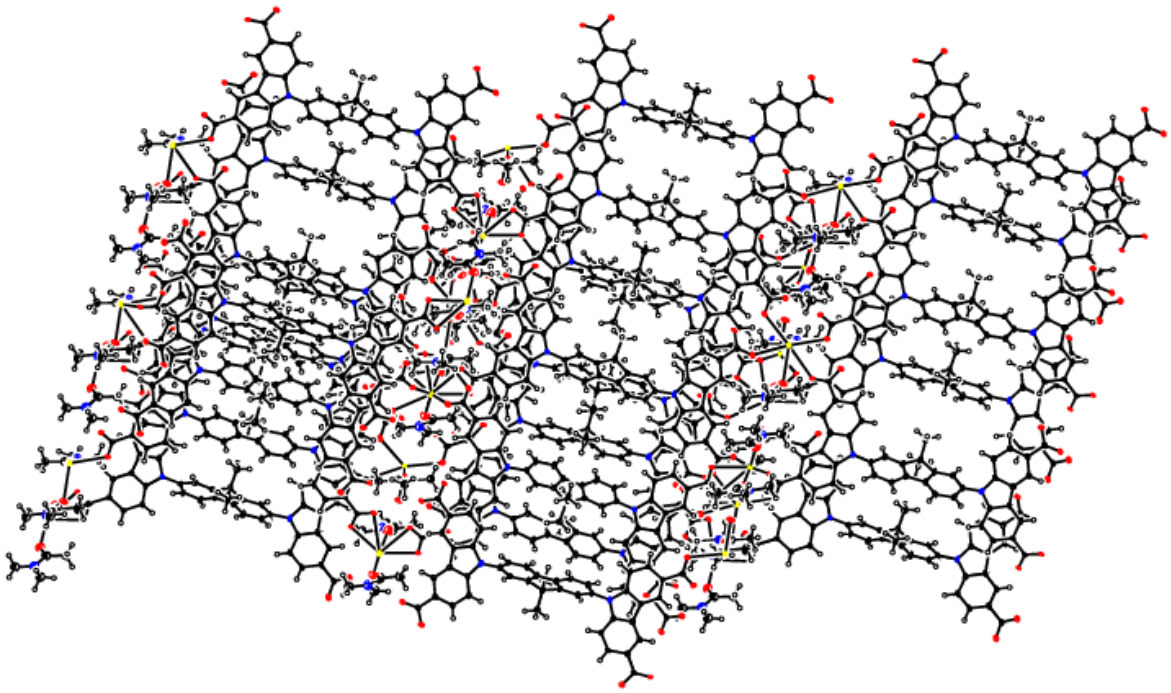

Fig. S17: ORTEP representation of the single-crystal structure of Ba(fbcd)(DMAc)$_{2.5}$(H$_2$O)$_{1.5}$ with thermal ellipsoids shown at the 50% probability level.

Crystal data	weise40_m_0m_sq
Chemical formula	$C_{86}H_{48}Ba_2N_4O_{16}\cdot3(C_4H_9NO)\cdot(H_2O)$
M_r	1963.33
Crystal system, space group	Monoclinic, *P* $2_1/n$
Temperature (K)	100
a, *b*, *c* (Å)	12.178 (1), 20.5805 (17), 46.760 (4)
β (°)	90.270 (2)
V (Å^3)	11719.3 (17)
Z	4
Radiation type	Mo *K*α
μ (mm^{-1})	0.73
Crystal size (mm)	0.25 × 0.01 × 0.01

Data collection	
Diffractometer	Bruker Photon CMOS
Absorption correction	Multi-scan *SADABS* 2016/2, Bruker, 2016
T_{min}, T_{max}	0.702, 0.745
No. of measured, independent and observed [$I > 2\sigma(I)$] reflections	312603, 23047, 21570
R_{int}	0.050
$(\sin\theta/\lambda)_{max}$ (Å^{-1})	0.617
Refinement	
$R[F^2 > 2\sigma(F^2)]$, $wR(F^2)$, S	0.075, 0.180, 1.16
No. of reflections	23047
No. of parameters	1233
No. of restraints	351
H-atom treatment	H atoms treated by a mixture of independent and constrained refinement
	$W = 1/[\Sigma^2(FO^2) + (0.0225P)^2 + 172.6567P]$ WHERE $P = (FO^2 + 2FC^2)/3$
$\Delta\rho_{max}$, $\Delta\rho_{min}$ (e Å^{-3})	2.78, −3.72

7. Steady-state spectroscopy of likers and CPs

7.1 Solvent-dependent absorption spectra of Pr_4sbcd linker

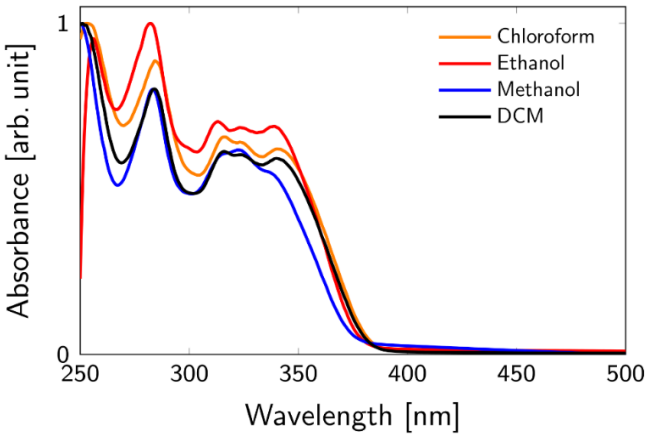

Fig. S18: UV/VIS absorption spectra of Pr_4sbcd measured in different solvents

7.2 Diffuse reflectance spectra of linkers and their corresponding CPs

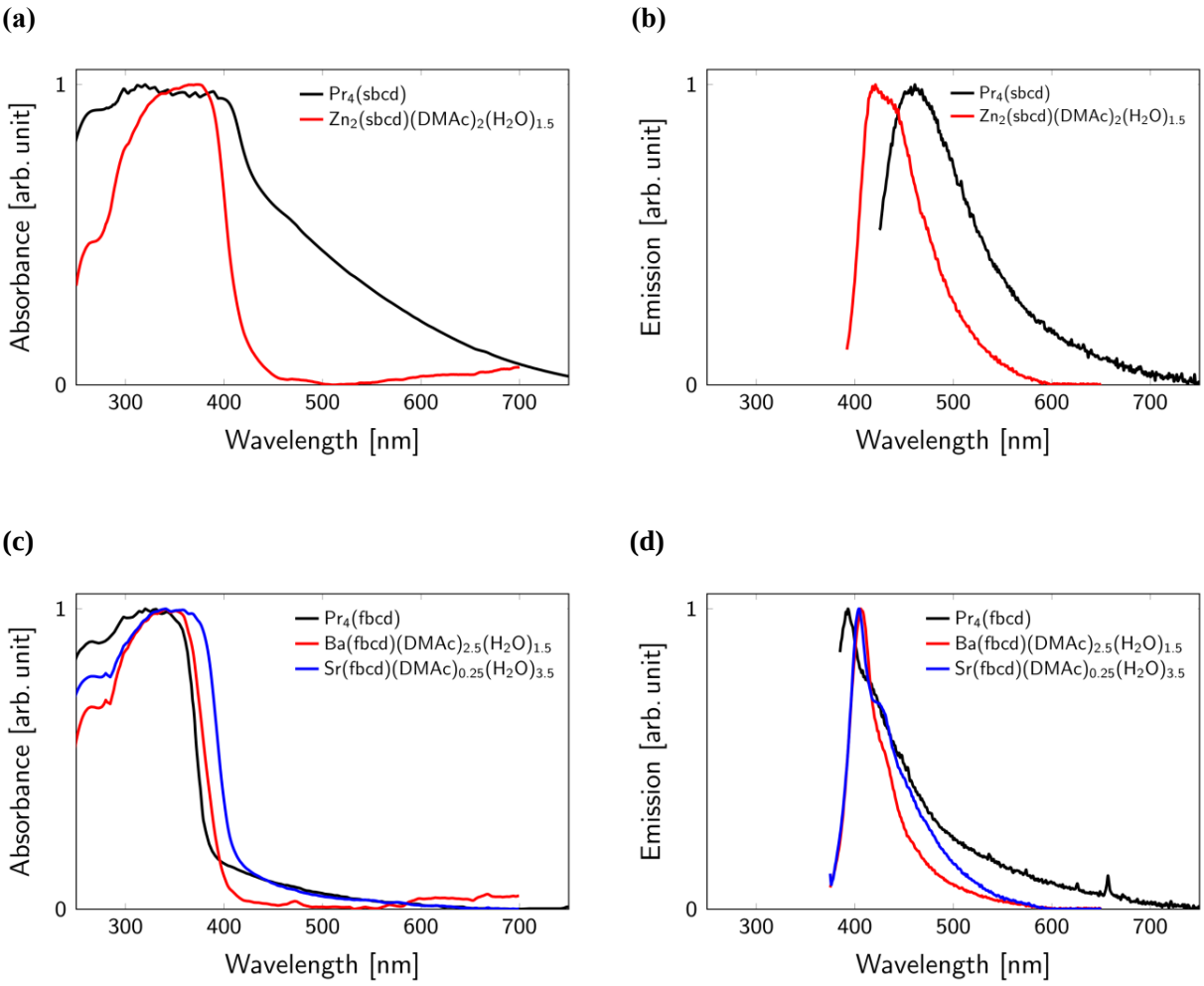

Fig S19: Diffuse reflectance spectra of solid-state linkers and corresponding solid-state CPs. (a) UV/Vis spectra of the linker Pr_4(sbcd) (black) and its corresponding zinc-CP (red) in solid-state. (b) Emission spectra of the linker Pr_4(sbcd) (black) and its corresponding CP (red) in solid-state. (c) UV/Vis spectra of the linker Pr_4(fbcd) (black) and its corresponding strontium-CP (blue) and barium-CP (red) in solid-state. (d) Emission spectra of the linker Pr_4(fbcd) (black) and its corresponding strontium-CP (blue) and barium-CP (red) in solid-state.

8. Sample preparation of CPs for the Z-scan measurements

All three CP crystalline powders are finely grinded to the uniform powders. Each CP powder was weighted (see Table S2) and mixed with 0.5 g PMMA (1.18 g/mL) powder into 5 mL DCM and was stirred for 2h in the solution. Afterwards PMMA films of the resulting dispersions were produced using the "doctor blading" technique with subsequent evaporation of the DCM.

Table S2: Parameters used to calculate the concentration of CPs in PMMA-film state.

CPs	Molecular weight [g/mol]	Mass [mg]	Concentration [mol/L]
$Zn_2(sbcd)(DMAc)_2(H_2O)_{1.5}$	1014.41	16.7	0.0389
$Ba(fbcd)(DMAc)_{2.5}(H_2O)_{1.5}$	1080.30	13.0	0.0284
$Sr(fbcd)(DMAc)_{0.25}(H_2O)_{3.5}$	871.13	20.2	0.0547

9. References

1. Steiger, W.; Gruber, P.; Theiner, D.; Dobos, A.; Lunzer, M.; Van Hoorick, J.; Van Vlierberghe, S.; Liska, R.; Ovsianikov, A., Fully automated z-scan setup based on a tunable fs-oscillator. *Opt. Mater. Express* **2019,** *9* (9), 3567-3581.

B. Full-length article of Section 2.2

Reproduced from Deger, S.N.[†]; Cui, Y.[†]; Warnan, J.; Fischer, R.A.; Šanda, F.; Hauer, J.; Pöthig, A. Influence of chromophore packing on multiphoton absorption in carbazole-based pillar-layered coordination polymers. *ACS Applied Optical Materials*, **2024**, with the permission of American Chemical Society.

ACS APPLIED OPTICAL MATERIALS

pubs.acs.org/acsaom

Forum Article

Influence of Chromophore Packing on Multiphoton Absorption in Carbazole-Based Pillar-Layered Coordination Polymers

Simon N. Deger,[⊥] Yang Cui,[⊥] Julien Warnan, Roland A. Fischer, František Šanda, Jürgen Hauer,* and Alexander Pöthig*

Cite This: https://doi.org/10.1021/acsaom.4c00080

Read Online

ACCESS | Metrics & More | Article Recommendations | Supporting Information

ABSTRACT: Coordination polymers (CP) and their subgroup metal−organic frameworks (MOF) are promising classes of modular multiphoton-absorption active materials. However, a detailed knowledge of the structure−property relationship or generalized design principles remains elusive. This study examines how various packings of the chromophore linker 9,9′-stilbene-bis-carbazole-3,6-dicarboxylic acid in three synthesized zinc-based CPs affect their MPA activity. Different spatial chromophore arrangements are achieved by the so-called "pillar-layer" synthesis approach, using the chromophore and two different additional pillar linkers (4,4′-bipyridine and 1,2-bis(4-pyridyl)ethane) for CP formation. Two novel pillar-layered CPs, $Zn_{2n}(sbcd)(bpy)(DMAc)_{2n}(H_2O)_{3n}$ and $Zn_{2n}(sbcd)(bpe)(DMAc)_{3n}(H_2O)$, are reported and examined in their two-photon-absorption-induced photoluminescence and compared to a previously synthesized CP $Zn_{2n}(sbcd)(DMAc)_{2n}(H_2O)_{1.5n}$, containing the same chromophore but no pillars. The comparison shows significant differences for the two-photon absorption cross-sections of the materials, improving it by incorporating the pillar. Our findings point toward the significance of controlling the chromophore orientation to tailor the nonlinear optical properties of the materials. These insights pave the way toward an aim-directed development of MOFs for advanced photonic applications.

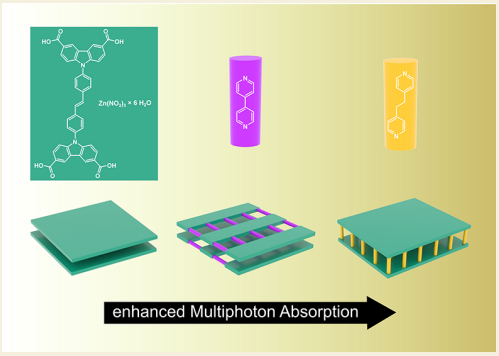

KEYWORDS: *coordination polymers, metal−organic frameworks, multiphoton absorption, nonlinear optics, structure−property relationships, single crystals*

INTRODUCTION

The invention of lasers has been a transformative milestone in scientific research, enabling significant advances across various disciplines.[1] Among the previously inaccessible optical phenomena, triplet−triplet up-conversion[2] and nonlinear optical (NLO) effects have gained prominence. NLO effects and materials are currently being explored for their application in optical filters and information encryption.[3−5] One of the best studied NLO effects is multiphoton absorption (MPA), having found applications in bioimaging,[6] 3D-data storage,[7] and other implementations.[8] MPA belongs to the group of third-order NLO processes, as it involves the conversion from a lower energy level to a higher energy level through simultaneous absorption of multiple photons in a single event.[8−10] The fundamental effect is, therefore, two-photon absorption (2PA), which is quantified by the two-photon absorption cross-section ($\sigma^{(2)}$), measured using the Göppert−Mayer unit (GM = 10^{-50} cm^4 × s × photon^{-1}).[11]

The fundamental difference between one photon absorption (1PA) and 2PA becomes obvious in the expressions for the transition moments $M_{fg}^{(1),(2)}$ between the ground (g) and excited states (f), where the superscript in parentheses stands for 1PA or 2PA, respectively.[12] The respective absorption cross-sections scale with the expectation value of $|M_{fg}^{(1),(2)}|^2$. For 1PA the matrix elements is:

$$M_{fg}^{(1)} = \langle f|\vec{E}\cdot\vec{\mu}|g\rangle \quad (1)$$

where $\vec{E}$ stands for the excitation light field along a defined polarization direction and $\vec{\mu}$ is the dipole moment operator. Two-photon absorption is most efficient if the frequency of the driving laser ω_L meets a resonance condition given by $\omega_{f'g} = 2\omega_L$, where state f' is the final state reached by the 2PA process. The 2PA probability is defined by the cross-section $\sigma^{(2)} \propto |M_{f'g}^{(2)}|^2$ derived from the two-photon transition matrix element:

Special Issue: Upconversion Optical Materials

Received: February 16, 2024
Revised: March 28, 2024
Accepted: March 28, 2024

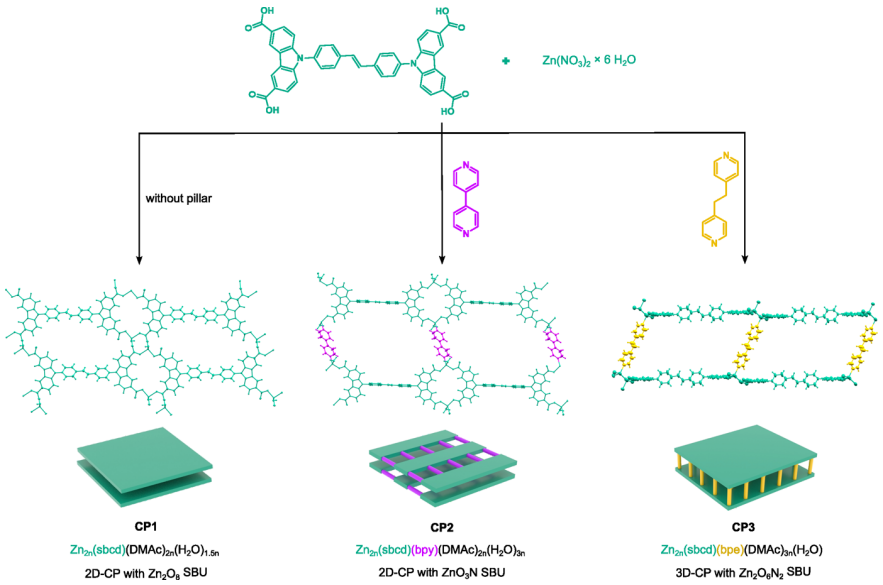

Figure 1. Overview of the synthesized materials discussed in this publication.

$$M^{(2)}_{f'g} = \frac{1}{\hbar}\sum_{e}\frac{\langle f'|\vec{E}\cdot\vec{\mu}|e\rangle\langle e|\vec{E}\cdot\vec{\mu}|g\rangle}{\omega_{eg}-\omega_{L}} \quad (2)$$

where ω_L stands for the frequency of the driving laser field and ω_{eg} for the transition frequency between the ground state and nonresonant intermediate transient levels e. The final excited state f' after 2PA is usually different from f after 1PA as the analysis of eqs 1 and 2 suggests different selection rules for them. Consequently, the transition between the ground and final state does not have to be one-photon allowed. The dependence of $M^{(2)}_{f'g}$ on detuning $\omega_{eg} - \omega_L$ is an important feature of eq 2, as only those transient e levels close to resonance with ω_L will contribute significantly.

In the search for optimized $\sigma^{(2)}$ values, different materials such as perovskites,[13] polymers,[7] and molecular organic chromophores have been investigated.[14] Organic chromophores possess the advantage of abundancy of synthesis and the potential for tuning 2PA properties by incorporating different functional groups.[15] Thereby, they access dipolar, quadrupolar, or branched molecules for increasing intermolecular interactions and consequently $\sigma^{(2)}$.[10,15] However, they possess different disadvantages, such as the tendency to aggregate and quench fluorescence in highly concentrated solutions, as well as limited optical stability.[9,11] Therefore, the stabilization of chromophores has gained research momentum, and inorganic−organic hybrid materials have been targeted as possible supporting scaffolds for chromophores.[9,11,16] In this regard, coordination polymers (CPs) and metal−organic frameworks (MOFs) are promising modular materials from their abundant organic linkers spatially templated by secondary building units (SBUs), predominantly metal-oxo clusters.[17] They are known to have a wide variety of potential applications, e.g., catalysis[18] or gas storage,[19] and more recently, photophysical applications like MPA.[9,11,20]

Incorporating the MPA-active chromophores into the framework has two potential immediate benefits: reducing photobleaching and enhancing the MPA cross-section.[9,21] Because of ordered crystalline structures in CPs/MOFs, ligand molecules can be fixed periodically with a controllable intermolecular distance. Therefore, dense chromophore packing may be achieved with a reduced reabsorption effect. Alternatively, a planar conformation of chromophore scaffold improves charge delocalization across molecules due to a larger overlap of π orbitals, which has proved to be a key factor that leads to optimized multiphoton absorption.[22,23] Furthermore, the rigidity of the framework can effectively limit radiationless decay pathways, which can lead to an increase in $\sigma^{(2)}$.[11,24] Additionally, the diversity in the choice of SBUs and coordination number allows for modulation of (stronger) intermolecular interaction.[25] Notably, the choice of SBUs not only influences the structural aspects but also introduces polarization effects, which facilitate the emergence of new charge transfer channels, consequently impacting the MPA cross-section.[26]

In general, pillar-layered MOFs offer the possibility of modifying the structure of MOFs without altering the (chromophore) linkers or SBUs. Via the introduction of "pillar" (linker) molecules, various aspects such as interlinker distances, pore size, and other structural features can be varied,[27] and examples of pillared-layer MOFs have been previously synthesized and investigated toward MPA activity.[28−31] However, due to the complex interplay of influencing parameters (e.g., chromophore-packing, -orientation, and -density) and challenges toward selectively synthesizing isostructural, (non)polymorphous MOFs, no general design principle for structure−property relationships in MPA active MOFs has been established.[26,30,31]

In this Article, we present the synthesis of two new pillar-layered Zn-CPs $Zn_{2n}(sbcd)(bpy)(DMAc)_{2n}(H_2O)_{3n}$ (**CP2**) and $Zn_{2n}(sbcd)(bpe)(DMAc)_{3n}(H_2O)$ (**CP3**) using the linker H_4sbcd (H_4sbcd = 9,9′-stilbene-bis-carbazole-3,6-dicarboxylic acid) with identical metals in the SBUs and chromophore linkers, differing only in the chemical structure of the incorporated "pillars", which are 4,4′-bipyridine (bpy) and 1,2-bis(4-pyridyl)ethane (bpe). This allows for the investigation of a potential structure−property relationship (between the chromophore packing and their NLO properties). The results are compared with the corresponding, pristine two-dimensional (pillar-free) Zn-CP structure $Zn_{2n}(sbcd)(DMAc)_{2n}(H_2O)_{1.5n}$ (**CP1**), previously published

https://doi.org/10.1021/acsaom.4c00080
ACS Appl. Opt. Mater. XXXX, XXX, XXX−XXX

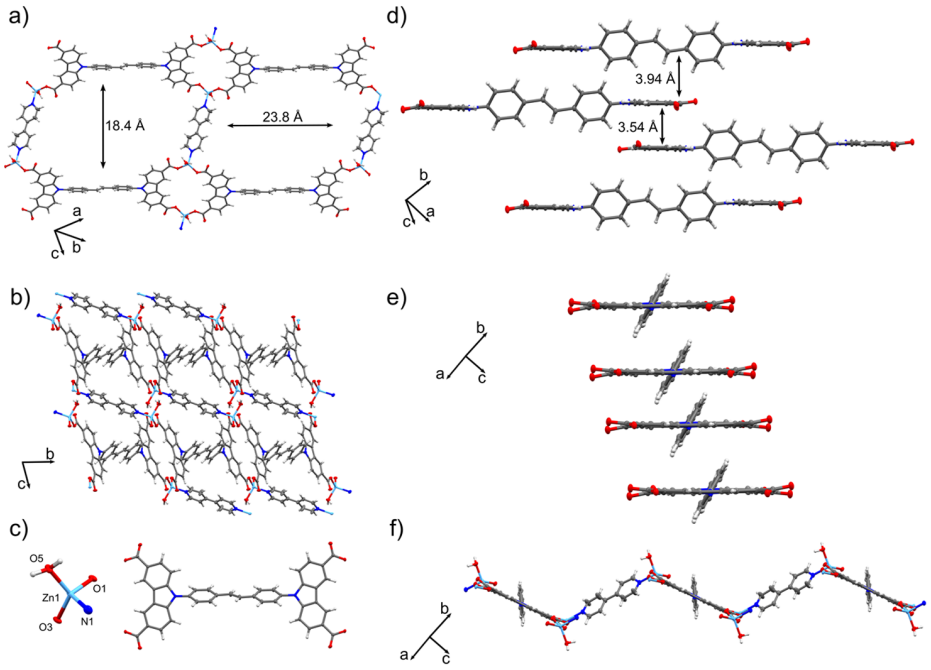

Figure 2. (a) Top view on a monolayer of **CP2** showing the interlinker and interpillar distances measured from the closest point. (b) Depiction of **CP2** along the *a* axis. (c) SBU and linker conformation inside the framework. (d) Representation of the packing and distances between the chromophores in **CP2**. (e) Visualization of the offset between the single linker strings alongside the linker N−N axis. (f) Zigzag conformation of the single CP sheets. Color coding: gray = carbon, blue = nitrogen, red = oxygen, and turquoise = zinc.

by our research group (Figure 1),[26] for which no direct structure−NLO−property relationship could be established. Compared to those of the nonpillar-layered **CP1**, the obtained data for **CP2** and **CP3** show the increase of $\sigma^{(2)}$. This indicates that the pillar-layering approach is a potential avenue to get a more comprehensive understanding of the effects of structural changes on the MOF's NLO properties and control as well as improve them.

RESULTS AND DISCUSSION

Synthesis, Structural Analysis and Comparison between $Zn_{2n}(sbcd)(DMAc)_{2n}(H_2O)_{1.5n}$ (CP1), $Zn_{2n}(sbcd)(bpy)(DMAc)_{2n}(H_2O)_{3n}$ (CP2), and $Zn_{2n}(sbcd)(bpe)(DMAc)_{3n}(H_2O)$ (CP3)

The linker molecule 9,9′-stilbene-bis-carbazole-3,6-dicarboxylic acid (H_4sbcd) was synthesized according to the previously published procedure; further information can be found in the Supporting Information (Figures S1−S3).[26] The "pillar-free" $Zn_{2n}(sbcd)(DMAc)_{2n}(H_2O)_{1.5n}$ **CP1** serves as a comparison in this study, so the influence of the pillars on packing and subsequently $\sigma^{(2)}$ of the materials can be investigated. In **CP1**, two carboxylic acid group atoms connect two zinc centers, forming a Zn_2O_8 cluster as the SBU. This SBU includes two water molecules on top of each tetrahedron. The SBUs further connect four linker molecules, leading to a 2D sheet-like sql-network topology. Alongside the *b*/*c* and *a*/*b* planes, an offset parallel stacking of the layers is observed, as expected for electron-rich-aromatic molecules, leading to an alternating packing of carbazoles and carbazole with the stilbene core.[32] In the *a*/*b* plane, a distance of 3.39 Å between the carbazoles and a carbazole−stilbene distance of 3.83 Å becomes apparent, resulting in a chromophore density of 1.40 mol/dm^3.

The CPs were synthesized by a solvothermal synthesis adjusted from that of the previously published Zn-CP (**CP1**) without the pillar.[26] To obtain phase pure and sufficiently large crystallites of the new CPs for SC-XRD analysis, the synthesis of CP1 was slightly modified. The reaction of H_4sbcd with 2.50 equiv of bpy and 3.00 equiv of $Zn(NO_3)_2{\cdot}6H_2O$ in 2.50 mL of a dimethylacetamide (DMAc)/H_2O mixture at 90 °C afforded block-shaped clear colorless single crystals which were analyzed by SC-XRD, PXRD, TGA, and IR, revealing and confirming the composition $Zn_{2n}(sbcd)(bpy)\text{-}(DMAc)_{2n}(H_2O)_{3n}$ (**CP2**) as well as successful incorporation of the linker (see Figures S4−S6).

CP2 forms a two-dimensional, sheet-like framework and crystallizes in the triclinic space group $P\bar{1}$ with the unit cell parameters a = 9.8240(7) Å, b = 11.3596(8) Å, c = 13.6356(11) Å, α = 76.524(3)°, β = 73.942(3)°, and γ = 74.063(3)° (Figure 2). The sheets of the CP are composed of linker molecules arranged in strings (see Figure 2a), which are connected via the ZnO_3N SBU (see Figure 2c). The SBU is formed by two κ^1-binding linkers (O1, O3), as well as additional coordinated water, and bpy molecules, which bridge the linker strings within the sheet structure (see Figure 2c). The sheets are not planar but show a zigzag conformation (Figure 2f), exhibiting a 65.8° angle between the pillars and the linkers. They are densely packed (with a chromophore density of 1.20 mol/dm^3), held together through π stacking, and further stabilized by hydrogen bonds between the water molecules coordinated with the SBU and the uncoordinated oxygen atoms of the carboxylic acid groups of the linkers (refer to Figure 2b). The conformation of the linker inside the framework holds a 58.9° twist between the carbazole and the stilbene moiety (Figure 2c).

https://doi.org/10.1021/acsaom.4c00080
ACS Appl. Opt. Mater. XXXX, XXX, XXX−XXX

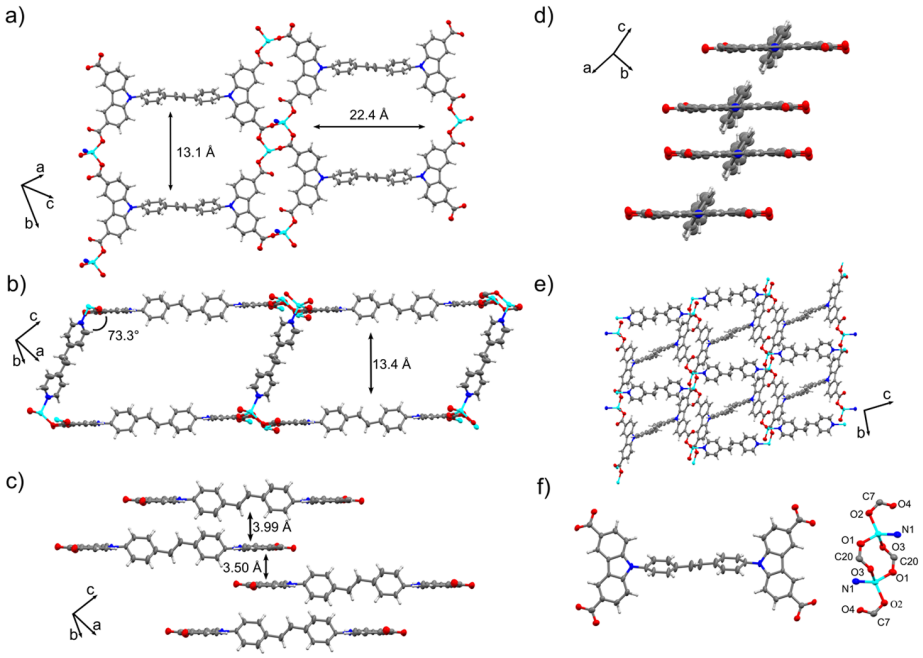

Figure 3. (a) Monolayer of the sbcd linker two-dimensional sheets in **CP3** ("linker sheets"). (b) Connection of the planar linker sheets by bpe pillars. (c) Intermolecular distances of sbcd linkers visualizing their tight packing inside the network. (d) Visualization of the offset between the single linkers alongside the linker N−N axis in the packing of **CP3**. (e) Depiction of **CP3** along the *a* axis. (f) Linker conformation inside the network and $Zn_2O_6N_2$ metal node. Color coding: gray = carbon, blue = nitrogen, red = oxygen, and turquoise = zinc.

Despite the zigzag conformation of the pillars, the linkers are stacked parallel to one another at a distance of 3.54 Å, alternating between two stacked off-center carbazoles and the built-in stilbene core, which is stacked 3.94 Å from the following carbazole (see Figure 2d). The single linker strings are shifted by 1.26 Å in relation to each other (see Figure 2e), resulting in an off-center parallel stacking, as in **CP1**.

In **CP2**, a different type of 2D periodic sheet can be observed compared to **CP1**. The bpy pillar is part of the sheet ("linker-pillar sheets") for **CP2**. The pristine dinuclear Zn_2O_8 SBU of **CP1** can be imagined to be virtually split by introduction of the bpy pillar, leading to two mononuclear Zn-SBUs bridged by bpy. This quasiextension of the SBU leads to a significant enlargement of the mesh in the 2D sheet with 13.1 × 22.4 Å compared to 18.4 × 23.8 Å for **CP1** and **CP2**, respectively.

To obtain a structurally different framework, the reaction of H_4sbcd with 3.00 equiv of $Zn(NO_3)_2{\cdot}6H_2O$ and 2.50 equiv of bpe in 2.00 mL of DMAc at 90 °C was performed. Clear block-shaped single crystals of **CP3** were obtained, crystallizing in space group $P\bar{1}$ as a three-dimensional CP. This 3D-CP consists of linker sheets assembled from the SBU and linkers as in **CP1** that are connected by the bpe pillars. A crystal has the following cell parameters: a = 8.3961(16) Å, b = 13.253(3) Å, and c = 13.510(3) Å, with cell angles of α = 72.953(7)°, β = 78.176(7)°, and γ = 72.835(7)°.

Figure 3a shows a monolayer cutout of **CP3**, demonstrating the planarity of the linker molecules arranged in two-dimensional sheets. These linker sheets are connected to each other through the bpe pillars, as depicted in Figure 3b, forming an angle of 73.3° between the pillars and the linker sheet. This makes the composition Zn_{2n}(sbcd)(bpe)-$(DMAc)_{3n}(H_2O)$ obvious, and the single crystals were furthermore analyzed with PXRD, TGA, and IR, confirming the successful incorporation of the linker and confirming the composition (Figures S4−S6). Induced by the angle, the distance between the pillar's connected layers is 13.4 Å. The SBU consists of two zinc cations connected by two bridging κ^1:κ^1 carboxylic (O1, O3) acid groups. Furthermore, two additional carboxylic acids (O2) bind in a κ^1 fashion, resulting in a total of four linker molecules connected to the metal node. Each zinc metal center is bound to a nitrogen atom (N1) from the bpe pillar, completing the tetrahedral coordination sphere of each zinc.

CP3 shows a 3-fold interpenetrated structure, leading to a close packing of the sbcd chromophores with a chromophore density of 1.22 mol/dm^3, similar to that of **CP2** (see Figure 3e). Comparably to **CP1** and **CP2**, the linkers are packed in off-center parallel stacking. However, in this case, the carbazoles of two sheets are aligned coplanar to each other at a distance of 3.50 Å, followed by a stilbene core of a third sheet stacked 3.99 Å above the carbazoles (Figure 3c) but now shifted by a larger margin of 2.50 Å compared to the previous CPs (Figure 3d). Additionally, there is a 57.5° rotation of the stilbene core compared with the carbazole.

In contrast to **CP2**, in **CP3**, the nuclearity of the zinc SBU, as well as the general structure of the pristine sheet like in **CP1** are preserved. However, compared to **CP1**, the bpe pillar can be imagined to be inserted in between the 2D "linker sheets", now connecting them by virtually replacing the originally coordinating water molecule of the Zn_2O_8 SBU, leading to $Zn_2N_2O_6$ SBUs and a three-dimensional network.

Despite the differences discussed in the structural arrangements induced by pillar incorporation, the tight packing and interpenetration resulted in comparable arrangements and observable interchromophoric distances within the three frameworks. However, a less distorted, i.e., more planar, molecular structure of the chromophore linkers is present both

https://doi.org/10.1021/acsaom.4c00080
ACS Appl. Opt. Mater. XXXX, XXX, XXX−XXX

in **CP2** and **CP3** compared to **CP1**, this phenomenon is expected to positively influence 2PA.[9]

Steady-State Spectroscopy of H_4sbcd and CPs

The purity of the bulk material samples for photophysical characterization was confirmed by a combination of PXRD, TGA, and elemental analysis (Supporting Information). One-photon optical spectroscopy and IR spectroscopy (Figure S5) were performed for the H_4sbcd linker and corresponding CPs (Figure 4). H_4sbcd was dissolved in DMF with a concentration

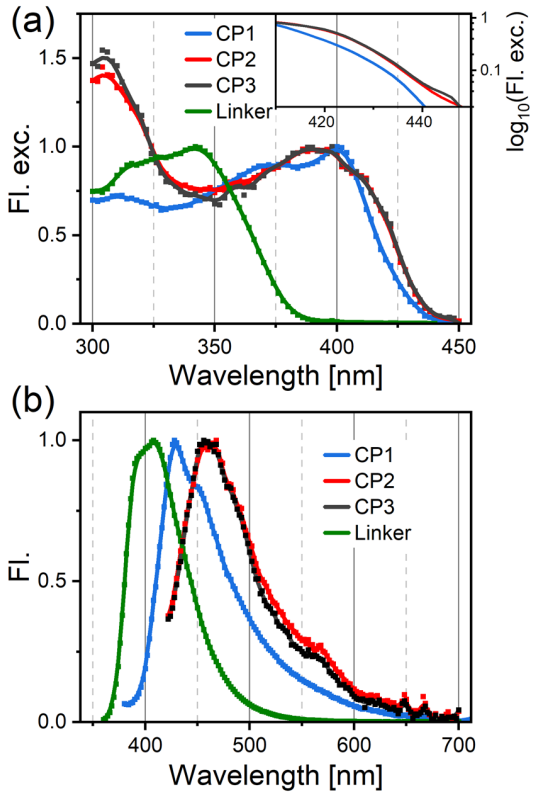

Figure 4. (a) Fluorescence excitation spectra of the H_4sbcd linker (detection wavelength at 450 nm) in DMF and corresponding CPs in the PMMA-film state. (b) Emission spectra of the H_4sbcd linker (excitation at 350 nm) and CPs. Note: to remove Raman peaks in the excitation and emission spectra for solid samples, CPs were excited and monitored at different wavelengths. For the excitation spectra of CPs, the detection wavelengths were set at 500, 510, and 520 nm, while for the emission spectra of CPs, the excitation wavelengths were set at 330, 340, 350, and 360 nm. Raman peaks can thus be removed significantly by stacking these excitation or emission spectra together.

of 10 μmol/L while solid samples of **CP1**, **CP2**, and **CP3** were prepared as a PMMA film using the doctor blade method with a concentration in the range of 9−38 mmol/L (see Table S3).

The excitation spectrum of the linker shows a broad absorption band at around 325 nm (Figure 4a). In comparison, the excitation spectra of the CPs show a redshift of approximately 50 nm and broadening in all CPs. The redshift, as well as the broadening of the absorption bands, points toward a higher excitonic interaction in the materials than in the linker.[26] In addition, structure rigidification and interligand charge transfer were also proposed to explain the spectral shift in the CP environment.[33−36] Comparing the CP-spectra, **CP1** shows the least pronounced redshift, while **CP2** and **CP3** are similar in this respect. The linear−log plot shown as an inset in Figure 4a shows that **CP3** extends marginally further to the red compared to CP2. A comparison of the CPs' emission spectra with the linker molecule again shows a redshift upon incorporation of the linker into the CPs. **CP1** shows a redshift of 25 nm, while **CP2** and **CP3** show similar emission spectra but are red-shifted up to 60 nm, as shown in Figure 4b. We note that the small emission peaks at wavelengths longer than 650 nm in the emission spectra of **CP2** and **CP3** originate from Raman scattering. The redshift in emission of the CPs compared to the linker can be rationalized by two structural effects. First, the $\pi-\pi$ interactions between adjacent linker molecules in the solid state may facilitate efficient intermolecular interactions through π-stacking.[37] Second, the increased planarity of the linker in **CP2** and **CP3** as compared to **CP1** may maximize the intramolecular π-orbital overlap and promote further $\pi-\pi$ interactions,[38] explaining the extra shift of the emission band.[38,39] Fluorescence quantum yields (QY) of all CPs are lower than those for the H_4sbcd linker in solution (Φ = 0.76). **CP1** shows the highest quantum yield Φ = 0.11, followed by **CP3** Φ = 0.015, and the lowest in **CP2** Φ = 0.010. Such a reduction of QY after incorporation of chromophores into the CP has been observed before and was explained by introduction of radiationless decay pathways by the pillars, aggregation, or reduction of the active H_4sbcd molecule in the pillar-layered CPs.[30] This, however, does not necessarily imply a lower $\sigma^{(2)}$ for the CPs, as a previous study inferred no direct correlation between the two values.[28]

Nonlinear Optical Characterization of the Linker and CPs

Nonlinear optical characterization of the linker and CPs was conducted via nonlinear Fourier-transform spectroscopy.[40] This method provides a broadband two-photon excitation spectrum for the substance under investigation. The used setup shares the working principle with the experiment of Hashimoto et al.,[40] with the exception that our design employs a noncollinear optical parametric amplifier (NOPA) for a broadband excitation laser and a common-path birefringent interferometer instead of a Michelson interferometer to generate pulse pairs. Pulse compression was achieved using a prism pair compressor, producing a routinely available 10 fs pulse for the 2PA measurement. The typical NOPA output falls in the range of 750−950 nm, tunable to shorter wavelengths if necessary. In this study, we utilized two NOPA spectral ranges to investigate the H_4sbcd linker and corresponding CPs, presenting the 2PA data in the fundamental wavelength range from 740 to 920 nm. $\sigma^{(2)}$ values were calibrated using fluorescein in water (pH 11) for the H_4sbcd linker and **CP1** for **CP2** and **CP3** (cf. Supporting Information).[26,41]

The 2PA spectrum of H_4sbcd is presented in Figure 5a. The 1PA spectrum shows an absorption edge at around 400 nm. This explains the lack of observable 2PA at a fundamental wavelength above 800 nm. Notably, $\sigma^{(2)}$ values are less than 3 GM in this region, emphasizing the sensitivity of our 2PA measurement technique. As the frequency-doubled fundamental wavelength begins to overlap with the 1PA spectrum, a sharp increase in $\sigma^{(2)}$ is observed, reaching up to 80 GM at 740 nm. It is anticipated that the $\sigma^{(2)}$ value for H_4sbcd will be even higher at shorter wavelengths, given the 1PA absorption band's peak intensity at 340 nm. Similar molecules featuring a stilbene core with carbazole donors have been previously studied for their 2PA cross-section, achieving values of up to 200 GM at 680 nm.[42]

https://doi.org/10.1021/acsaom.4c00080
ACS Appl. Opt. Mater. XXXX, XXX, XXX−XXX

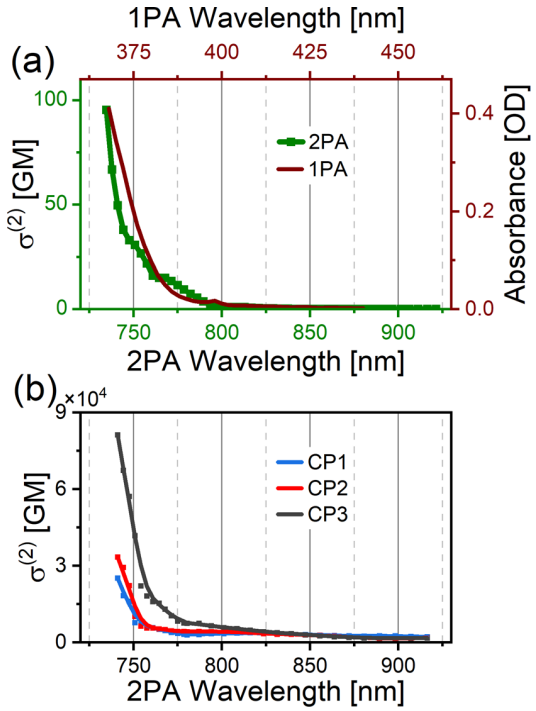

Figure 5. (a) Experimental 2PA spectrum of H_4sbcd in DMF (green dots and line) compared with its one-photon excitation spectrum (brown line). (b) 2PA spectra of **CP1** (blue), **CP2** (red), and **CP3** (dark gray).

After incorporating the linker molecules into CPs, the observed red-shift in the 1PA spectrum enables the measurement of 2PA from a wavelength of 900 nm, as depicted in Figure 5b. Within the employed excitation range, **CP2** exhibits $\sigma^{(2)}$ values ranging from 1340 to 33 457 GM, **CP3** values from 1501 to 81 267 GM, and **CP1** values from 2258 to 25 156 GM (Table 1). At this point, it should be noted that the $\sigma^{(2)}$ of **CP1** deviates from our previous publication, which was measured using a fully automated Z-scan setup and showed values of 2137−15 838 GM.[26,43] We place greater confidence in the present data set due to the significantly extended data acquisition time required for Z-scan measurements in comparison to the interferometric approach outlined herein. Swept laser sources are often used in a Z-scan method; therefore, excitation intensities and pulse durations at each central wavelength must be characterized with great care. As a wavelength scanning method, recording a broadband 2PA spectrum may take several tens of minutes.[42,44,45] Consequently, the potential for sample degradation is more pronounced in the Z-scan measurement, impacting the result of the measurement.[46] As a contrast, in our approach, a broadband laser with 10 fs pulses was focused on the sample. Therefore, a complete 2PA spectrum can be acquired in less than 3 min.

Table 1. 2PA Cross-Sections of the Reported CPs/MOFs in the Range of 740 to 920 nm

CPs/MOFs	2PA cross-section $\sigma^{(2)}$ (10^3 GM)
Zn_{2n}(sbcd)$(DMAc)_{2n}(H_2O)_{1.5n}$ (**CP1**)	2.258−25.156
Zn_{2n}(sbcd)(bpy)$(DMAc)_{2n}(H_2O)_{3n}$ (**CP2**)	1.340−33.457
Zn_{2n}(sbcd)(bpe)$(DMAc)_{3n}(H_2O)$ (**CP3**)	1.501−81.267

In all cases, the generally enhanced 2PA of the CPs compared to that of the linker is attributed to the linker incorporation into the framework, as was observed in other cases.[9] Interestingly, with the same linker and SBU metal shared, the activity of the CPs varies significantly.

The 2PA cross-section of **CP1** and **CP2** stays relatively constant with a slight improvement in **CP2**, while **CP3** shows a drastically improved performance despite the fact that the observable packing of the linker stays similar with only minor differences. The enhancement of $\sigma^{(2)}$ in **CP2** and **CP3** with respect to **CP1** can be attributed to the planarization of the linker molecule.[47] This planarization, coupled with relatively short distances between chromophores in the material, likely results in stronger $\pi-\pi$ intermolecular interactions, known to positively influence the MPA response.[25,47] The different SBUs and sheet structures, however, appear not to have a big impact on the 2PA activity.

The 2.4-fold increase in $\sigma^{(2)}$ from **CP2** to **CP3** cannot be accounted for by the planarization of the linker in this comparison, as in both cases the linker remains planar. Notably, the rotation of the stilbene compared to the carbazole is smaller in **CP3** compared to that of **CP2** (57.5° vs 58.9°). This subtle difference may enhance intermolecular interactions, given that the stilbene is more in-plane with the carbazole, increasing orbital overlap and therefore increasing the charge-transfer between chromophores.[48] Furthermore, as illustrated in Figure 2e and 3d, the chromophore alignment in **CP3** is more coplanar than that in **CP2**. This is potentially amplifying intermolecular interactions and, consequently, the 2PA cross-section.[38] Moreover, the 3D-MOF structure in **CP3** enforces more rigidity compared to the 2D structures in **CP2** and **CP1**, likely contributing to the increased 2PA activity as well.[16]

Besides optimization of the structure to enhance the intermolecular interactions and rigidity in the CPs and, in turn, $\sigma^{(2)}$, this surprisingly large increase of $\sigma^{(2)}$ can be further rationalized by fine-tuning of nonresonant levels of centrosymmetric linkers in the CPs, as detailed in the following. Both the one-photon allowed states (with transitions shown in Figure 4a) and the nonresonant intermediate states (e in eq 2) follow the same selection rules and tend to behave similarly in terms of bathochromic shifts.[49] The same is not necessarily true for the two-photon active f' state. In fact, for centrosymmetric molecules such as stilbene—the parent compound of H_4sbcd—the rule of mutual exclusion applies for $g \rightarrow f$ and $g \rightarrow f'$ transitions. Accordingly, the one-photon resonance shifts between the linker and CPs (and between CPs), and the main peak for the two-photon resonance remains located at the blue edge of the excitation spectrum for the linker and all CPs, as depicted in Figure 5a. Assuming similar trends for the one-photon $g \rightarrow f$ transitions and the first step of a two-photon absorption process, $g \rightarrow e$, we can expect that frequency shift in the one-photon spectrum may indicate a shift in energy in the manifold of nonresonant e states. This situation is depicted in Figure 6. We note that the arguments made here apply rigorously to a generalized centrosymmetric system. More specific arguments would require quantitative quantum chemical calculations of 2PA cross sections of the free ligand and the ligand in the CP environment and are beyond the scope of this manuscript.[12]

https://doi.org/10.1021/acsaom.4c00080
ACS Appl. Opt. Mater. XXXX, XXX, XXX−XXX

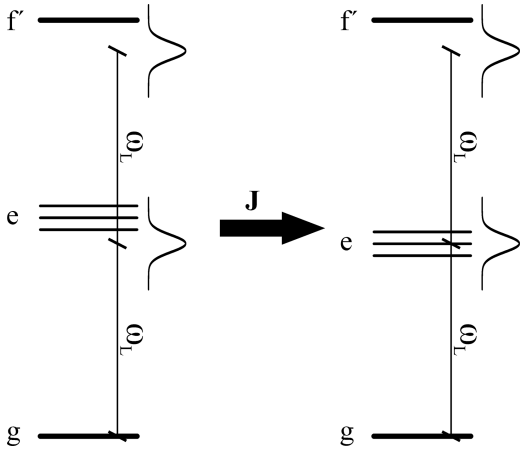

Figure 6. Schematic energy level diagram of a two-photon absorption process with a nonresonant intermediate step. For the uncoupled molecule (i.e., the linker, left side), the manifold on nonresonant states e is detuned from the laser frequency ω_L, contributing to 2PA decreasingly with detuning, see eq 2. The bandwidth of the exciting laser pulse is shown as a Gaussian curve. Upon coupling between chromophores with strength J, i.e., after incorporation of the linker into a CP, the e-manifold shifts toward the laser's center frequency ω_L, leading to increased 2PA. The two-photon state f' is unaffected by coupling.

The uncoupled molecule is assumed to have the energy level diagram shown on the left side of Figure 6. In this scenario, the e-manifold is detuned for laser frequency ω_L, making the $g \rightarrow e$ transition inefficient. This can be the scenario for the isolated linker molecule, explaining its moderate $\sigma^{(2)}$ values. Upon coupling (right side of Figure 6), we expect the e-manifold to red-shift, following the trend of the one-photon absorption spectrum. Even a marginal red-shift may bring the e-manifold in resonance with ω_L. This has no effect on the 1PA cross-section (see Figure 4) but leads to potentially drastic changes in the 2PA cross-section as the denominator of eq 2 can approach zero. We note that changes in solvent polarizability were shown to have a strong effect on $\sigma^{(2)}$, which can, in analogy to the above argument, be interpreted as a shift of the e-manifold.[50]

In summary, there are several arguments based on chemistry and/or crystal structure to explain an increase in 2PA activity of a linker when inserted into a CP.[25] Briefly, the polar CP environment may lead to planarization of the linker or to an increase in charge-transfer character, which is readily associated with larger 2PA cross sections.[51] Similarly, the relative arrangement of transition dipole moments within a CP can lead to enhanced 2PA based on, e.g., excitonic effects.[11] This influence of transition dipole moments $\vec{\mu}$ on 2PA is readily seen in the numerator of eq 2. We add an argument based on the denominator of the said equation. Even a small change in transition frequencies ω_{eg} can lead to a drastic increase of 2PA if it brings ω_{eg} closer to the $\omega_{eg} = \omega_L$ resonance condition.

CONCLUSION

In conclusion, the synthesis and structural characterization of two new coordination polymers (CPs) based on the linker molecule 9,9′-stilbene-bis-carbazole-3,6-dicarboxylic acid (H_4sbcd) have been presented: a two-dimensional CP Zn_{2n}(sbcd)(bpy)$(DMAc)_{2n}(H_2O)_{3n}$ (**CP2**) and a three-dimensional metal−organic framework Zn_{2n}(sbcd)(bpe)$(DMAc)_{3n}(H_2O)$ (**CP3**). Both structures were synthesized via a solvothermal approach adjusted from the synthesis of $Zn_{2n}(sbcd)(DMAc)_{2n}(H_2O)_{1.5n}$ **CP1** previously reported by our group,[26] additionally incorporating ditopic pillar molecules (bpy for **CP2** or bpe for **CP3**, respectively). The introduction of the pillars leads to distinct structural differences in the CP, either by virtual insertion into the dinuclear SBU (**CP2**) or by bridging of the pristine 2D periodic sheets (**CP3**) with reference to the original **CP1**. Both new CPs exhibited enhanced molecular planarity and reduced distortion in the sbcd linker structure. However, the packing of the linkers was only marginally affected compared to CP1.

In-depth photophysical characterization revealed bathochromic shifts in the excitation and emission spectra for all CPs compared to those of the free linker, possibly explained by enhanced excitonic interactions and $\pi-\pi$ interactions within the materials. The nonlinear optical characterization using 2PA spectroscopy demonstrated enhanced 2PA in the CPs compared to the free linker, with **CP3** exhibiting a remarkable 2.4-fold increase in $\sigma^{(2)}$ compared to **CP2** and 3.2-fold increase over **CP1**. The coplanar alignment of chromophores in **CP3**, along with its 3D structure, likely contributes to this increase, emphasizing the importance of structural considerations in influencing the 2PA activity. Accordingly, future CP design should target rigid 3D structures with closely packed chromophores to obtain a high 2PA activity. On a more general level, we find that fine-tuning nonresonant levels has the potential to strongly increase 2PA activity, for centrosymmetric linkers such as stilbene, the desired redshift of nonresonant levels is accompanied by a—maybe subtle—bathochromic shift of the one-photon absorption spectrum. This could be further probed by impedance spectroscopy to further study the influence of the polarization and dielectric constant of the MOFs on the nonresonant levels.[50,52]

The obtained pillar-layered CPs have the highest $\sigma^{(2)}$ among other pillared-layer CPs. The first synthesized pillar-layered CPs by Vittal et al. using the An2Py linker reached values of up to 32.7 GM.[16,28,31] Fischer and colleagues synthesized pillar-layered CPs using the MPA active linker tetra-(4-carboxylphenyl)ethylene (H_4TCPE), reaching values of up to 476 GM, and Vittal et al. improved on this with values up to 74 000 GM by changing the used pillars.[29,30] This competitive performance of pillar-layered systems shows the potential of carbazole-based chromophores in MPA active CPs and MOFs.

The findings show that the pillar-layering approach is a potent way to produce varied CP materials implementing the same chromophores and, in general, contributes to the broader field of CPs and their potential applications in nonlinear optical devices.

EXPERIMENTAL SECTION

Materials and Methods

All purchased reagents were received from chemical suppliers and used without any further purification unless otherwise stated. Dipropyl-9-(4-nitrophenyl)-carbazole-3,6-dicarboxylate and 9,9′-(stilbyl)-bis(carbazole-3,6-dicarboxylic acid) were synthesized following the previously published synthesis procedures.[26,53] All reactions with air- and moisture-sensitive compounds were carried out under standard Schlenk techniques using Argon 4.6 (Westfalen) or in a glovebox (UNIlab, M. Braun). Required glassware was flame-dried in vacuo prior to use. Elemental analysis was performed at the microanalytical laboratory at the Technical University of Munich.

https://doi.org/10.1021/acsaom.4c00080
ACS Appl. Opt. Mater. XXXX, XXX, XXX−XXX

Analysis of C, H, and N values was conducted by using the flash combustion method at 1800 °C. NMR spectra were recorded on a Bruker AV400 instrument at room temperature at 400 MHz. Single-crystal X-ray diffraction (SC-XRD) data were collected on a Bruker D8 Venture system equipped with a Mo TXS rotating anode (λ = 0.71073 Å) and a CMOS photon 100 detector (for detailed information, see the Supporting Information). Capillary PXRD measurements were recorded in transmission geometry on a Stoe STADI P diffractometer equipped with Mo radiation (λ = 0.7093 Å), a curved Ge(111) monochromator, and a Dectris Mythen 1K detector. Fluorescence emission and excitation measurements were recorded on an FS5 spectrofluorometer from Edinburgh Instruments either in solution (linker) or in a PMMA matrix (CPs). For the PMMA matrix, all three CP crystalline powders are finely ground to uniform powders. Each CP powder was weighed and mixed with 0.5 g of PMMA (1.18 g/mL) powder in 5 mL of DCM and stirred for 2 h in the solution. Afterward, PMMA films of the resulting dispersions were produced by using the "doctor blading" technique with subsequent evaporation of the DCM. These samples were then used for 2PA measurements as well. IR measurements were conducted on a PerkinElmer Frontier FT-IR spectrometer. Quantum yield measurements in solution and the solid state were performed on a Hamamatsu Quantaurus-QY Absolute PL quantum yield spectrometer in the scan method in a range of 300−390 nm.

Synthesis

Zn_{2n}(sbcd)(bpy)$(DMAc)_{2n}(H_2O)_{3n}$. In a 4 mL scintillation vial, 10.0 mg of H_4sbcd (14.7 μmol, 1.0 equiv) dissolved in 1 mL of DMAc, 5.68 mg of 4,4′-bipyridine (36.4 μmol, 2.5 equiv) dissolved in 1 mL of DMAc, and 13.0 mg of $Zn(NO_3)_2{\cdot}6H_2O$ dissolved in 0.5 mL of H_2O are added subsequently and heated for 2 days at 90 °C. The resulting white crystalline precipitate is filtered off, washed with DMAc, and dried under air. 8.02 mg (10.4 μmol, 69%) of a white crystalline powder is obtained. EA calcd. for $Zn_2C_{52}H_{30}N_4O_8{\cdot}2C_4H_9O{\cdot}3H_2O$: C, 60.16; H, 4.54; N, 7.02. Found: C, 59.41; H, 4.47; N, 6.66.

Zn_{2n}(sbcd)(bpe)$(DMAc)_{3n}(H_2O)$. 13.0 mg of $Zn(NO_3)_2{\cdot}6H_2O$ is put into a 4 mL scintillation vial. Subsequently, 10.0 mg of H_4sbcd (14.7 μmol, 1.0 equiv) and 6.70 mg of bpe (36.4 μmol, 2.5 equiv) are dissolved in, respectively, 1 mL of DMAc and added to the metal salts. The solution is heated to 90 °C in an oven for 2 days. The obtained white precipitate is filtered off, washed with DMAc, and dried. This yields 5.71 mg (8.94 μmol, 61%) of a light-yellow crystalline powder. EA calcd. for $Zn_2C_{54}H_{34}N_4O_8{\cdot}3C_4H_9O{\cdot}H_2O$: C, 62.08; H, 4.97; N, 7.68. Found: C, 61.27; H, 4.66; N, 7.51.

■ ASSOCIATED CONTENT

Supporting Information

The Supporting Information is available free of charge at https://pubs.acs.org/doi/10.1021/acsaom.4c00080.

Additional synthetic procedures; NMR spectra; IR, PXRD, and TGA; two-photon absorption data processing; and single-crystal X-ray data (PDF)

Accession Codes

CCDC 2333064−2333065 contains the supplementary crystallographic data for this paper. These data can be obtained free of charge via www.ccdc.cam.ac.uk/data_request/cif, or by emailing data_request@ccdc.cam.ac.uk, or by contacting The Cambridge Crystallographic Data Centre, 12 UnionRoad, Cambridge CB2 1EZ, U.K.; fax: + 44 1223 336033.

■ AUTHOR INFORMATION

Corresponding Authors

Jürgen Hauer − *Technical University of Munich, TUM School of Natural Sciences, Department of Chemistry, Professorship for Dynamic Spectroscopy, Catalysis Research Center, 85747 Garching, Germany*; Email: juergen.hauer@tum.de

Alexander Pöthig − *Technical University of Munich, TUM School of Natural Sciences, Department of Chemistry, Chair of Inorganic and Metal−Organic Chemistry, Catalysis Research Center, 85747 Garching, Germany*; orcid.org/0000-0003-4663-3949; Email: alexander.poethig@tum.de

Authors

Simon N. Deger − *Technical University of Munich, TUM School of Natural Sciences, Department of Chemistry, Chair of Inorganic and Metal−Organic Chemistry, Catalysis Research Center, 85747 Garching, Germany*

Yang Cui − *Technical University of Munich, TUM School of Natural Sciences, Department of Chemistry, Professorship for Dynamic Spectroscopy, Catalysis Research Center and TUM School of Natural Sciences, Department of Physics, Catalysis Research Center, 85747 Garching, Germany*; orcid.org/0000-0003-2116-7611

Julien Warnan − *Technical University of Munich, TUM School of Natural Sciences, Department of Chemistry, Chair of Inorganic and Metal−Organic Chemistry, Catalysis Research Center, 85747 Garching, Germany*; orcid.org/0000-0003-2729-8997

Roland A. Fischer − *Technical University of Munich, TUM School of Natural Sciences, Department of Chemistry, Chair of Inorganic and Metal−Organic Chemistry, Catalysis Research Center, 85747 Garching, Germany*; orcid.org/0000-0002-7532-5286

František Šanda − *Institute of Physics, Faculty of Mathematics and Physics, Charles University, Prague 121 16, Czech Republic*; orcid.org/0000-0003-2416-8804

Complete contact information is available at: https://pubs.acs.org/10.1021/acsaom.4c00080

Author Contributions

⊥S.N.D. and Y.C. contributed equally to this work. S.N.D.: conceptualization, methodology, validation, formal analysis, investigation, data curation, writing—original draft, review and editing, visualization. Y.C.: methodology, validation, formal analysis, investigation, data curation, writing—original draft, review and editing, visualization. J.W.: supervision, writing—review and editing. F.S.: writing—review and editing. R.A.F.: resources, writing—review and editing, supervision, project administration. J.H. conceptualization, supervision, writing—review and editing, resources, project administration. A.P. conceptualization, supervision, writing—review and editing, resources, project administration.

Funding

The authors would like to thank the German Research Foundation (DFG) for funding within the frame of the EXC 2089 Cluster of Excellence and the Priority Programme "COORNETs" (SPP 1928). F.S. is supported by the Czech Science Foundation (GACR) through grant no. 22-26376S.

Notes

The authors declare no competing financial interest.

■ ACKNOWLEDGMENTS

The authors would like to thank the German Research Foundation (DFG) for funding within the frame of the EXC 2089 Cluster of Excellence and the Priority Programme

"COORNETs" (SPP 1928). The TUM is greatly acknowledged for its institutional funding. S.N.D. and Y.C. would like to thank the TUM Graduate School for financial support. S.N.D. would like to thank Silva Kronawitter for the support with measurements.

REFERENCES

(1) Moulton, P. F.; Rines, G. A.; Slobodtchikov, E. V.; Wall, K. F.; Frith, G.; Samson, B.; Carter, A. L. G. Tm-Doped Fiber Lasers: Fundamentals and Power Scaling. *IEEE J. Sel. Top. Quantum Electron.* **2009**, *15* (1), 85−92.
(2) Monguzzi, A.; Tubino, R.; Hoseinkhani, S.; Campione, M.; Meinardi, F. Low power, non-coherent sensitized photon up-conversion: modelling and perspectives. *Phys. Chem. Chem. Phys.* **2012**, *14* (13), 4322−4332.
(3) Byer, R. L. Nonlinear Optical Phenomena and Materials. *Annu. Rev. Mater. Sci.* **1974**, *4* (1), 147−190.
(4) Chen, W. Spatial nonlinear optics for securing information. *Light Sci. Appl.* **2022**, *11* (1), 11.
(5) Dini, D.; Calvete, M. J. F.; Hanack, M. Nonlinear Optical Materials for the Smart Filtering of Optical Radiation. *Chem. Rev.* **2016**, *116* (22), 13043−13233.
(6) Wei, Z.; Pan, Y.; Hou, G.; Ran, X.; Chi, Z.; He, Y.; Kuang, Y.; Wang, X.; Liu, R.; Guo, L. Excellent Multiphoton Excitation Fluorescence with Large Multiphoton Absorption Cross Sections of Arginine-Modified Gold Nanoclusters for Bioimaging. *ACS Appl. Mater. Interfaces* **2022**, *14* (2), 2452−2463.
(7) Bhawalkar, J. D.; He, G. S.; Prasad, P. N. Nonlinear multiphoton processes in organic and polymeric materials. *Rep. Prog. Phys.* **1996**, *59* (9), 1041.
(8) He, G. S.; Tan, L.-S.; Zheng, Q.; Prasad, P. N. Multiphoton Absorbing Materials: Molecular Designs, Characterizations, and Applications. *Chem. Rev.* **2008**, *108* (4), 1245−1330.
(9) Medishetty, R.; Zaręba, J. K.; Mayer, D.; Samoć, M.; Fischer, R. A. Nonlinear optical properties, upconversion and lasing in metal−organic frameworks. *Chem. Soc. Rev.* **2017**, *46* (16), 4976−5004.
(10) Pawlicki, M.; Collins, H. A.; Denning, R. G.; Anderson, H. L. Two-Photon Absorption and the Design of Two-Photon Dyes. *Angew. Chem., Int. Ed.* **2009**, *48* (18), 3244−3266.
(11) Weishäupl, S. J.; Mayer, D. C.; Cui, Y.; Kumar, P.; Oberhofer, H.; Fischer, R. A.; Hauer, J.; Pöthig, A. Recent advances of multiphoton absorption in metal−organic frameworks. *J. Mater. Chem. C* **2022**, *10* (18), 6912−6934.
(12) Ohta, K.; Antonov, L.; Yamada, S.; Kamada, K. Theoretical study of the two-photon absorption properties of several asymmetrically substituted stilbenoid molecules. *J. Chem. Phys.* **2007**, *127* (8), No. 084504.
(13) Walters, G.; Sutherland, B. R.; Hoogland, S.; Shi, D.; Comin, R.; Sellan, D. P.; Bakr, O. M.; Sargent, E. H. Two-Photon Absorption in Organometallic Bromide Perovskites. *ACS Nano* **2015**, *9* (9), 9340−9346.
(14) Nalwa, H. S. Organic Materials for Third-Order Nonlinear Optics. *Adv. Mater.* **1993**, *5* (5), 341−358.
(15) Terenziani, F.; Katan, C.; Badaeva, E.; Tretiak, S.; Blanchard-Desce, M. Enhanced Two-Photon Absorption of Organic Chromophores: Theoretical and Experimental Assessments. *Adv. Mater.* **2008**, *20* (24), 4641−4678.
(16) Quah, H. S.; Chen, W.; Schreyer, M. K.; Yang, H.; Wong, M. W.; Ji, W.; Vittal, J. J. Multiphoton harvesting metal−organic frameworks. *Nat. Commun.* **2015**, *6* (1), 7954.
(17) Kirchon, A.; Feng, L.; Drake, H. F.; Joseph, E. A.; Zhou, H.-C. From fundamentals to applications: a toolbox for robust and multifunctional MOF materials. *Chem. Soc. Rev.* **2018**, *47* (23), 8611−8638.
(18) Stanley, P. M.; Su, A. Y.; Ramm, V.; Fink, P.; Kimna, C.; Lieleg, O.; Elsner, M.; Lercher, J. A.; Rieger, B.; Warnan, J.; Fischer, R. A. Photocatalytic CO2-to-Syngas Evolution with Molecular Catalyst Metal-Organic Framework Nanozymes. *Adv. Mater.* **2023**, *35* (6), No. 2207380.
(19) Connolly, B. M.; Aragones-Anglada, M.; Gandara-Loe, J.; Danaf, N. A.; Lamb, D. C.; Mehta, J. P.; Vulpe, D.; Wuttke, S.; Silvestre-Albero, J.; Moghadam, P. Z.; Wheatley, A. E. H.; Fairen-Jimenez, D. Tuning porosity in macroscopic monolithic metal-organic frameworks for exceptional natural gas storage. *Nat. Commun.* **2019**, *10* (1), 2345.
(20) Medishetty, R.; Nemec, L.; Nalla, V.; Henke, S.; Samoć, M.; Reuter, K.; Fischer, R. A. Multi-Photon Absorption in Metal−Organic Frameworks. *Angew. Chem., Int. Ed.* **2017**, *56* (46), 14743−14748.
(21) Mingabudinova, L. R.; Vinogradov, V. V.; Milichko, V. A.; Hey-Hawkins, E.; Vinogradov, A. V. Metal−organic frameworks as competitive materials for non-linear optics. *Chem. Soc. Rev.* **2016**, *45* (19), 5408−5431.
(22) D'Aléo, A.; Felouat, A.; Heresanu, V.; Ranguis, A.; Chaudanson, D.; Karapetyan, A.; Giorgi, M.; Fages, F. Two-photon excited fluorescence of BF2 complexes of curcumin analogues: toward NIR-to-NIR fluorescent organic nanoparticles. *J. Mater. Chem. C* **2014**, *2* (26), 5208−5215.
(23) Johann, T.; Schmidt, K.; Prabhakaran, P.; Zentel, R.; Lee, K.-S. Two-photon absorption dye based on 2,5-bis(phenylacrylonitrile)-thiophene with aggregration enhanced fluorescence. *Opt. Mater. Express* **2016**, *6* (4), 1296−1305.
(24) Mei, J.; Leung, N. L. C.; Kwok, R. T. K.; Lam, J. W. Y.; Tang, B. Z. Aggregation-Induced Emission: Together We Shine, United We Soar! *Chem. Rev.* **2015**, *115* (21), 11718−11940.
(25) Mayer, D. C.; Manzi, A.; Medishetty, R.; Winkler, B.; Schneider, C.; Kieslich, G.; Pöthig, A.; Feldmann, J.; Fischer, R. A. Controlling Multiphoton Absorption Efficiency by Chromophore Packing in Metal−Organic Frameworks. *J. Am. Chem. Soc.* **2019**, *141* (29), 11594−11602.
(26) Weishäupl, S. J.; Cui, Y.; Deger, S. N.; Syed, H.; Ovsianikov, A.; Hauer, J.; Pöthig, A.; Fischer, R. A. Coordination Polymers Based on Carbazole-Derived Chromophore Linkers for Optimized Multiphoton Absorption: A Structural and Photophysical Study. *Chem. Mater.* **2022**, *34* (16), 7402−7411.
(27) ZareKarizi, F.; Joharian, M.; Morsali, A. Pillar-layered MOFs: functionality, interpenetration, flexibility and applications. *J. Mater. Chem. A* **2018**, *6* (40), 19288−19329.
(28) Quah, H. S.; Nalla, V.; Zheng, K.; Lee, C. A.; Liu, X.; Vittal, J. J. Tuning Two-Photon Absorption Cross Section in Metal Organic Frameworks. *Chem. Mater.* **2017**, *29* (17), 7424−7430.
(29) Mayer, D. C.; Zaręba, J. K.; Raudaschl-Sieber, G.; Pöthig, A.; Chołuj, M.; Zaleśny, R.; Samoć, M.; Fischer, R. A. Postsynthetic Framework Contraction Enhances the Two-Photon Absorption Properties of Pillar-Layered Metal−Organic Frameworks. *Chem. Mater.* **2020**, *32* (13), 5682−5690.
(30) Liu, N.; Chen, Z.; Fan, W.; Su, J.; Lin, T.; Xiao, S.; Meng, J.; He, J.; Vittal, J. J.; Jiang, J. Highly Efficient Multiphoton Absorption of Zinc-AIEgen Metal−Organic Frameworks. *Angew. Chem., Int. Ed.* **2022**, *61* (12), No. e202115205.
(31) Rath, B. B.; Kottilil, D.; Ji, W.; Vittal, J. J. Enhancement in Two-Photon Absorption and Photoluminescence in Single Crystals of Cd(II) Metal Organic Frameworks. *ACS Appl. Mater. Interfaces* **2023**, *15* (22), 26939−26945.
(32) Martinez, C. R.; Iverson, B. L. Rethinking the term "pi-stacking. *Chem. Sci.* **2012**, *3* (7), 2191−2201.
(33) Yao, Z.; Yang, L.; Cai, Y.; Yan, C.; Zhang, M.; Cai, N.; Dong, X.; Wang, P. Rigidifying the π-Linker to Enhance Light Absorption of Organic Dye-Sensitized Solar Cells and Influences on Charge Transfer Dynamics. *J. Phys. Chem. C* **2014**, *118* (6), 2977−2986.
(34) Huang, H.; Yang, L.; Facchetti, A.; Marks, T. J. Organic and Polymeric Semiconductors Enhanced by Noncovalent Conformational Locks. *Chem. Rev.* **2017**, *117* (15), 10291−10318.
(35) McCarthy, B. D.; Hontz, E. R.; Yost, S. R.; Van Voorhis, T.; Dincă, M. Charge Transfer or J-Coupling? Assignment of an Unexpected Red-Shifted Absorption Band in a Naphthalenediimide-

https://doi.org/10.1021/acsaom.4c00080
ACS Appl. Opt. Mater. XXXX, XXX, XXX−XXX

Based Metal−Organic Framework. *J. Phys. Chem. Lett.* **2013**, *4* (3), 453−458.
(36) Yang, L.; Yu, Y.; Feng, J.; Wu, J.; Jiang, L.; Dan, Y.; Qiu, Y. Charge transfer induced unexpected red-shift absorption of Zn and Cu porous coordination polymers based on electron-withdrawing ligand. *J. Photochem. Photobiol., A* **2018**, *350*, 103−110.
(37) Vaganova, T. A.; Gatilov, Y. V.; Benassi, E.; Chuikov, I. P.; Pishchur, D. P.; Malykhin, E. V. Impact of molecular packing rearrangement on solid-state fluorescence: polyhalogenated N-hetarylamines vs. their co-crystals with 18-crown-6. *CrystEngComm* **2019**, *21* (39), 5931−5946.
(38) Che, Y.; Perepichka, D. F. Quantifying Planarity in the Design of Organic Electronic Materials. *Angew. Chem., Int. Ed.* **2021**, *60* (3), 1364−1373.
(39) Bauer, C. A.; Timofeeva, T. V.; Settersten, T. B.; Patterson, B. D.; Liu, V. H.; Simmons, B. A.; Allendorf, M. D. Influence of Connectivity and Porosity on Ligand-Based Luminescence in Zinc Metal−Organic Frameworks. *J. Am. Chem. Soc.* **2007**, *129* (22), 7136−7144.
(40) Hashimoto, H.; Isobe, K.; Suda, A.; Kannari, F.; Kawano, H.; Mizuno, H.; Miyawaki, A.; Midorikawa, K. Measurement of two-photon excitation spectra of fluorescent proteins with nonlinear Fourier-transform spectroscopy. *Appl. Opt.* **2010**, *49* (17), 3323−3329.
(41) Makarov, N. S.; Drobizhev, M.; Rebane, A. Two-photon absorption standards in the 550−1600 nm excitation wavelength range. *Opt. Express* **2008**, *16* (6), 4029−4047.
(42) Segal, J.; Kotler, Z.; Sigalov, M.; Ben-Asuly, A.; Khodorkovsky, V. *Two-Photon Absorption Properties of (N-carbazolyl)-Stilbenes*; SPIE, 1999.
(43) Steiger, W.; Gruber, P.; Theiner, D.; Dobos, A.; Lunzer, M.; Van Hoorick, J.; Van Vlierberghe, S.; Liska, R.; Ovsianikov, A. Fully automated z-scan setup based on a tunable fs-oscillator. *Opt. Mater. Express* **2019**, *9* (9), 3567−3581.
(44) Ajami, A.; Husinsky, W.; Ovsianikov, A.; Liska, R. Dispersive white light continuum single Z-scan for rapid determination of degenerate two-photon absorption spectra. *Appl. Phys. B: Laser Opt.* **2018**, *124* (7), 142.
(45) Rumi, M.; Perry, J. W. Two-photon absorption: an overview of measurements and principles. *Adv. Opt. Photon.* **2010**, *2* (4), 451−518.
(46) Nag, A.; De, A. K.; Goswami, D. Two-photon cross-section measurements using an optical chopper: z-scan and two-photon fluorescence schemes. *J. Phys. B* **2009**, *42* (6), No. 065103.
(47) Lee, S.; Thomas, K. R. J.; Thayumanavan, S.; Bardeen, C. J. Dependence of the Two-Photon Absorption Cross Section on the Conjugation of the Phenylacetylene Linker in Dipolar Donor−Bridge−Acceptor Chromophores. *J. Phys. Chem. A* **2005**, *109* (43), 9767−9774.
(48) Rajput, S. S.; Zaleśny, R.; Alam, M. M. Chromophore Planarity, − BH Bridge Effect, and Two-Photon Activity: Bi- and Ter-Phenyl Derivatives as a Case Study. *J. Phys. Chem. A* **2023**, *127* (38), 7928−7936.
(49) Collins, J. Two-Photon Absorption and Applications to Biological Systems. In *Biophotonics: Spectroscopy, Imaging, Sensing, and Manipulation*; Springer: Dordrecht, The Netherlands, 2011; Bartolo, B. D., Collins, J., Eds.; pp 261−285.
(50) Wielgus, M.; Michalska, J.; Samoc, M.; Bartkowiak, W. Two-photon solvatochromism III: Experimental study of the solvent effects on two-photon absorption spectrum of p-nitroaniline. *Dyes Pigm.* **2015**, *113*, 426−434.
(51) Watanabe, S.; Tahara, A.; Isozaki, T.; Kinoshita, S.; Takeuchi, R.; Kashihara, W.; Suzuki, T. Effects of Two Electron-Donating and/or -Withdrawing Substituents on Two-Photon Absorption for Diphenylacetylene Derivatives. *J. Phys. Chem. A* **2023**, *127* (30), 6204−6212.
(52) Sorbara, S.; Mukherjee, S.; Schneemann, A.; Fischer, R. A.; Macchi, P. Hydrophobicity and dielectric properties across an isostructural family of MOFs: a duet or a duel? *ChemComm* **2022**, *58* (92), 12823−12826.
(53) Weishäupl, S. J.; Mayer, D. C.; Thyrhaug, E.; Hauer, J.; Pöthig, A.; Fischer, R. A. A nitrophenyl-carbazole based push-pull linker as a building block for non-linear optical active coordination polymers: A structural and photophysical study. *Dyes Pigm.* **2021**, *186*, No. 109012.

https://doi.org/10.1021/acsaom.4c00080
ACS Appl. Opt. Mater. XXXX, XXX, XXX−XXX

B.1. Supporting information

SI of Deger, S.N.[†]; Cui, Y.[†]; Warnan, J.; Fischer, R.A.; Šanda, F.; Hauer, J.; Pöthig, A. Influence of chromophore packing on multiphoton absorption in carbazole-based pillar-layered coordination polymers. *ACS Applied Optical Materials*, **2024**. The SI is available free of charge; thus, no reprint permission is necessary.

Supporting Information

for

Influence of Chromophore Packing on Multiphoton Absorption in Carbazole-Based Pillar-Layered Coordination Polymers

Simon N. Deger[a†], Yang Cui[b,c†], Julien Warnan,[a] Roland A. Fischer,[a] František Šanda[d], Jürgen Hauer[b], Alexander Pöthig[a*].*

[a]Technical University of Munich; TUM School of Natural Sciences, Department of Chemistry, Chair of Inorganic and Metal-Organic Chemistry; Catalysis Research Center, 85747 Garching, Germany

[b]Technical University of Munich; TUM School of Natural Sciences, Department of Chemistry, Professorship for Dynamic Spectroscopy; Catalysis Research Center, 85747 Garching, Germany

[c]Technical University of Munich; TUM School of Natural Sciences, Department of Physics; Catalysis Research Center, 85747 Garching, Germany

[d]Institute of Physics, Faculty of Mathematics and Physics, Charles University, Ke Karlovu 5, Prague 121 16, Czech Republic

† these authors contributed equally to this work

*Correspondence: alexander.poethig@tum.de (AP), juergen.hauer@tum.de (JH)

1. Synthesis of Carbazole Precursors[1]

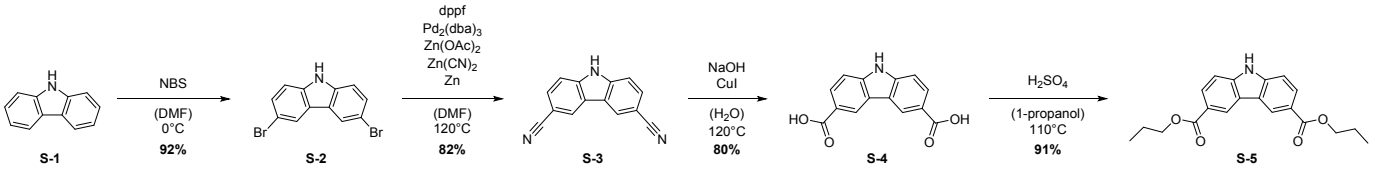

Figure S1. Synthesis route of the carbazole linker precursor

3,6-Dibromocarbazole (**S-2**): A solution of *N*-bromosuccinimide (22.4 g, 125 mmol) in 50 mL DMF was slowly added through a syringe pump to a stirring solution of carbazole (**S-1**, 10.0 g, 59.8 mmol) in 20 mL DMF in an ice bath. After 24 hours of reaction time, the mixture was poured into 600 mL ice water and then filtered through a suction filter to give a dark grey powder. The crude product was recrystallized with ethanol to give a grey powder of 3,6-dibromocarbazole (17.9 g, 92%).

^{1}H-NMR (400 MHz, 298 K, DMSO-d_6) δ (ppm) = 7.47 (d, J = 8.6 Hz, 2H), 7.53 (dd, J = 2.0, 8.6 Hz, 2H), 8.43 (d, J = 1.9, 2H), 11.59 (s, 1H, N-H).

Carbazole-3,6-dicarbonitrile (**S-3**): **S-2** (9.75 g, 30.0 mmol) and 1,1'-bis(diphenylphosphino)ferrocene]dichloropalladium (100 mg, 0.18 mmol) were added to a 100 mL Schlenk flask and solved in 30 mL DMF and 0.3 mL water. The suspension was degassed *via* bubbling argon for 1 hour through the mixture. Subsequently, $Zn(CN)_2$ (4.21 g, 36 mmol), zinc powder (78.0 mg, 1.2 mmol), $Zn(OAc)_2 \cdot 2\ H_2O$ (0.26 g, 1.2 mmol) and $Pd_2(dba)_3 \cdot$ dba (69.5 mg, 0.06 mmol) were added under a positive pressure of argon. This mixture was heated to 110 ˚C for 2 days. The suspension was cooled, poured into a 100 mL mixture of $H_2O/NH_4Cl/NH_3$ (5/4/1), and filtered through a suction filter. The filter cake was washed with the same volume of the above mixture, toluene (3 × 30 mL) and MeOH (3 × 30 mL) to give a grey solid. The crude product was recrystallized with DMF to give a white solid (5.26 g, 82%).

^{1}H-NMR (400 MHz, 298 K, DMSO-d_6) δ (ppm) = 7.72 (d, J = 8.5 Hz, 2H), 7.85 (d, J = 9.9 Hz, 2H), 8.80 (s, 2H), 12.38 (s, 1H, N-H).

Carbazole-3,6-dicarboxylic acid (**S-4**): **S-3** (4.20 g, 19.3 mmol) was suspended in an aqueous NaOH solution (12.5 g in 150 mL). To this solution CuI (37.5 mg, 0.20 mmol) was added and then quickly heated to 125 ˚C for 2 days, until the starting material was dissolved. Afterward, active carbon was added, and the mixture was again heated to 125 ˚C for 2 hours. After cooling, the suspension was filtered through celite, after the celite was pre-washed with aq. 2 N NaOH-solution. The filtrate was acidified with 6 M HCl-solution to give a white precipitate. The precipitate was filtered, washed with water, and dried to give a white solid (3.76 g, 80%).

^{1}H-NMR (400 MHz, 298 K, $CDCl_3$) δ (ppm) = 7.60 (d, J = 8.5 Hz, 2H), 8.06 (d, J = 8.4 Hz, 2H), 8.85 (s, 2H), 12.04 (s, 1H, N-H), 12.69 (bs, 2H, COOH).

Dipropyl-carbazole-3,6-dicarboxylate (**S-5**): **S-4** (4.01 g, 15.6 mmol) was suspended in 100 mL 1-propanol. To this suspension, conc. sulfuric acid (2 mL) was added and then refluxed at 110 ˚C for 24 hours. After cooling, the suspension was concentrated on a rotary evaporator and extracted with 200 mL dichloromethane. The organic layer was washed with aq. saturated $NaHCO_3$ (150 mL) and then dried with MgSO4. The solvent was evaporated to give a yellowish solid (4.88 g, 91%).

^{1}H NMR (400 MHz, 298 K, $CDCl_3$) δ (ppm) = 1.09 (t, J = 7.4 Hz, 6H), 1.87 (h, J = 7.2 Hz, 4H), 4.36 (t, J = 6.7 Hz, 4H), 7.47 (d, J = 8.5 Hz, 2H), 8.18 (dd, J = 1.5 Hz, 2H), 8.86 (s, 2H).

2. Synthesis of Linker H_4sbcd[2]

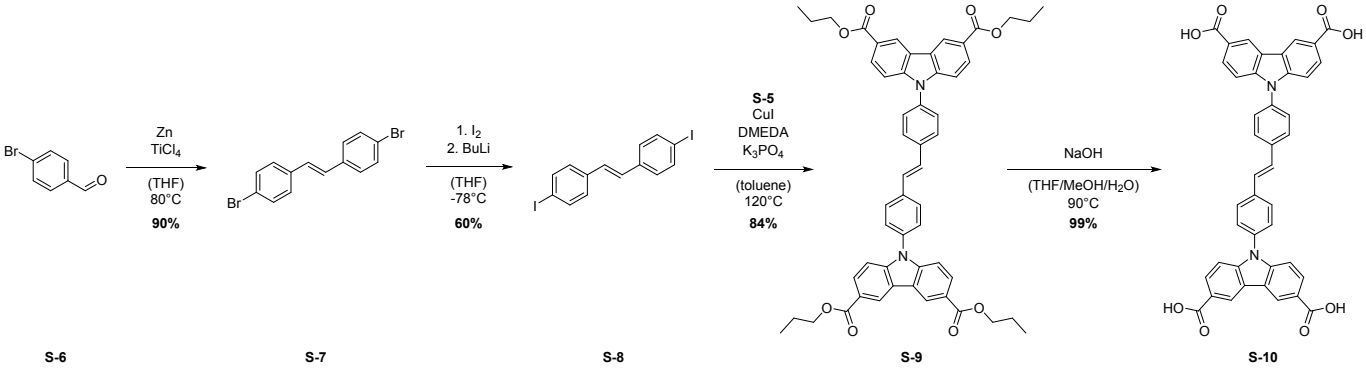

Figure S2. Synthesis route towards the linker molecule H_4sbcd **S-10**.

4,4'-Dibromostilbene (**S-7**): To a suspension of zinc powder (6.00 g, 90.7 mmol, 5.60 equiv) in THF (150 mL) at 0 °C, slowly, $TiCl_4$ (5 mL, 8.61 g, 45.3 mmol, 2.80 equiv) is added via a syringe. Subsequently, the reaction mixture is heated to 80 °C, and bromobenzaldehyde (3.00 g, 16.2 mmol, 1.00 equiv) and THF (50 mL) is added and heated for 5 h at reflux. After completion, saturated $NaHCO_3$ solution is added dropwise at room temperature. Afterward, the organic layer is separated and the water is extracted with chloroform (3 × 100 mL). The combined organic layers are dried with magnesium sulfate, filtered, and then concentrated on a rotary evaporator to yield a white solid (2.48 g, 90%).

^{1}H NMR (400 MHz, 298 K, DCl_3): δ (ppm) 7.02 (s, 2H), 7.36 (d, J = 8.47 Hz, 4H), 7.48 (d, J = 8.45 Hz, 4H).

4,4'-Diiodostilbene (**S-8**): 2.5 M *n*-BuLi solution in hexane (5.45 mL, 13.6 mmol, 4.60 equiv) was slowly dropped into a mixture of **S-7** (1.00 g, 2.96 mmol, 1.00 equiv) in THF (150 mL) at −78 °C. Then the yellow solution was stirred at −78 °C for 4 h. Afterward, it was warmed up to 0 °C, whereby the color of the solution changed from yellow to grayish yellow. The reaction mixture was cooled down again to −78 °C, and a solution of iodine (2.82 g, 11.1 mmol, 3.75 equiv) in THF (48 mL) was added. Finally, the reddish-brown solution was quenched with a solution of sodium thiosulfate (2 spatulas $Na_2S_2O_3$ in 150 mL H_2O) and filtrated through a glass filter. The filter cake was then washed multiple times with water and dried at 100 °C to afford a yellowish solid (769 mg, 60%).

^{1}H NMR (400 MHz, $CDCl_3$): δ (ppm) 7.04 (d, 4H), 7.26 (d, J = 14.2 Hz), 7.70 (dd, J = 8.3, 1.9 Hz, 4H).

Dipropyl-9,9'-(stilbyl)-bis-(carbazole-3,6-dicarboxylate) (**S-9**): **S-5** (0.79 g, 2.32 mmol, 2.00 equiv.), **S-8** (0.50 g, 1.16 mmol, 1.00 equiv), K_3PO_4 (1.97 g, 9.26 mmol, 8.00 equiv.), 1,2-dimethylethylenediamine (0.186 mL, 1.74 mmol, 1.5 equiv.), and CuI (66 mg, 0.34 mmol, 0.30 equiv.) were dissolved in 15 mL of dry toluene in a 50 mL Schlenk flask and heated to 115 °C for 3 days. After cooling, the suspension was dissolved in 60 mL of aq. saturated NH_4Cl solution,

extracted with chloroform (3 × 50 mL). The organic layers were combined and then dried with $MgSO_4$ and subsequently filtered. The solvent was evaporated on a rotary evaporator to give a brown solid. The crude product was then dissolved in 5 mL of dichloromethane (DCM) and added dropwise to 35 mL of MeCN in a centrifuge tube. The precipitate was collected by centrifugation and washed with MeCN twice to give a pale-yellow powder. Subsequently, the product is then subjected to column chromatography (DCM 100%) to give an off-white powder (830 mg, 0.96 mmol, 84%).

^{1}H NMR (400 MHz, $CDCl_3$): δ (ppm) 1.12 (t, J = 7.4 Hz, 12H), 1.89 (h, J = 7.2 Hz, 8H), 4.38 (t, J = 6.7 Hz, 8H), 7.26 (d, 4H), 7.49 (d, J = 8.5 Hz, 4H), 7.69 (d, J = 14.2 Hz, 2H), 7.86 (dd, J = 8.3, 1.9 Hz, 4H), 8.23 (dd, J = 1.5 Hz, 4H), 8.89 (s, 4H).

9,9'-(Stilbyl)-bis-(carbazole-3,6-dicarboxylic acid) (**S-10**) (H_4sbcd): To a solution of **S-9** (450 mg, 0.59 mmol, 1.00 equiv) in 150 mL of THF and 15 mL of MeOH, an aqueous NaOH solution (2.5 g in 250 mL of water) is added and heated for 18 h at 90 ˚C. After completion of the reaction, THF and MeOH are removed under vacuum on a rotary evaporator. Subsequently, the aqueous phase is acidified with a 2 N HCl solution till pH = 2 The resulting white precipitate is filtered, washed with water, and then dried, giving a white powder (390 mg, 0.56 mmol, 99%).

^{1}H NMR (400 MHz, 298 K, DMSO-d_6) δ (ppm) 7.52 (d, 4H), 7.61 (s, 2H) 7.74 (d, 4H), 8.02 (d, 4H), 8.12 (dd, 4H), 8.99 (s, 4H), 12.81 (s, 4H).

3. NMR-spectrum of H_4sbcd

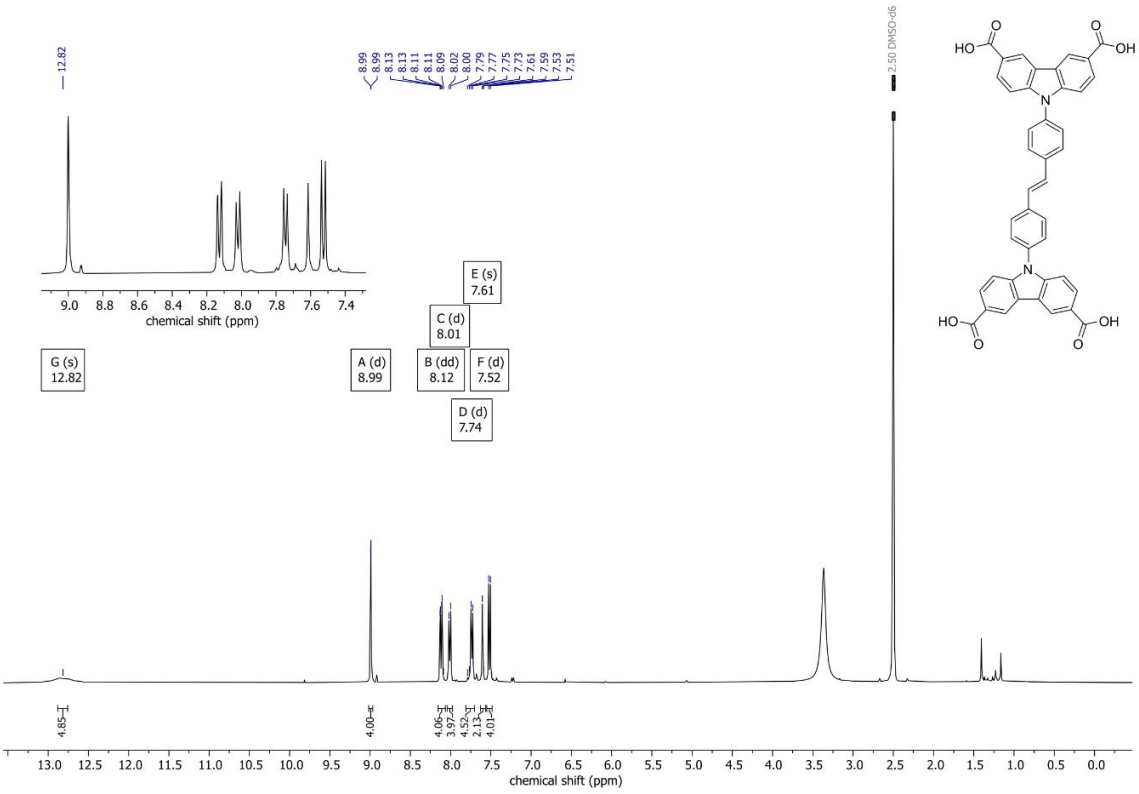

Figure S3. ^{1}H-NMR of the synthesized linker molecule H_4sbcd.

4. Powder X-Ray Diffraction (PXRD)

a) b)

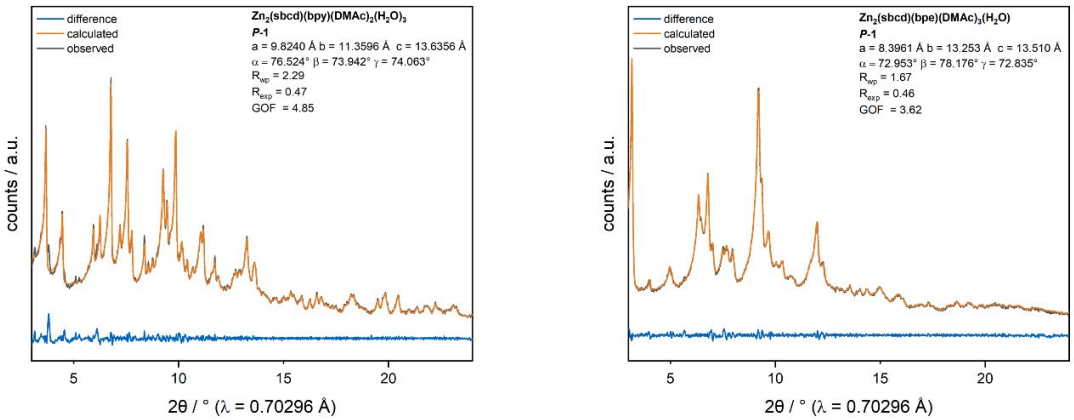

Figure S4. Pawley refinement of a) $Zn_{2n}(sbcd)(bpy)(DMAc)_{2n}(H_2O)_{3n}$ **(CP2)** and b) $Zn_{2n}(sbcd)(bpe)(DMAc)_{3n}(H_2O)$ (**CP3**). Both obtained sets of crystal parameters are in good accordance with the single crystal X-ray data.

5. IR Analysis (FT-IR) of the CPs and H_4sbcd

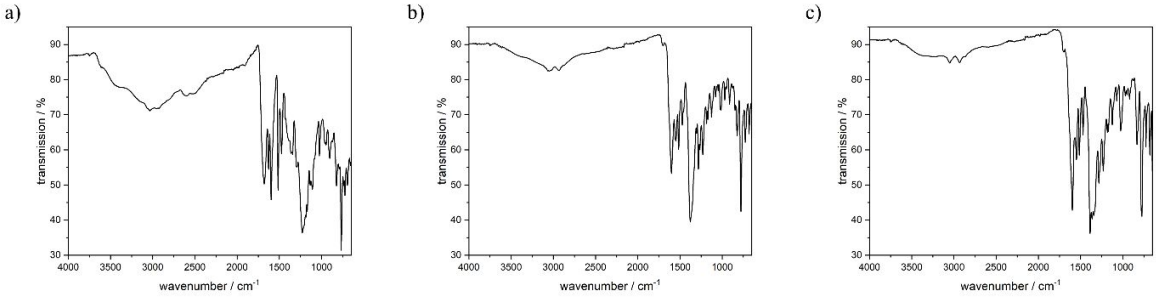

Figure S5. Infrared spectroscopy of a) H_4sbcd, b) $Zn_{2n}(sbcd)(bpy)(DMAc)_{2n}(H_2O)_{3n}$, and c) $Zn_{2n}(sbcd)(bpe)(DMAc)_{3n}(H_2O)$, showing the absence of the carboxyl C-O stretching mode at 1730 cm^{-1} for both CPs, verifying the successful incorporation in the network.

6. Thermo Gravimetric Analysis (TGA) of the CPs

a) b)

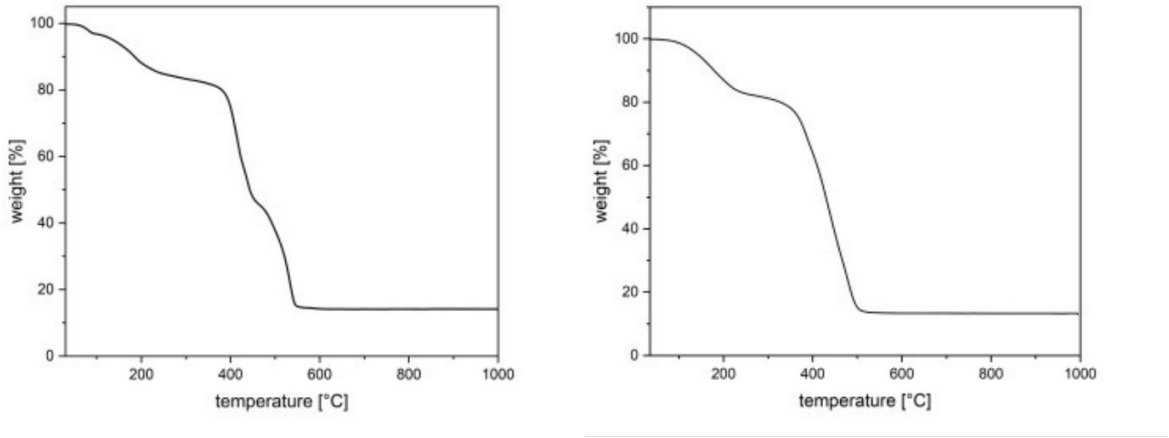

Figure S6. TGA of both coordination polymers: a) $Zn_{2n}(sbcd)(bpy)(DMAc)_{2n}(H_2O)_{3n}$, which is stable until 400 ˚C and shows a 4.6% weight loss until 105 ˚C equating to three molecules of H_2O, as well as a 14.5% weight loss until 370 ˚C equating to two molecules of DMAc. b) $Zn_{2n}(sbcd)(bpe)(DMAc)_{3n}(H_2O)$ showing a 20% weight loss starting at 100 ˚C until 300 ˚C, which equates to the loss of one H_2O and three DMAc molecules with the following decomposition at 380 ˚C.

7. Single Crystal Reports of the CPs

General Information

X-ray intensity data of the compound was collected at 100 K using a Bruker D8 Venture diffractometer equipped with a Helios optic monochromator, a Photon II CPAD detector and a Mo IMS microsource (Mo-Kα radiation). The raw area detector data frames were reduced

and corrected for absorption effects using the SAINT and SADABS programs with multi-scan absorption correction. Final unit cell parameters were determined by fast Fourier transform refinement of the respective independent reflections taken from the data sets. The structure was solved by autostructure with SHELXT. Difference Fourier calculations and full-matrix least-squares refinements against F2 were performed by SHELXL-2014/7 (Sheldrick, 2014). All non-hydrogen atoms were refined with anisotropic displacement parameters. Hydrogen atoms were refined by a mixture of independent and constrained refinement.

Report $Zn_{2n}(sbcd)(bpy)(DMAc)_{2n}(H_2O)_{3n}$

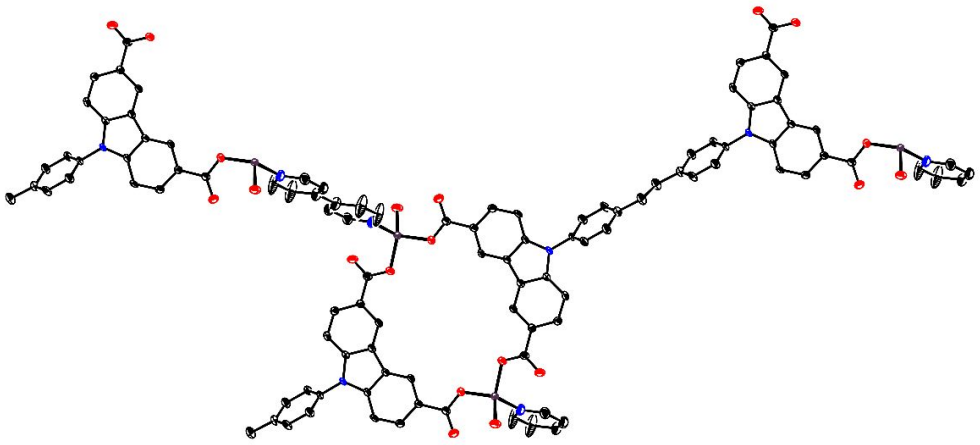

Figure S7. ORTEP representation of the single-crystal structure of $Zn_2(sbcd)(bpy)(DMAc)_2(H_2O)_3$ with thermal ellipsoids shown at the 50% probability level.

Table S1. Crystallographic data of $Zn_{2n}(sbcd)(bpy)(DMAc)_{2n}(H_2O)_{3n}$.

Crystal data	DegSi15
Chemical formula	$C_{26}H_{17}N_2O_5Zn$
M_r	502.81
Crystal system, space group	Triclinic, *P*-1
Temperature (K)	100
a, b, c (Å)	9.8240(7), 11.3596(8), 13.6356(11)
α, β, γ (°)	76.524(3), 73.942(3), 74.063(3)
V (Å^3)	1385.64(18)
Z	2
Radiation type	Mo Kα
μ (mm^{-1})	0.920
Crystal size (mm)	0.038 × 0.082 × 0.113
Data collection	
Diffractometer	Bruker Photon CMOS
Absorption correction	Multi-scan SADABS 2016/2, Bruker, 2016
T_{min}, T_{max}	0.6779, 0.7454
No. of measured, independent and observed [I > 2σ(I)] reflections	32451, 4480, 4115
R_{int}	0.0491
Refinement	
$R[F^2 > 2\sigma(F^2)]$, wR(F2), S	0.044, 0.127, 1.12
No. of reflections	4480

No. of parameters	315
No. of restraints	45
H-atom treatment	H atoms treated by a mixture of independent and constrained refinement $W = 1/[\Sigma^2(FO^2) + (0.172P)^2 + 35.4396P]$ WHERE $P = (FO^2 + 2FC2)/3$
Δρmax, Δρmin (e $Å^{-3}$)	1.114, -0.414

Report $Zn_{2n}(sbcd)(bpe)(DMAc)_{3n}(H_2O)$

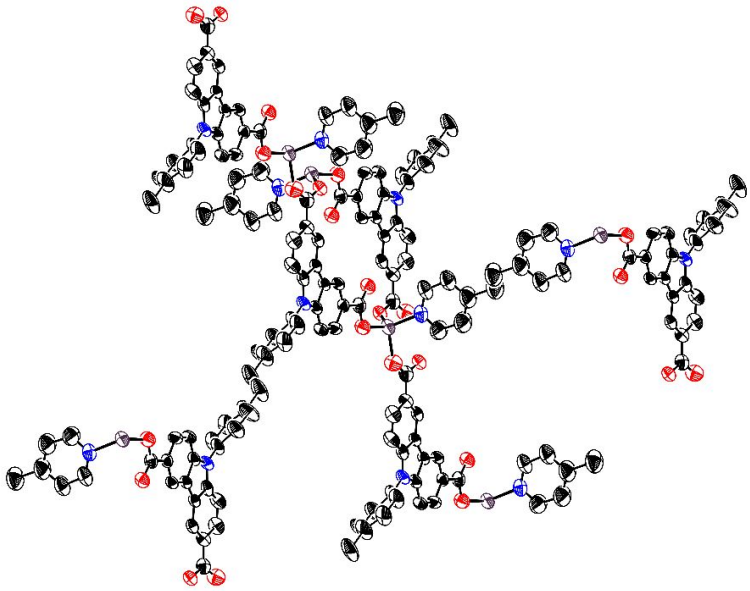

Figure S8. ORTEP representation of the single-crystal structure of $Zn_{2n}(sbcd)(bpe)(DMAc)_{3n}(H_2O)$ with thermal ellipsoids shown at the 50% probability level.

Table S2. Crystallographic data of $Zn_2(sbcd)(bpe)(DMAc)_3(H_2O)$.

Crystal data	DegSi16
Chemical formula	$C_{27}H_{17.47}N_2O_4Zn$
M_r	499.29
Crystal system, space group	Triclinic, *P*-1
Temperature (K)	101
a, b, c (Å)	8.3961(16), 13.253(3), 13.510(3)
α, β, γ (°)	72.953(7), 78.176(7), 72.835(7)
V (Å^3)	1361.7(5)

Z	2
Radiation type	Mo Kα
μ (mm^{-1})	0.933
Crystal size (mm)	0.063 × 0.109 × 0.193
Data collection	
Diffractometer	Bruker Photon CMOS
Absorption correction	Multi-scan SADABS 2016/2, Bruker, 2016
T_{min}, T_{max}	0.5981, 0.7454
No. of measured, independent and observed [I > 2σ(I)] reflections	30474, 4768, 3327
R_{int}	0.0874
Refinement	
$R[F^2 > 2\sigma(F^2)]$, wR(F2), S	0.0732, 0.2289, 1.03
No. of reflections	4768
No. of parameters	371
No. of restraints	269
H-atom treatment	H atoms treated by a mixture of independent and constrained refinement W = $1/[\Sigma^2(FO^2) + (0.172P)^2 + 35.4396P]$ WHERE $P = (FO^2 + 2FC2)/3$
Δρmax, Δρmin (e $Å^{-3}$)	0.551, -0.520

8. Two-photon excitation spectroscopy

8.1 Experimental setup

The working principle and experimental design for Fourier transform two-photon fluorescence excitation spectroscopy is similar as described by Hashimoto *et al.*[3, 4] A schematic of our setup is shown in Figure S9. The broadband spectra in our lab are generated from a noncollinear optical parametric amplifier (NOPA rainbow) pumped by femtosecond pulses from a mode-locked Yb:KGW laser (Light Conversion, PHAROS PH2) operating at 1024 nm with a variable repetition rate of up to 200 kHz.[5, 6]

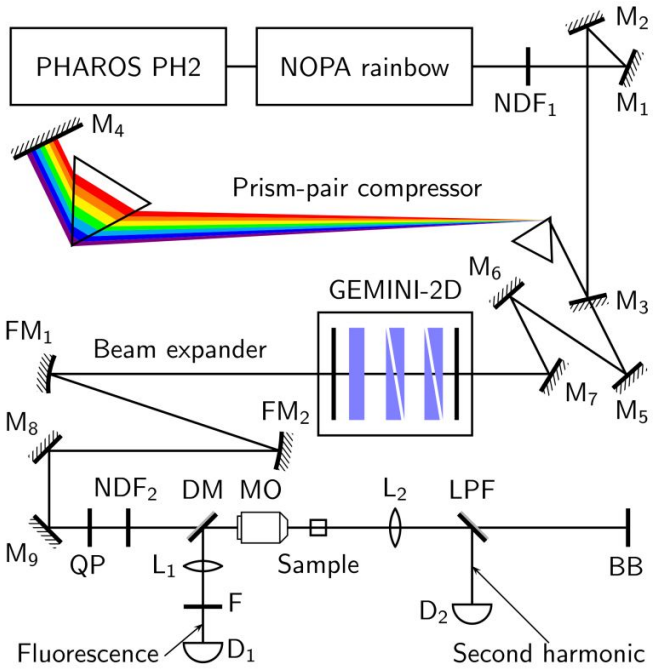

Figure S9: Experimental design for interferometric two-photon excitation spectroscopy. NDF: neutral density filter; M: mirror; FM: focusing mirror; QP: quartz plate; DM: dichroic mirror; MO: microscope objective; L: lens; F: filter; D: detector; LPF: long-pass filter; BB: beam block (see text for details).

The NOPA output spectra used for this work are shown in Figure S10. The dispersion introduced by the interferometer, microscope objective, and other transmissive optics

is pre-compensated using a prism pair fused silica compressor. Pulse pairs are generated using a phase-stable common-path birefringent interferometer (NIREOS, GEMINI-2D, please see Preda *et al.* for design details).[7] They are focused on the sample position using a long working distance (7.4 mm) microscope objective (Nikon, CFI S Plan Fluor ELWD 20XC, NA 0.45). Pulse duration is measured by cFROG (collinear frequency-resolved optical gating)[8] using a 10-µm thick type-I phase matching BBO crystal as a nonlinear medium. Spectrum NOPA850 gives a pulse duration of 10 fs (Fourier limit is 7 fs), while NOPA750 gives a pulse duration of 15 fs (Fourier limit is 17 fs). For details of the data processing procedure, please see Section 8.3.

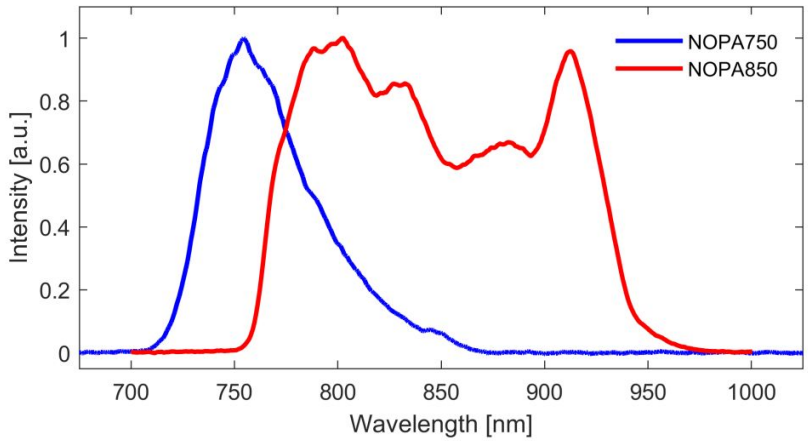

Figure S10: NOPA spectra used for two-photon excitation in this work.

8.2 Sample preparation of CPs

CP crystalline powders are ground to uniform powders. Each CP powder was weighted and mixed with 500 mg PMMA (1.18 g/mol) powder into 5 mL DCM and stirred for 2 hours in the solution. Afterward, PMMA film samples were prepared using the 'doctor blade' method with subsequent evaporation of the DCM.

Table S3: Parameters used to calculate the concentration of CPs in film state.

CPs	Molecular weight [g/mol]	Mass [mg]	Concentration [mmol/L]
CP1	1014.41	16.7	38.9
CP2	1197.88	5	9.9
CP3	1277.03	5	9.2

8.3 Data treatment

To get two-photon excitation spectra of the samples under investigation, we follow the procedure described in the work of Hashimoto and co-workers.[3, 4] Here we take **CP2** as an example to illustrate the data processing routine; all other samples measured at different spectral ranges will follow the same procedure. Once the pulse duration was optimized, we recorded the interferogram of the second harmonic (SH) signal in the forward direction using a fiber spectrometer (D_2 in Figure S9). The *x*-axis is in the unit of wedge positions in the GEMINI-2D interferometer (Figure S11). Afterward, the BBO crystal was replaced with **CP2** sample, and the two-photon induced fluorescence was collected in the backward direction using a dichroic mirror. The interferogram of the fluorescence signal for **CP2** is depicted in Figure S12.

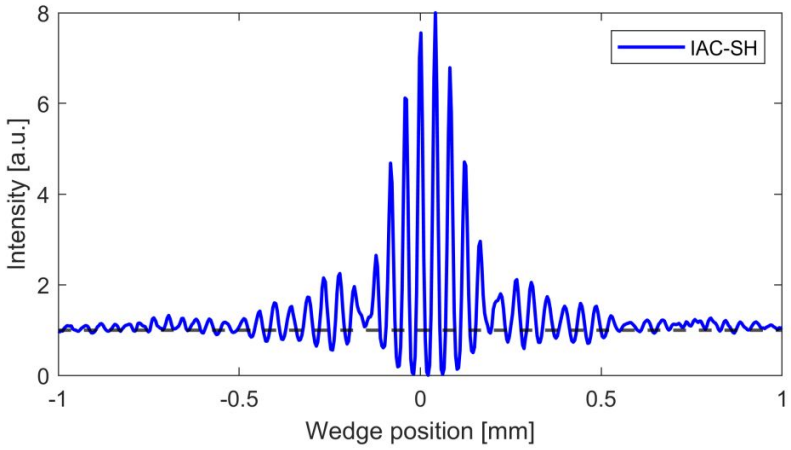

Figure S11: Interferometric autocorrelation (IAC) trace of the second harmonic (SH) signal from a BBO crystal.

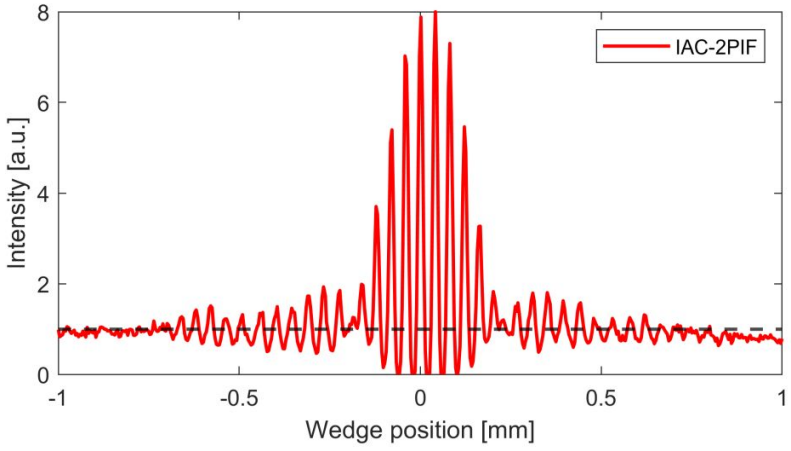

Figure S12: Interferogram of two-photon induced fluorescence (2PIF) signal from **CP2**.

Fourier transform (FT) of interferograms gives the second harmonic spectrum corresponding to the current NOPA spectrum and the two-photon excitation spectrum of **CP2**, respectively. After axis calibration, i.e., from the wedge position to the detection wavelength, both spectra are plotted together in Figure S13. The normalized two-photon excitation spectrum can be obtained by dividing the second harmonic spectrum (FT[SH-IAC]) from the two-photon excitation spectrum (FT[2PIF-IAC]), as shown in Figure S14. In the end, the two-photon absorption cross-section values were calculated by comparing the two-photon induced fluorescence with a standard sample. Fluorescein dyes dissolved in water with pH11 (36GM@800nm) were used to calibrate cross-section values for the H_4sbcd linker, while **CP1** (3359GM@840nm) was used to calibrate the cross-section values of **CP2** and **CP3**.[2, 9]

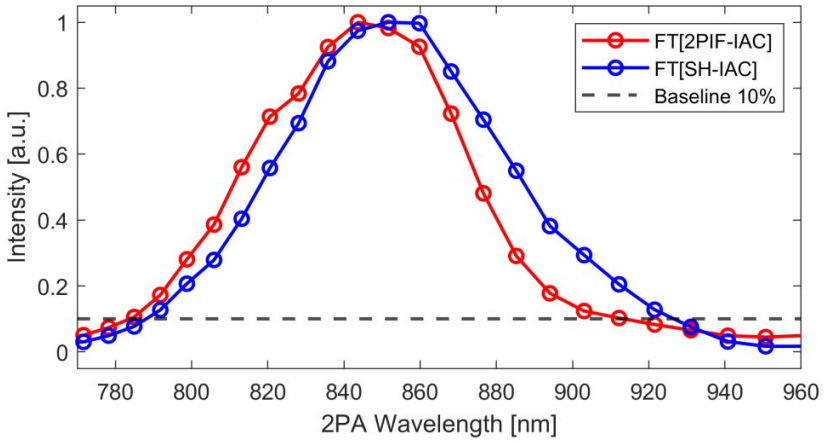

Figure S13: Fourier transform of interferograms in Figures S11 and S12 gives the two-photon excitation spectrum of **CP2** (FT[2PIF-IAC], red) and second harmonic spectrum of a BBO crystal (FT[SH-IAC], blue), respectively.

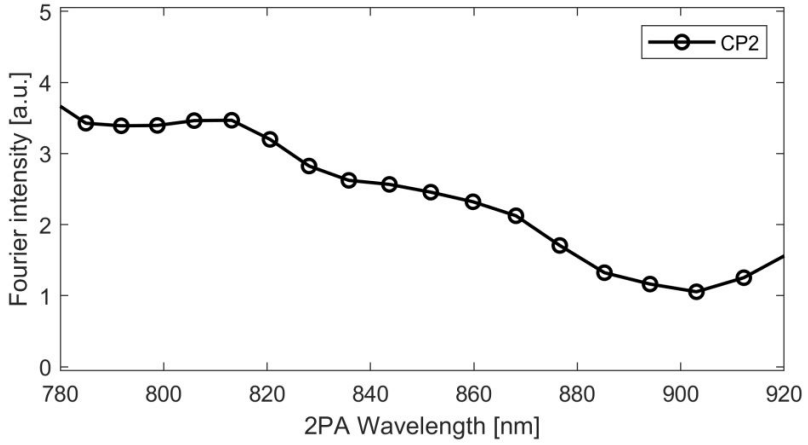

Figure S14: Normalized two-photon excitation spectrum of **CP2**.

The two-photon induced fluorescence of the H_4sbcd linker was compared with the fluorescein under the excitation of 800 nm, as shown in Figure S15. Two-photon-induced fluorescence excited at 840 nm for **CP1**, **CP2**, and **CP3** were measured 10 times for each and are depicted in Figures S16, S17, and S18, respectively. The mean values were used to compare the fluorescence strengths. Note: all four spectra were collected using the same integration time, i.e., 500 ms but with different excitation intensities. The unknown two-photon absorption cross-sections can be determined using the following relation.[9]

$$\sigma_{2,\ sam}(\lambda) = \frac{F_{2,sam} C_{ref} \phi_{ref}}{F_{2,ref} C_{sam} \phi_{sam}} \sigma_{2,ref}(\lambda)$$

where $\sigma_2(\lambda)$ is two-photon absorption cross sections at a given wavelength λ, $F_2(\lambda)$ is the fluorescence intensity per unit laser power per unit time at the registration wavelength, C is the concentration, ϕ is the quantum yield. Indices *sam* and *ref* stand for the sample and the reference samples.

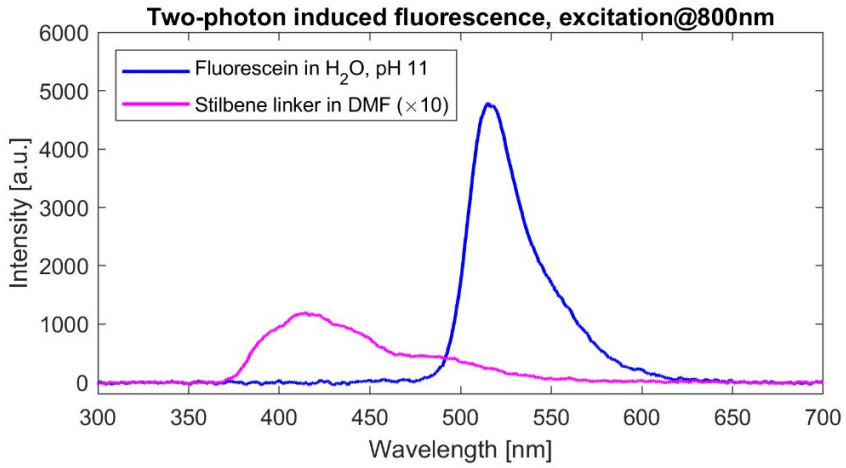

Figure S15: Two-photon induced fluorescence spectra of fluorescein with concentration of 100 μM and stilbene linker (H_4sbcd) in DMF with a concentration of 500 μM.

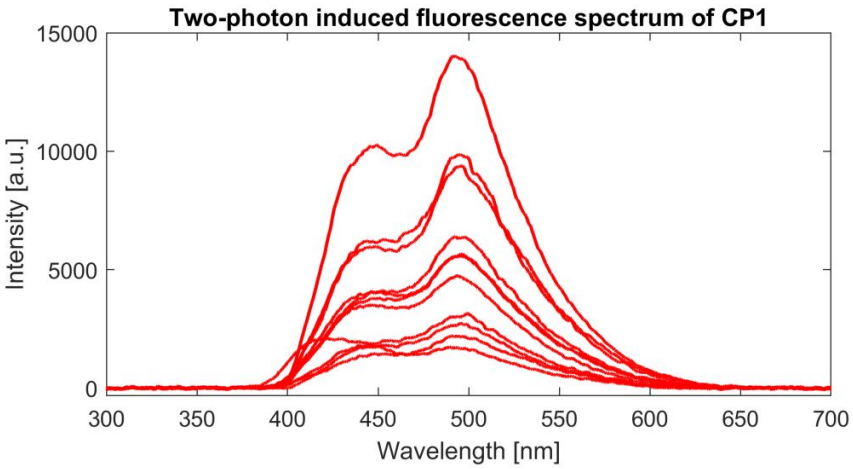

Figure S16: Two-photon induced fluorescence spectra of **CP1**.

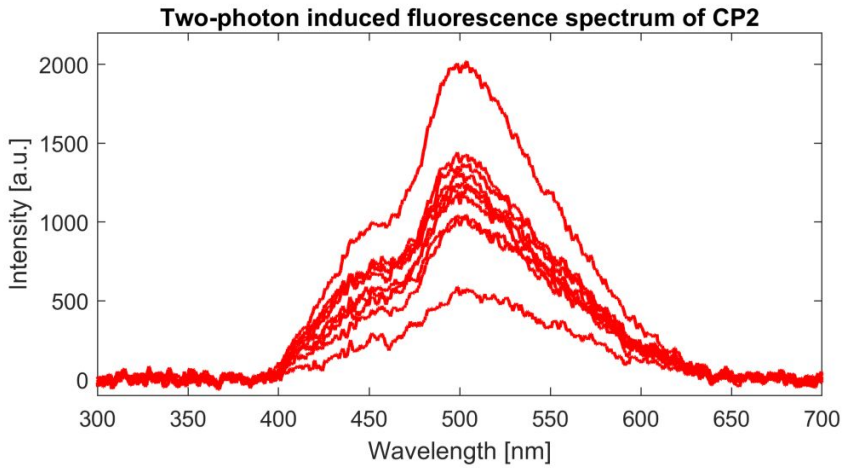

Figure S17: Two-photon induced fluorescence spectra of **CP2**.

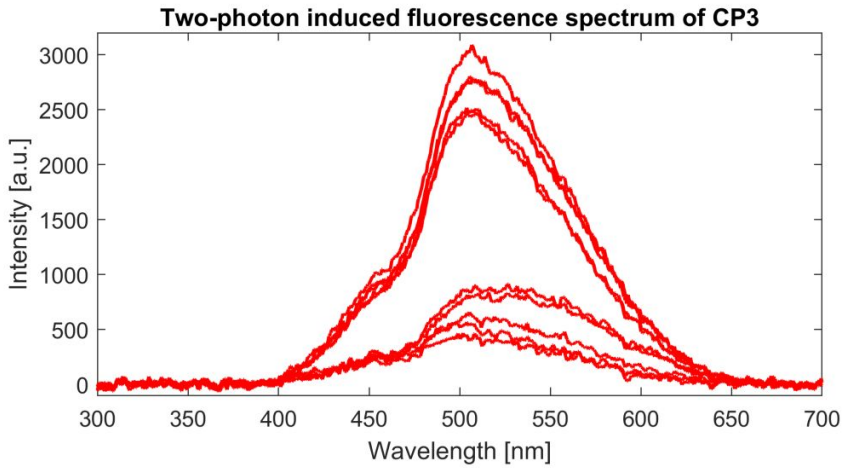

Figure S18: Two-photon induced fluorescence spectra of **CP3**.

9. References

(1) Weishäupl, S. J.; Mayer, D. C.; Thyrhaug, E.; Hauer, J.; Pöthig, A.; Fischer, R. A. A nitrophenyl-carbazole based push-pull linker as a building block for non-linear optical active coordination polymers: A structural and photophysical study. *Dyes Pigm.* **2021**, *186*, 109012.

(2) Weishäupl, S. J.; Cui, Y.; Deger, S. N.; Syed, H.; Ovsianikov, A.; Hauer, J.; Pöthig, A.; Fischer, R. A. Coordination Polymers Based on Carbazole-Derived Chromophore Linkers for Optimized Multiphoton Absorption: A Structural and Photophysical Study. *Chem. Mater.* **2022**, *34* (16), 7402-7411.

(3) Isobe, K.; Suda, A.; Tanaka, M.; Kannari, F.; Kawano, H.; Mizuno, H.; Miyawaki, A.; Midorikawa, K. Fourier-transform spectroscopy combined with a 5-fs broadband pulse for multispectral nonlinear microscopy. *Phys. Rev. A* **2008**, *77* (6), 063832.

(4) Hashimoto, H.; Isobe, K.; Suda, A.; Kannari, F.; Kawano, H.; Mizuno, H.; Miyawaki, A.; Midorikawa, K. Measurement of two-photon excitation spectra of fluorescent proteins with nonlinear Fourier-transform spectroscopy. *Appl. Opt.* **2010**, *49* (17), 3323-3329.

(5) Bradler, M.; Riedle, E. Sub-20 fs μJ-energy pulses tunable down to the near-UV from a 1 MHz Yb-fiber laser system. *Opt. Lett.* **2014**, *39* (9), 2588-2591.

(6) Schriever, C.; Lochbrunner, S.; Krok, P.; Riedle, E. Tunable pulses from below 300 to 970 nm with durations down to 14 fs based on a 2 MHz ytterbium-doped fiber system. *Opt. Lett.* **2008**, *33* (2), 192-194.
(7) Preda, F.; Oriana, A.; Réhault, J.; Lombardi, L.; Ferrari, A. C.; Cerullo, G.; Polli, D. Linear and Nonlinear Spectroscopy by a Common-Path Birefringent Interferometer. *IEEE J. Sel. Top.Quantum Electron.* **2017**, *23* (3), 88-96.
(8) Amat-Roldán, I.; Cormack, I. G.; Loza-Alvarez, P.; Gualda, E. J.; Artigas, D. Ultrashort pulse characterisation with SHG collinear-FROG. *Opt. Express* **2004**, *12* (6), 1169-1178.
(9) Makarov, N. S.; Drobizhev, M.; Rebane, A. Two-photon absorption standards in the 550–1600 nm excitation wavelength range. *Opt. Express* **2008**, *16* (6), 4029-4047.